POLITECNICO DI MILANO

School of Industrial and Information Engineering

Master's degree in Materials Engineering and Nanotechnology

Development of Paper-Based SERS Sensors for the Detection of Drugs

Supervisor: Prof. Matteo Tommasini
Co-Supervisor: Prof. Andrea Lucotti

<div align="right">

Master's thesis of:
Andrea MACRELLI
ID: 917845

</div>

Academic year 2019-2020

"I am among those who think that science has great beauty. A scientist in his laboratory is not only a technician: he is also a child placed before natural phenomena which impress him like a fairy tale."

Marie Skłodowska-Curie
Madame Curie: A Biography

"Cieco chi guarda il cielo senza comprenderlo: è un viaggiatore che attraversa il mondo senza vederlo; è un sordo in mezzo ad un concerto."

Camille Flammarion
Les étoiles et les curiosités du ciel

Ringraziamenti

Nella stesura della tesi, la parte dei ringraziamenti è sicuramente una tra le più difficili, se non la più difficile. Sono stati cinque anni intensi, ricchi, stimolanti ed impegnativi, in un contesto, quello del Politecnico di Milano, che mi ha fatto conoscere tante cose e incontrare molte persone. La situazione attuale, in un mondo in preda alla pandemia, ha un po' offuscato gli ultimi mesi del mio percorso universitario, ma desidero ringraziare chi, nonostante tutto, mi ha aiutato e supportato, non solo durante il lavoro di tesi ma in tutti e cinque gli anni.

Innanzitutto, ringrazio il professor Matteo Tommasini, senza il quale questa tesi non sarebbe mai nata. Grazie per i consigli, gli insegnamenti e la tranquillità con cui mi ha seguito durante le ore in laboratorio e nella stesura della tesi, anche nei momenti di maggiore difficoltà.
Ringrazio Andrea Lucotti e Luigi Brambilla, per l'aiuto pratico e per la pazienza con cui mi hanno insegnato a maneggiare i complicati strumenti in laboratorio, trasmettendomi una piccola parte della loro enorme esperienza.
Ringrazio Ettore Maggiore e David Dellasega, del Dipartimento di Energia, per avermi guidato negli angoli remoti della materia attraverso il microscopio ottico ed elettronico.
Ringrazio Nicolò Villa, per i suggerimenti e le dritte di chi "ci è già passato" e, soprattutto, per aver trovato il *Perampanel* in un momento in cui il morale era basso.
Ringrazio Cinzia Citti, dell'Istituto di Nanotecnologia del CNR, per aver fornito i campioni necessari di CBD.
Ringrazio i professori Marco Beghi, Chiara Bertarelli, Carlo Casari, Mirella Del Zoppo, Andrea Li Bassi e Valeria Russo che, in questi cinque anni, mi hanno fatto appassionare al mondo "infinitamente piccolo" degli atomi e delle nanotecnologie.

Ringrazio mia mamma, per aver sopportato le mie ansie e per essermi stata vicina sempre. Grazie per tutto, anche per aver costantemente dimostrato che la vera mente matematica è la tua. Un grazie anche a mio papà, alle mie sorelle Laura e Silvia, a mia nonna e ai miei zii Paola e Marco (detto Tob) per avermi appoggiato, ognuno a modo suo, nei momenti felici e in quelli meno felici.

Ringrazio Loredana, Diego e Claudia, per il provvidenziale aiuto quando il computer aveva deciso di rompersi ad un mese dalla consegna.

Ringrazio Cristina Gambalonga e Jessica Corbyn, per il supporto con la lingua inglese.

Ringrazio la dottoressa Barbara Caloni, per avermi accompagnato in tutti questi anni, aiutandomi a superare alcune delle mie paure e a trovare il mio posto nel mondo.

Per ultimi ma non meno importanti, ringrazio gli amici del Poli, Alberto, Arianna, Cecilia, Chiara, Christopher, Davide, Erik, Giorgio, Laura, Matteo e Simone, per aver condiviso con me le lunghe giornate in università, le lezioni, gli esami, la stanchezza, ma anche i momenti goliardici e spensierati tra le grandi aule del Poli.

Grazie a tutti!

Abstract

My Master's thesis was aimed at developing and testing paper-based SERS sensors for the detection and quantification of selected examples of anti-epileptic drugs, namely Perampanel (PER) and Cannabidiol (CBD). Properly prepared filter-paper supports were loaded with silver or gold nanoparticles by means of simple, rapid and inexpensive techniques, such as dip-coating with colloidal dispersions and *in situ* reduction of a metallic precursor, and the dipping procedure was further accelerated by the use of a centrifuge. Both the colloids and the final substrates were characterized by UV-VIS-NIR spectroscopy and the nanostructured morphology was investigated with scanning electron microscopy (SEM).

Silver substrates produced by dip-coating (via both natural sedimentation and centrifugation) were tested using acidified PER solutions in a concentration range between 10^{-4} M and 10^{-6} M and SERS measurements were carried out using the 632.8 nm excitation and adopting the spinning-cell setup to overcome the problem of spatial non-uniformity. At the same time, the relevant problem of the strong contribution originating from the background was addressed and chloride-containing solutions proved to be effective in significantly reducing the background. The same substrates were employed for quantitative SERS measurements of PER; despite quite large error bars, arising primarily from the poor inter-sample repeatability, a linear correlation between the average peak height and the PER concentration was observed.

Moving to the second analyte, silver substrates produced via centrifugation were tested with a 10^{-4} M solution of CBD, although the final spectra, even upon the addition of the complexing and enhancing agent $MgCl_2$, were quite unsatisfactory. Finally, the last chapter is devoted to substrates prepared by *in situ* reduction of silver onto paper supports. PER was clearly detected on substrates produced with trisodium citrate (TSC) as reducing agent, whereas the silver content in the absence of TSC was low, resulting in poor SERS properties.

The final results highlighted the potential of rapidly and easily prepared paper-made sensors for the SERS detection of specific analytes, paving the way for future development and optimization.

Contents

List of Figures

List of Tables

Introduction

Surface-Enhanced Raman Spectroscopy (SERS) is a technique that effectively combines the spectroscopic fingerprint provided by Raman spectroscopy with a huge signal intensification when molecules are in the proximity of properly designed metal nanostructures [1, 2]. In recent times, SERS is emerging as a widely available analytical technique and it is promisingly applied to the detection, identification and quantification of analytes in many fields, including analytical chemistry, biochemistry, cultural heritage, forensic sciences and trace analysis of drugs, medicines, explosives, food additives and contaminants [1, 3]. More recently, SERS has been proposed as a complementary technique for therapeutic drug monitoring (TDM) of drugs characterized by a narrow therapeutic index, such as anti-cancer and anti-epileptic drugs (AEDs), for which the determination of the exact blood concentration is essential to individualize the therapy and to minimize adverse effects [4, 5]. Indeed, narrow therapeutic index (NTI) is defined as the restricted concentration range in which, for a given patient, a drug is effective without adverse or toxic effects [5]. Good results have been achieved so far, but the routine application of SERS in clinical practice is still unfeasible [4]. Previous works have focused on the potential of SERS in TDM of selected anti-epileptic drugs, like Carbamazepine (CBZ) [5, 6], Lamotrigine (LTG) [7], and Perampanel (PER) [5, 8–10], dissolved in simple solutions at concentrations within or outside the therapeutic range. Considering the particular case of PER, gold and silver nanoparticles produced by chemical methods and deposited onto glass supports and nanostructured films produced by pulsed laser ablation (PLA) or pulsed laser ablation in liquid (PLAL) have been employed as SERS substrates in the last few years [6, 8–12]. Important issues concerning the sensitivity, the detection limit, the spatial uniformity, and the repeatability have been systematically addressed.

The current pandemic and the need to use readily available materials and substances have influenced the development of my thesis work, encouraging me to rely on alternative types of SERS substrates which could be produced with fast, easy, and cheap methods. In particular, I exploited the so-called *plasmonic paper* [13], i.e. a paper-

based material loaded with metal nanoparticles for plasmonic applications. The first use of paper-based substrates of SERS relevance dates back to 1984 [14] but the field has evolved significantly since then, exploring novel substrate designs and applications. Many paper-based materials have been considered, including filter paper [14, 15], sand paper [16], office paper [13], news paper, kraft paper and nanocomposite cellulosic materials [14]. Cellulose is the most abundant biopolymer on earth and combines biocompatibility and biodegradability with low cost, proving to be both a cheap and easy-to-use solid platform for SERS and a green reducing and stabilizing agent in the synthesis of metal nanoparticles [14, 16]. Unlike traditional rigid supports like glass, silicon wafers and aluminium, paper has unique features such as flexibility, porosity, thinness, ease of functionalization, wicking capability, large surface area, and 3D fibrous structure that make it an ideal platform to host nanoparticles and to produce SERS sensors suitable for point-of-care medical diagnostics, water quality assessment and food safety [13–16]. The sensitivity of the substrate depends on several factors, but detection limits as low as 10^{-16} M of Rhodamine 6G have been reported [17]. Moreover, many methods have been employed to load the paper with nanoparticles, such as drop casting, dip coating, *in situ* coating (including silver mirror reaction [17]), inkjet printing, screen printing, spray coating, brushing, pen-on-paper and physical vapour deposition [14], each providing the final substrate with specific plasmonic properties.

In my thesis, I selected two rapid, simple, and inexpensive bottom-up approaches, i.e. dip-coating of filter-paper with concentrated silver and gold colloids and *in situ* reduction of silver with and without the use of an external reducing agent. To further accelerate the production process, I used a centrifuge to speed up the aggregation of the metal nanoparticles on the paper fibres. In this way, starting from the same colloidal dispersion, I succeeded in producing some tens of comparable SERS substrates in just a few hours. Since my thesis belongs to a wider research subject on the TDM of AEDs using SERS, I applied my substrates to the qualitative and quantitative detection of the well-known *Perampanel* (PER) and to the potential detection of the cannabinoid *Cannabidiol* (CBD), investigated in a parallel Master's thesis. The use of paper-based SERS sensors for TDM has already been reported in the literature, e.g. for the anti-neoplastic Methotrexate (MTX) in human serum [18] and for the anticonvulsant Phenobarbital (PB) in tear fluids [19], both in their therapeutic ranges.

The measured average total and free (non-protein bound) concentrations of PER are, respectively, 343.02 and 1.53 ng/mL (about 9.8×10^{-7} and 4.4×10^{-9} M) in plasma, and 9.74 and 2.83 ng/mL (about 2.8×10^{-8} and 8.1×10^{-9} M) in saliva [20]. Such low concentrations were not practical for my tests on newly developed SERS substrates, therefore

I restricted myself to a concentration range of 10^{-4} - 10^{-6} M. Similar considerations hold for CBD; plasma level in 100 patients evaluated in reference [21] ranged from 7.1 to 1200 ng/mL (corresponding to 2.26×10^{-8} - 2.82×10^{-6} M), but I considered a 10^{-4} M CBD solution in my thesis.

As a result, my thesis is primarily aimed at demonstrating the feasibility of simple production methods to fabricate many comparable SERS substrates, with a quantitative response in a concentration range not too far from the reference therapeutic range of PER in plasma. After a brief overview of the theoretical background on Raman spectroscopy and SERS, Perampanel and Cannabidiol will be presented in chapter 2 and their application as anti-epileptic drugs will be mentioned, along with a comprehensive molecular characterization on the basis of previous theses and other literature works. Chapter 3 will be devoted to the detailed description of the synthesis of colloidal silver, of the dip-coating production method, and of the characterization of the optical and morphological properties of the produced SERS substrates. The first SERS tests carried out using paper-based sensors with Rhodamine 6G and Perampanel will be presented in chapter 4, in which important issues regarding the optimization of the detection conditions, the reduction of the background, the excitation laser, and the spatial uniformity of the sensors will be addressed. In chapter 5, quantitative SERS measurements performed on optimized sensors will be discussed, leading to the construction of calibration curves, while the CBD detection attempts will be described in chapter 6. Finally, alternative substrates produced by *in situ* reduction of a silver precursor or using colloidal gold will be investigated in chapter 7, providing ideas about further optimization and improvement of sensitivity, reproducibility and production methods.

Chapter 1

Methods and Theory

The interaction between light and matter produces numerous signals that can be detected and interpreted to investigate the chemical-physical nature of a sample. This is the working principle of all the *optical spectroscopies*, which differ from each other in the underlying physical process and in the sample energy states involved during this process. As a result, different molecular properties can be probed using different spectroscopic techniques. For instance, the absorption of a photon in the visible or in the ultraviolet (200-800 nm) causes the excitation of an electron to higher states and can be used to probe the electronic structure of a molecular system (*UV-VIS spectroscopy*). Conversely, infrared photons (1-100 μm) do not have enough energy to cause electronic transitions but they can excite a molecule to higher vibrational levels within a given electronic state, probing its vibrational structure (*IR spectroscopy*). After absorption, the relaxation from an excited state to a low-energy state accompanied by the emission of a photon is responsible for *luminescence*, of which fluorescence and phosphorescence are the most common examples. Finally, a photon can interact with a molecule without being absorbed but undergoing *scattering*. The scattering process can be both elastic and inelastic depending on whether energy is exchanged or not with the molecule. Like fluorescence, two photons are involved in the scattering event but the overall process is instantaneous and does not require the physical absorption of the incident photon and the excitation of the molecule to a high electronic state [1].

1.1 Raman spectroscopy

Raman spectroscopy is an analytical technique that exploits the *Raman scattering* to gain chemical and structural information about a sample. The Raman effect was first discovered by the Indian physicist Chandrasekhara Venkata Raman in 1921, who was awarded the *Nobel Prize in Physics* in 1930 with the following rationale [22]:

> "*For his work on the scattering of light and for the discovery of the effect named after him*".

When monochromatic light interacts with a sample, both elastic and inelastic scattering processes may occur: most of the radiation is scattered at constant energy and frequency, but a small fraction of light with different energy can be observed and the difference with respect to the incident radiation depends on the specific exchange of energy with the vibrational modes of the sample. This difference in energy because of inelastic processes, typically reported in wavenumbers (i.e., cm^{-1}), is known as the *Raman shift* and is the key factor in Raman spectroscopy, since the exchanged energy strongly depends on the position of vibrational levels, which in turn is determined by the molecular structure of the system. As a result, a Raman spectrum is a unique fingerprint of a molecule.

Raman spectroscopy has a universal character and can be applied to solids (both crystalline and amorphous), liquids, solutions, and gases, producing important results in the fields of art and archaeology, biosciences, analytical chemistry, solid-state physics, nanotechnology, pharmaceutical studies, and forensic science [1]. In addition, it is non-invasive and non-destructive and any material can be in principle investigated.

1.1.1 Classical theory of Raman scattering

In this section, the Raman scattering will be explained using a simple classical treatment, in which both the sample and the electromagnetic radiation are described in a classical way [23]. In particular, the incident radiation is a monochromatic plane wave and is expressed in terms of an electric field vector $\boldsymbol{E}$ harmonically oscillating at the frequency ω_L:

$$\mathbf{E} = \mathbf{E}_0 \cos(\omega_L t) \tag{1.1}$$

The incoming light induces a polarization in the sample and the corresponding frequency-dependent induced electric dipole $\boldsymbol{p}$, in the linear approximation, is proportional to the incident electric field through the polarizability tensor $\boldsymbol{\alpha}$:

$$\mathbf{p} = \boldsymbol{\alpha} \cdot \mathbf{E} \tag{1.2}$$

The polarizability tensor is an intrinsic property of the molecule and depends on the nuclear coordinates of atoms. As a result, the polarizability changes if atoms move from their equilibrium positions because of molecular vibrations. Considering one single molecule which can vibrate freely, the dependence of the polarizability on all the normal coordinates of the molecule can be expressed as a Taylor series:

$$\boldsymbol{\alpha} = \boldsymbol{\alpha}_0 + \sum_k \left(\frac{\partial \boldsymbol{\alpha}}{\partial Q_k} \right)_0 Q_k + ... \tag{1.3}$$

where the index *0* stands for the equilibrium configuration and higher order terms are neglected in the linear approximation [23]. The summation in equation 1.3 includes all the normal modes of the molecule, i.e. $3N-6$, where N is the number of atoms in a non-linear molecule [1].

In the harmonic approximation, the variation of the kth normal coordinate in time is expressed by a simple cosine function oscillating at the characteristic frequency ω_k:

$$Q_k = Q_{k_0} \cos(\omega_k t + \delta_k) \tag{1.4}$$

Considering, for simplicity, one normal mode only and substituting equation 1.4 into equation 1.3, the polarizability tensor as a function of the kth vibration is obtained:

$$\boldsymbol{\alpha} = \boldsymbol{\alpha}_0 + \left(\frac{\partial \boldsymbol{\alpha}}{\partial Q_k}\right)_0 Q_{k_0} \cos(\omega_k t + \delta_k) \tag{1.5}$$

The final expression of the induced electric dipole is derived introducing equations 1.1 and 1.5 into 1.2:

$$\mathbf{p} = \boldsymbol{\alpha}_0 \mathbf{E}_0 \cos(\omega_L t) + \left(\frac{\partial \boldsymbol{\alpha}}{\partial Q_k}\right)_0 \mathbf{E}_0 Q_{k_0} \cos(\omega_k t + \delta_k) \cos(\omega_L t) \tag{1.6}$$

Equation 1.6 can be manipulated using Werner's trigonometric formulas and rewritten in a more compact form:

$$\mathbf{p} = \boldsymbol{\alpha}_0 \mathbf{E}_0 \cos(\omega_L t) + \frac{1}{2}\left(\frac{\partial \boldsymbol{\alpha}}{\partial Q_k}\right)_0 \mathbf{E}_0 Q_{k_0} \left[\cos((\omega_L - \omega_k)t - \delta_k) + \cos((\omega_L + \omega_k)t + \delta_k)\right] \tag{1.7}$$

The induced electric dipole moment in equation 1.7 contains cosine functions oscillating at three different frequencies, which are the result of three distinct scattering processes occurring during light-matter interaction:

* The first term, proportional to the equilibrium polarizability tensor and oscillating at the frequency of the incoming radiation ω_L, is the *Rayleigh* component and corresponds to elastic scattering, which is by far the most probable scattering event. No energy is exchanged with the molecule and the energy of the incident radiation is the same as the energy of the scattered one.

* The second term, proportional to the derived polarizability tensor, is the *Raman* component and arises because of inelastic processes. Some energy is exchanged with the sample and the frequency of the scattered radiation is modified by the frequency of the considered normal mode of vibration. In particular, when the incident radiation gives energy to the molecule, the outgoing radiation is red-shifted and oscillates at frequency $\omega_L - \omega_k$ (*Stokes* component); on the other hand, when the incident radiation acquires energy from the molecule, the outgoing radiation is blue-shifted and oscillates at frequency $\omega_L + \omega_k$ (*anti-Stokes* component).

Stokes and anti-Stokes processes are much less probable than elastic scattering, therefore the corresponding peaks in a Raman spectrum are not very intense (figure 1.1). In addition, the shift with respect to the Rayleigh peak (usually expressed in wavenumbers, $\tilde{\nu} = (2\pi c)^{-1}\omega$) is a function of the vibrational frequency only and is independent of the frequency of the excitation radiation ω_L [1, 23].
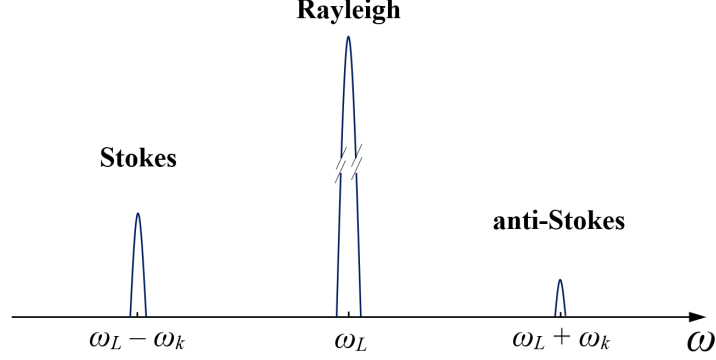
Figure 1.1: Schematic representation of the characteristic peaks of a Raman spectrum.

1.1.2 Calculation of intensity

The intensity of the scattered radiation can be calculated using the expression for the time-averaged power radiated per unit solid angle by an oscillating electric dipole induced in the molecule by an incident electric field; according to classical electromagnetism [23]:

$$I = \frac{\omega_s^4 \cdot p_0^2}{32\pi^2\varepsilon_0 c^3}\sin^2\theta \tag{1.8}$$

where ω_s is the dipole frequency, p_0 is the dipole amplitude and θ is the angle between the dipole axis and the emission direction. Combining equations 1.7 and 1.8, it can be demonstrated that the intensity of the scattered radiation is proportional to the fourth power of the frequency, to the square of the amplitude of the incident electric field E_0 (i.e. to the intensity of the incident radiation), and to the square of the derived polarizability tensor [23, 24]:

$$I \propto \omega_s^4 \cdot I_0(\omega_L) \cdot \left(\frac{\partial\boldsymbol{\alpha}}{\partial Q_k}\right)_0^2 \tag{1.9}$$

It should be noted that the intensity I depends on the derivative of the polarizability tensor with respect to the normal coordinate Q_k; the larger the variation of the polarizability of the molecule upon the vibration along the kth normal mode, the larger the intensity will be. Therefore, in order to have nonzero intensity, at least one component of the tensor must be different from zero, according to specific selection rules strongly affected by molecular symmetry [1, 23].

Moreover, the theoretical intensity ratio of Stokes to anti-Stokes bands can be evaluated:

$$\frac{I_{Stokes}}{I_{anti-Stokes}} = \frac{(\omega_L - \omega_k)^4}{(\omega_L + \omega_k)^4} \tag{1.10}$$

which is clearly smaller than 1 [24]. This result is in contrast with experimental data, because anti-Stokes lines are always less intense than Stokes lines. As a result, even if the classical theory correctly predicts the position of Raman lines, it fails to describe the exact intensity ratio and a more accurate quantum treatment is necessary.

1.1.3 Quantum theory of Raman scattering

The classical approach can be justified and improved by using quantum mechanics. Actually, only the molecule (or the crystal) is treated quantum mechanically, while the electromagnetic field still behaves classically according to Maxwell's equations. This kind of approach is called *semi-classical* [1].

Considering a molecular system with N atoms, the Schrödinger equation for nuclei in the presence of a harmonic potential can be solved:

$$\hat{\mathcal{H}}_\nu \Psi_\nu = E_\nu \Psi_\nu \tag{1.11}$$

where $\hat{\mathcal{H}}_\nu$ is the vibrational Hamiltonian for the quantum problem. The introduction of the normal coordinates Q_k allows the decoupling of the problem and the diagonalization of the Hamiltonian, which becomes simply written as the sum of $3N-6$ independent quantum harmonic oscillators, with no cross-terms. The corresponding eigenvalue is the sum of the energy contributions of each oscillator:

$$E_\nu = \sum_{k=1}^{3N-6} E_k = \sum_{k=1}^{3N-6} \hbar\omega_k \left(\nu_k + \frac{1}{2} \right) \quad \text{with} \quad \nu_k = 0, 1, 2, ... \tag{1.12}$$

Similarly, the total wavefunction is the product of the eigenfunctions of each normal mode. For a given electronic state and for a given normal mode of frequency ω_k, vibrations are quantized and only discrete vibrational energies, labelled by a quantum number ν_k, are allowed. In the harmonic approximation, vibrational levels are equally spaced, with a zero-point energy different from zero. Rayleigh and Raman scattering can be explained on the basis of quantized energy levels through the use of Jablonski diagrams [1]. Unlike fluorescence, scattering processes can occur without direct photon absorption, so without transitions between true molecular electronic states; when light interacts with a molecule in its ground state S_0 (ν=0), it is excited to an intermediate high-energy virtual state. If the molecule comes back to the initial level without any change in the vibrational state, the photon is scattered elastically (Rayleigh process).

On the other hand, if the molecule deexcites to the first excited vibrational state ($\nu=1$), the outcoming photon will be characterized by a lower energy (Stokes process, figure 1.2), because the energy difference $E_{\nu=1}-E_{\nu=0}$ is given to a quantum of vibration.
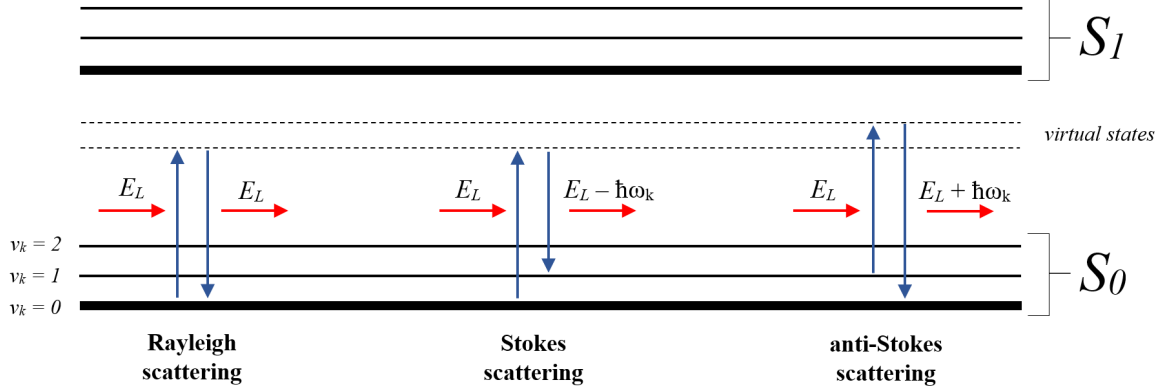
Figure 1.2: Simplified Jablonsky diagram representing Rayleigh, Stokes and anti-Stokes scattering processes.

When the molecule is already in a high-energy vibrational state (e.g., $\nu=1$) and is excited to the virtual state, it can relax to the vibrational ground state ($\nu=0$), resulting in a scattered photon with more energy than the incident one (anti-Stokes process, figure 1.2). The probability of anti-Stokes processes to occur is strongly temperature-dependent because the population of higher vibrational levels is determined by thermal equilibrium. Since the quanta of vibrations (i.e. the quasi-particles associated to the population of the levels in a harmonic oscillator) are bosons, the occupancy of vibrational levels is described by the *Bose-Einstein distribution function* [1]:

$$n_k(T) = \frac{1}{e^{\frac{\hbar\omega_k}{\kappa T}} - 1} \tag{1.13}$$

which depends on both the frequency and the temperature. The quantum approach allows the derivation of the correct ratio of Stokes to anti-Stokes intensities for a given normal mode of vibration. It can be demonstrated that the application of the time-dependent perturbation theory to the transition probabilities between two vibrational states under the action of an external electric field, also accounting for the statistical Bose-Einstein factor, leads to the following expression [23]:

$$\frac{I_{Stokes}}{I_{anti-Stokes}} = \frac{(\omega_L - \omega_k)^4}{(\omega_L + \omega_k)^4} \cdot e^{\frac{\hbar\omega_k}{\kappa T}} \tag{1.14}$$

The ratio in equation 1.14 is larger than 1 thanks to the presence of the exponential factor, in accord with experiments. Moreover, the ratio decreases with increasing temperature: the intensity of the anti-Stokes peak depends on the occupancy of the

initial state and the population of excited vibrational levels grows as the temperature increases.

1.1.4 Selection rules

The intensity of the inelastically scattered radiation is a function of the derived polarizability tensor (known as the *Raman tensor*), as stated in equation 1.9. Therefore, only those normal modes involving a variation of the molecular polarizability tensor during the vibration are Raman-active. The Raman tensor may be zero in molecules with high symmetry, in which the contributions of symmetric atoms cancel out. In particular, molecules containing an inversion centre are symmetric with respect to the operation $r \longrightarrow -r$ and satisfy the *mutual exclusion principle*: normal modes are either Raman or infrared active and the two spectroscopic techniques can be used in a complementary way to completely characterize a molecule (a normal mode is infrared-active when the electric dipole moment of the molecule varies during the vibration) [1]. In non-symmetric molecules, all vibrations are, in principle, both Raman and infrared active.

1.1.5 Resonance Raman scattering

In a Raman experimental setup, the sample is irradiated with a laser (typically in the visible or near-infrared range), which provides not only a large intensity but also monochromaticity [1]. In general, the laser frequency is selected to avoid any absorption by the molecule [24]: the sample is transparent to the incident light and the resulting spectrum is independent of the excitation wavelength. This is the case of non-resonance Raman, as described in 1.1.3.

Nevertheless, when the laser frequency falls within an absorption band, the intermediate virtual state coincides with a real electronic level, resulting in a strong intensification of some Raman lines by several orders of magnitude (10^3-10^6) [1, 25]. This process, known as *resonance Raman scattering* (RRS), exploits a stronger interaction between light and matter and is more selective, also providing information about the electronic structure of the molecule. RRS is competitive to absorption/fluorescence, but the physical mechanisms and the characteristic timescales are completely different, being scattering faster than absorption. The relative efficiency of scattering and absorption depends on the molecule, moreover, strong fluorescence can be excited in some chromophores, hindering the detection of the Raman signal. The overwhelming effect of fluorescence can be reduced using a long-wavelength exciting radiation [25].

1.2 Surface Enhanced Raman Scattering

High specificity, non-destructiveness, minimum sample preparation, multiplexing and flexibility are essential advantages of Raman spectroscopy [3]. However, two intrinsic limitations reduce the applicability of conventional Raman when high sensitivity is required, i.e. the signal weakness and the strong fluorescence emission. The first drawback is related to the inherently small probability of the Raman process to occur, whose cross-section is 12 to 14 orders of magnitude lower than the fluorescence one [2]. Indeed, only one in every 10^7 photons is inelastically scattered, while the large majority of photons undergo elastic scattering [25]. The second disadvantage is represented by strong fluorescence emission, especially when visible exciting radiation is used, which can prevent the detection of the Raman signal. Resonance Raman scattering (RRS) can be exploited to amplify the intensity of the Raman lines, even if a suitable laser source must be selected to match a real electronic transition and fluorescence may still be a problem [5].

Alternatively, a huge intensification of Raman signals coming from molecules can be achieved when the analyte is close to the surface of a metallic nanostructured substrate. This is the principle of *Surface-Enhanced Raman Scattering* (SERS), that has gradually become a valuable technique able to combine the spectroscopic fingerprint typical of Raman spectroscopy with a very large sensitivity as requested by trace detection in chemical, biological, medical, forensic, and food sciences. The first observation of the SERS effect dates back to 1974, when M. Fleischmann reported a strong Raman signal from pyridine adsorbed on electrochemical roughened silver electrodes. His observations were later confirmed by two independent works by D.L. Jeanmaire and R.P. Van Duyne and by M.G. Albrecht and J.A. Creighton, who also provided a first explanation about the origin of the enhancement: the amplification of the signal was not caused by an increase in the surface area, as supposed by Fleischmann, but because of strong electric fields at the metal surface (according to Jeanmarie and Van Duyne) or due to the formation of a molecule-metal complex (according to Albrecht and Creighton). An important review was published in 1985 by M. Moskovits, who related the intensification effect with the excitation of collective oscillations of conduction electrons in the metal nanostructure. In the following years, the technological improvement in Raman instrumentation, the advancement of nanotechnology and the possibility of single-molecule detection have fostered the development of SERS as a powerful tool for analytical investigations, although some theoretical aspects regarding the exact enhancement mechanism are not fully clarified [1, 3].

1.2.1 Optical properties of metals

Before addressing the SERS enhancement, the plasmonic properties of metals and metal nanoparticles should be briefly introduced. The optical behaviour of metals is largely determined by the electrons in the conduction band, which can be approximated as free electrons moving in a fixed array of positive ions (*plasma* or *Drude model*). The effect of the crystal lattice is not explicitly considered but it is included into an effective electron mass. The validity of this model extends over a range of frequencies that depends on the kind of metal, up to the threshold for interband transitions [26, 27].

The equation of motion for a free electron moving under the action of an external electric field with a harmonic time-dependence is reported in equation 1.15:

$$m\frac{\mathrm{d}^2\mathbf{x}}{\mathrm{d}t^2} + m\Gamma\frac{\mathrm{d}\mathbf{x}}{\mathrm{d}t} = -e\mathbf{E}_0 e^{-i\omega t} \tag{1.15}$$

where the second term accounts for collisions and contains a damping factor Γ, which is the inverse of the average collisional time (at room temperature, $\Gamma \approx 10^{14}$ Hz).
The electronic oscillations produce a macroscopic polarization in the material, which can be expressed by equation 1.16 considering a particular solution of equation 1.15 and the electron concentration N:

$$\mathbf{P} = -Ne\mathbf{x} = -\frac{Ne^2}{m\left(\omega^2 + i\Gamma\omega\right)}\mathbf{E}_0 e^{-i\omega t} \tag{1.16}$$

The complex amplitude incorporates any phase shift between the input and the material response. Recalling the expression of the dielectric displacement vector:

$$\mathbf{D} = \varepsilon_0\mathbf{E} + \mathbf{P} = \varepsilon_0\varepsilon(\omega)\mathbf{E} \tag{1.17}$$

the equation of the complex dielectric constant as a function of the angular frequency is derived:

$$\varepsilon(\omega) = 1 - \frac{Ne^2}{\varepsilon_0 m\left(\omega^2 + i\Gamma\omega\right)} = 1 - \frac{\omega_p^2}{\omega^2 + i\Gamma\omega} \tag{1.18}$$

where ω_p

$$\omega_p = \sqrt{\frac{Ne^2}{\varepsilon_0 m}} \tag{1.19}$$

is the plasma frequency of the system. Theoretical values of the plasma frequency are 8.9 eV (139 nm) for gold, 9.2 eV (135 nm) for silver and 8.7 eV (142 nm) for copper [3].

The dielectric function can be rewritten to highlight the real and the imaginary part:

$$\varepsilon(\omega) = \varepsilon'(\omega) + i\varepsilon''(\omega) = 1 - \frac{\omega_p^2}{\omega^2 + \Gamma^2} + i\frac{\omega_p^2\Gamma}{\omega\left(\omega^2 + \Gamma^2\right)} \tag{1.20}$$

Focusing on optical frequencies (UV-VIS, $\omega \approx 10^{15}$ Hz), the inequality $\omega \gg \Gamma$ holds and the dielectric function is approximated as in equation 1.21:

$$\varepsilon'(\omega) \approx 1 - \frac{\omega_p^2}{\omega^2} \quad \text{and} \quad \varepsilon''(\omega) \approx \frac{\omega_p \Gamma}{\omega^3} \tag{1.21}$$

from which it is possible to notice that $\varepsilon''(\omega)$ is negligible with respect to $\varepsilon'(\omega)$ and the dielectric function is predominantly real [26]:

$$\varepsilon(\omega) = 1 - \frac{\omega_p^2}{\omega^2} \tag{1.22}$$

Looking at equation 1.22, three regimes can be identified:

- When $\omega < \omega_p$, $\varepsilon(\omega) < 0$, the refractive index ($n = \sqrt{\varepsilon(\omega)}$) is purely imaginary, and the reflectance is equal to 1. The incident radiation is completely reflected back and cannot propagate in the material, where an evanescent wave decays exponentially in the first tens of nanometres below the surface (metallic domain).

- When $\omega > \omega_p$, $\varepsilon(\omega) > 0$, the refractive index is real and light is transmitted through the metal (transparency domain).

- When $\omega = \omega_p$, $\varepsilon(\omega) = 0$ and collective in-phase longitudinal oscillations of free conduction electrons are observed. The quanta of this oscillation are called bulk plasmons, each corresponding to an energy equal to $\hbar\omega_p$.

This model is an oversimplification and real metals exhibit large discrepancies. First of all, the imaginary part of the dielectric constant has been neglected; secondly, bound electrons, responsible for interband transition (especially in transition metals with inner d bands), have not been considered; and thirdly, the polarization background of ions has not been included in the model.

The concept of plasmon can be extended to an interface between a dielectric ($\varepsilon_d > 0$) and a metal. The solution of Maxwell's equations for a flat interface leads to the dispersion relation of *surface plasmon polaritons* (SPP), which are defined as non-radiative propagating modes, bound at the interface and evanescently confined in the perpendicular direction, with a transverse-magnetic/longitudinal-electric character [26, 27]. In order to be able to observe SPPs, a precise relationship between the dielectric constants of the two materials must be fulfilled:

$$\varepsilon(\omega) < 0 \quad \text{and} \quad \varepsilon(\omega) < -\varepsilon_d \tag{1.23}$$

For large wavevectors, the dispersion relation of SPP tends to the characteristic surface plasmon frequency:

$$\omega_{SP} = \frac{\omega_p}{\sqrt{1 + \varepsilon_d}} \tag{1.24}$$

1.2.2 Optical properties of metal nanoparticles

The oscillations of conduction electrons in a metal nanoparticle under illumination can be modelled as a mass-spring system; the harmonic external electric field is the driving force, while the curved surface of the particle and the electrostatic attraction between separate charges act as a restoring force (figure 1.3). The resulting oscillation is known as the *localized surface plasmon* (LSP), which is a non-propagating electronic excitation confined in the finite size of the particle [3].
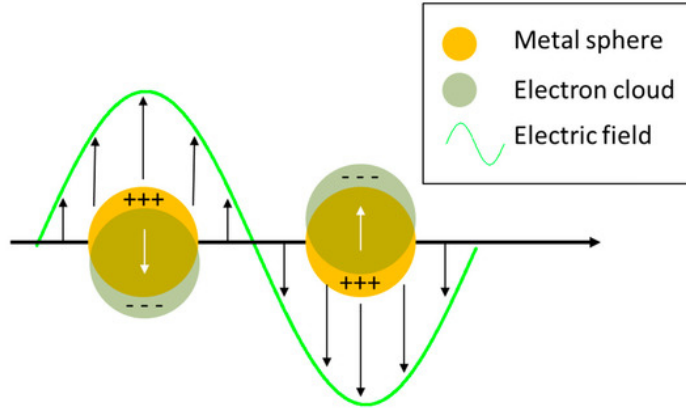
Figure 1.3: Schematic representation of the collective oscillations of electrons in metal nanoparticles under the action of an external electric field (taken from [3]).

Considering sub-wavelength nanoparticles embedded in a dielectric medium with constant $\varepsilon_d > 0$, the absorption and scattering cross-sections can be evaluated using a quasi-static approximation:

$$\sigma_{Abs.}(\omega) = 4\pi k a^3 \operatorname{Im}\left[\frac{\varepsilon(\omega) - \varepsilon_d}{\varepsilon(\omega) + 2\varepsilon_d}\right] \quad \text{and} \quad \sigma_{Scat.}(\omega) = \frac{8}{3}\pi k^4 a^6 \left|\frac{\varepsilon(\omega) - \varepsilon_d}{\varepsilon(\omega) + 2\varepsilon_d}\right|^2 \quad (1.25)$$

where k is the incident wavevector and a is the radius of the nanosphere. Moreover, the oscillating dipole induced in the nanoparticle by the external field generates an additional local field, resulting in a global field that is stronger than the incident one:

$$E_{int} = \frac{3\varepsilon_d}{\varepsilon(\omega) + 2\varepsilon_d} E_0 \quad (1.26)$$

The field enhancement, absorption and scattering are maximized under the same resonance condition, corresponding to the minimization of the denominator in equations 1.25 and 1.26. Remembering the expression for the dielectric constant in the Drude model in the high-frequency limit (equation 1.22), the maximum corresponds to the so-called *Fröhlich* condition [26]:

$$\varepsilon(\omega) \approx -2\varepsilon_d \quad (1.27)$$

Consequently, also the characteristic frequency of the localized surface plasmon for which the resonance condition is established can be found:

$$\omega_{LSP} = \frac{\omega_p}{\sqrt{1 + 2\varepsilon_d}} \tag{1.28}$$

The relative contribution of absorption and scattering depends on the diameter of the particle. In addition, size-dependent damping effects and losses caused by interband transitions due to bound electrons should be taken into account, leading to a shift and broadening of the experimental resonance condition.

The shape is another important factor affecting the plasmonic behaviour of nanoparticles and different shapes like spheres, cubes, octahedrons, prisms, rods, wires, and cages have been tested to best fit the application requirements and to obtain the largest possible enhancement [28]. In particular, gold and silver nanorods are characterized by two LSP frequencies, corresponding to transverse and longitudinal electron oscillation modes. The position of the resonance peaks depends on the ratio between the length and the diameter (i.e. the aspect ratio) of the rod. In case of silver, the transverse LSP peak is around 400 nm, while the longitudinal one moves towards larger wavelengths as the aspect ratio increases [28].

1.2.3 Electromagnetic enhancement

In a conventional Raman experiment, the Raman power (defined as the number of Stokes photons collected by the detector and converted into an electrical signal) is proportional by a constant $\mathcal{K}$ (accounting for several instrumental parameters) to the number N of illuminated molecules, to the Raman cross-section σ_k of the kth normal mode, and to the incident laser intensity I [3]:

$$P_{Raman}(\omega_R) = \mathcal{K}N\sigma_k I(\omega_L) \tag{1.29}$$

The SERS power is related to the normal Raman power through the global enhancement factor G_{SERS}, which can be further expressed as the product between an electromagnetic enhancement factor G^{Em} and a chemical enhancement factor G^{Chem}:

$$P_{SERS}(\omega_R) = G_{SERS}P_{Raman}(\omega_R) = G^{Em}G^{Chem}P_{Raman}(\omega_R) \tag{1.30}$$

The electromagnetic enhancement originates from the resonant excitation of LSPs in the nanoparticles and provides the strongest contribution, up to 10^{10}. It is independent of the type of molecule and does not require the direct absorption of the molecular species onto the metal [3]. In the proximity of the metallic surface (within 1-10 nm),

the molecule feels a local field E_{loc} that is much stronger than the incident one. Since the radiated Raman power is proportional to the square modulus of the electric field, the larger the local field, the higher the SERS power. As a result, an EM enhancement factor can be defined accounting for the intensification of both incident and scattered fields:

$$G^{Em} = M_{loc}(\omega_L)M_{loc}(\omega_R) = \left|\frac{E_{loc}(\omega_L)}{E(\omega_L)}\right|^2 \left|\frac{E_{loc}(\omega_R)}{E(\omega_R)}\right|^2 \qquad (1.31)$$

Considering a simple system of a molecule at distance d from a sphere of radius a, the EM enhancement factor can be written as [2]:

$$G^{Em} = \left|\frac{\varepsilon(\omega_L) - \varepsilon_d}{\varepsilon(\omega_L) + 2\varepsilon_d}\right|^2 \left|\frac{\varepsilon(\omega_R) - \varepsilon_d}{\varepsilon(\omega_R) + 2\varepsilon_d}\right|^2 \left(\frac{a}{a+d}\right)^{12} \qquad (1.32)$$

When the resonance condition of equation 1.27 is met, G^{Em} tends to infinite. Common EM factors are in the order of 10^6-10^7, but factors as large as 10^{11}-10^{12} can be predicted in correspondence of highly-localized regions of the SERS substrate, like sharp tips and nanogaps, known as *hot spots* [2, 3]. Thanks to the synergistic interaction between the polarization effects on different nanoparticles, the enhancement factor in these spatially localized spots can be orders of magnitude larger than the average one.

1.2.4 Chemical enhancement

An additional contribution to the global enhancement in a SERS experiment is provided by the chemical (or electronic) enhancement, which originates from any modification in the polarizability of a molecule because of chemical-physical interactions with the substrate. This kind of enhancement strongly depends on the molecule and requires direct adsorption, resulting in a smaller contribution (10^2-10^4) to the total intensification [3].
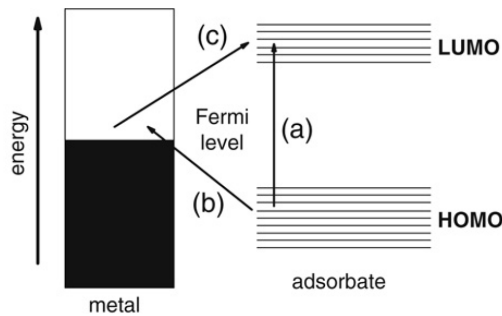
Figure 1.4: Energy level diagram for a molecule-metal complex (taken from [1]).

Several mechanisms have been investigated and the debate is still not concluded. However, the so-called *charge-transfer* mechanism is one of the most probable effects and can arise in different ways depending on the specific chemical configuration [1]:

- Type I does not require a covalent bond between the molecule and the metal, but simply a physisorption. The weak van der Waals forces are responsible for a slight perturbation of the geometrical and electronic structure of the molecule, resulting in a small modification of the Raman polarizability.

- Type II occurs when a metal-adsorbate complex is formed by a direct covalent bond. Because of the electronic coupling and the overlap of molecular orbitals, new electronic states and new indirect transitions can appear, producing a considerable modification of the molecular polarizability. This effect is even stronger when the new electronic states are in resonance with the excitation laser.

- Type III involves photo-driven charge transfer between the molecule and the metal and occurs when the energy difference between the Fermi level of the metal and the HOMO/LUMO of the molecule is matched by the exciting radiation.

Overall, the modified polarizability becomes more resonant with the laser than the initial one, leading to an increase of the Raman cross-section with respect to the free molecule. Therefore, the chemical enhancement factor can be defined as follows [3]:

$$G^{Chem} = \frac{\sigma_k^{Ads.}}{\sigma_k^{Free}} \qquad (1.33)$$

The evaluation of the chemical contributions to the SERS enhancement is very difficult and additional factors such as the molecule orientation and the presence of ions in the electrolyte should be considered. Computational methods like DFT and molecular dynamics can be used to provide a theoretical justification [1, 3].

1.2.5 Fluorescence issues

The fluorescence emission from the analyte or from impurities can be so intense and spread over a wide range of wavenumbers to completely cover up the Raman signal, especially during RRS measurements [1, 3]. This problem is partially attenuated in SERS, as metals tend to promote non-radiative decay mechanisms, resulting in fluorescence quenching [2, 3]. In addition, the enhancement of the fluorescent background during a SERS experiment is smaller by 4-5 orders of magnitude with respect to the enhancement of the Raman lines, allowing the clear identification of any peak even in resonant conditions (SERRS, i.e. Surface-Enhanced Resonance Raman Scattering) [1].

However, fluorescence may still be an issue when it is originated from impurities or analytes that are not adsorbed onto the metallic substrate. The use of exciting radiations in the NIR can mitigate the problem, reducing the probability of optical transitions to occur [3].

1.3 UV-VIS optical spectroscopy

Ultraviolet-visible spectroscopy exploits molecular absorption of radiation in the UV-VIS range (approximately between 190 and 800 nm) for the identification of organic and inorganic compounds, for the characterization of samples and for quantitative analysis on solutions and gases [29]. UV and VIS photons have enough energy to promote transitions between electronic states and information about the electronic structure of a compound can be gained. Selection rules can help one predict which transitions are allowed or forbidden. The inspection of UV-VIS spectra allows the investigation of the effect of molecular geometry, functional groups and solvent on electronic transitions, especially when organic species are considered. In addition, UV-VIS spectroscopy is a common technique to probe the plasmonic behaviour of metallic colloids, highlighting the resonance frequency for absorption and scattering.

1.3.1 Transmission UV-VIS

In transmission configuration, polychromatic radiation emitted by two separate sources (typically, a halogen lamp for the visible component and a deuterium lamp for the UV component) passes through a transparent cuvette containing the sample. In order to compensate for reflection losses and absorption by the cuvette and the solvent, the transmitted beam is compared at the detector with a beam emerging from a reference cuvette containing the solvent only. After proper corrections and subtractions, the absorption spectrum as a function of wavelength is provided in terms of *absorbance A*, defined by equation 1.34:

$$A = -\log(T) = \log\left(\frac{I_0}{I}\right) \tag{1.34}$$

where T is the transmittance, I_0 is the incident intensity and I is the intensity attenuated by the sample. The absorbance can be empirically correlated to the molar concentration $[c]$ of the absorber by the Lambert-Beer's law:

$$A = \varepsilon[c]b \tag{1.35}$$

where ε is the molar extinction coefficient and b is the optical path during which attenuation occurs. The linear relationship between absorbance and concentration is valid only at low analyte concentration (< 0.01 M [29]), as deviations from the direct proportionality can be registered at larger concentrations. For most instruments, quantitative reliable detection is feasible for absorbance between 0.1 and 1, while values larger than 1 are typically unreliable and require sample dilution.

1.3.2   Reflectance UV-VIS

Samples like powders, thick films or aggregates cannot be probed in transmission, therefore reflectance measurements could be considered as an alternative. When light is reflected at a dull surface, both specular and diffuse reflection occur: in addition to light reflected at an angle equal to the angle of incidence, some photons penetrate in the sample and, as a result of scattering and refraction processes, are reflected back in any direction. Unlike specularly reflected light, diffusely reflected radiation has undergone partial absorption and provides information about the electronic structure of the sample [30, 31].

A typical diffuse reflectace UV-VIS setup is shown in figure 1.5, in which an optical accessory known as the integrating sphere is used to collect photons that are reflected in any direction. After passing through an input port, the incident beam interacts with the sample and diffused photons are gathered by the sphere and analysed by a detector connected to an output port. The inner walls of the sphere are coated with a highly-reflective material, such as $BaSO_4$ or PTFE (*Spectralon*), which is able to reflect all the wavelengths of interest with a nearly ideal Lambertian distribution. A specular reflectance sink can be added to reduce the contribution from specularly reflected light, which is responsible for noise, low accuracy and spectral artefacts. Before starting the measurement, a reference baseline is recorded using the white reflecting material of the sphere as a standard [30, 31].
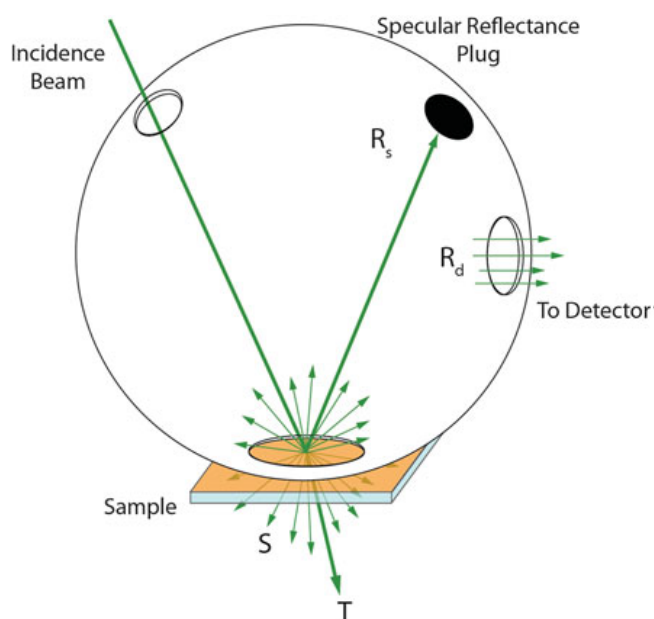
Figure 1.5: Integrating sphere for diffuse reflectance UV-VIS measurements. Image taken from [30].

The most used model to correlate diffuse reflectance to absorption coefficient and analyte concentration is the Kubelka-Munk equation:

$$f(R) = \frac{(1-R)^2}{2R} = \frac{\alpha}{S} = 2.303 \cdot \frac{\varepsilon C}{S} \tag{1.36}$$

where $f(R)$ is the Kubelka-Munk function, R is the relative diffuse reflectance, α is the absorption coefficient, S is the scattering coefficient, ε is the molar extinction coefficient and C is the analyte concentration. This linear approach is valid as long as S is constant [31].

Chapter 2

Analytes: Selected AEDs

Epilepsy is a chronic neurological disorder affecting about 40 to 70 million people world-
wide. Characteristic features of epilepsy are sudden and persistent seizures caused by
the absence or the excess of electrical signal in the brain cells, leading to convulsions,
lapses of consciousness and unexpected movements in the body. Several types of epi-
leptic disorders exist, caused by brain defects, head trauma, infections, stroke, tumours,
or genetic anomalies [32, 33]. Nowadays, long-term seizure control can be achieved in
most cases thanks to the regular intake of specific and effective anti-epileptic drugs
(AEDs); however, the current drug therapy is either unsuccessful or intolerable for
about 20-30% of patients, whose epilepsy is considered treatment refractory. In addi-
tion, side effects or contraindications, which are strongly related to the AED, to the
patient clinical status and to interactions with other drugs, may reduce the number of
AEDs that can be used in individual cases [33, 34]. Therefore, novel AEDs with dif-
ferent mechanisms of action, broad spectrum of efficiency, high tolerability and safety
are continuously searched for [33].

2.1 Perampanel

Glutamate is the main excitatory neurotransmitter in the brain and plays a key role in
triggering, maintaining, and spreading epileptic activity. Indeed, an increased concen-
tration of extracellular glutamate has been detected in the hippocampus of epileptic pa-
tients during seizures [33, 35]. Alpha-amino-3-hydroxy-5-methyl-4-isoxazolepropionic
acid (AMPA) receptors have been studied for decades because they act on glutamate-
mediated excitatory neurotransmission and they appear critical to seizure-generated
neuronal injury, epileptogenesis and seizure generation and spread [33, 35, 36]. AMPA
antagonists (i.e. small molecules that could bind to AMPA receptors inhibiting their
action) may be exploited as innovative AEDs, even if they possess some intrinsic draw-

backs that have hindered their development as valid drug candidates [36]. For example, NBXQ, the prototype of AMPA-receptor antagonists, is characterized by poor solubility, while its polar derivatives exhibit weak efficacy and decreased blood-brain barrier penetration [37]. Talampanel has demonstrated a positive signal in epilepsy, but its half-life is so short (approximately 3 hours) that multiple daily dosing is required, resulting in a sharp rise of drug concentration and in increased incidence and severity of adverse side effects [36, 37]. To overcome the critical issues mentioned above, an extensive and in-depth program was carried out at *Eisai Research Laboratories* in Japan, focusing on new chemical structures for AMPA receptor antagonists. Several compounds were examined and the investigation into the structure-activity relationship by molecular manipulation culminated in the discovery of the first clinically available AED acting on AMPA receptors: 2-(2-oxo-1-phenyl-5-pyridin-2-yl-1,2-dihydropyridin-3-yl)benzonitrile, known as Perampanel or with the commercial name of *Fycompa*® [35–37]. Perampanel is a novel, orally active, highly selective, non-competitive AMPA receptor antagonist authorized as an adjunctive therapy for the treatment of partial-onset seizures in epileptic patients aged 12 years and older in more than 55 countries (including EU and USA in 2012, Canada, Russia, and Switzerland) [33, 35].

Perampanel exerts a non-competitive antagonist action, i.e. it binds at a different site with respect to glutamate, which results in a larger effectiveness at lower doses and even under increased excitation when the agonist concentration is high [33, 37]. Perampanel is characterized by a long half-life (70-100 hours) and relatively high bioavailability, and its concentration in the plasma rises gradually at constant dose, reducing the risk of adverse effects and increasing the tolerability above 10 mg, with a recommended dosage between 2 and 12 mg once daily [34–36]. The adverse effects, especially dizziness and somnolence, are comparable to those of other well-established AEDs and the high selectivity towards AMPA receptors reduces the probability of psychoactive effects due to the interaction with other kinds of receptors [34, 35, 37]. However, late-occurring severe side effects may still be unknown and long-term studies are needed [34]. Finally, the favourable pharmacokinetics and the minimal interactions allow the synergistic increase of the efficacy by combining Perampanel with other AEDs like Carbamazepine, Lamotrigine, and Valproate, leading to a rational individualized polytherapy and to minimized side effects [33, 36].

2.1.1 Molecular characterization of Perampanel

Perampanel (PER) is available as a white-yellowish non-hygroscopic powder, almost insoluble in water at neutral pH [38]. Solid PER exhibits polymorphism and exists in several crystalline forms, both anhydrous and hydrate, depending on the production

method. Different polymorphs of the same compound are not identical and may possess different physical, chemical, and pharmaceutical properties, such as dissolution rate, solubility, bulk density, melting point, thermal and chemical stability, and shelf-life. This is the reason why various polymorphic forms are identified and characterized in [39] by means of X-ray diffraction (XRD), differential scanning calorimetry (DSC), thermogravimetric analysis (TGA), Fourier transform infrared spectroscopy (FTIR) and Raman spectroscopy. For example, a comparison of the X-ray powder diffraction (XRPD) patterns of four crystalline PER forms is reported in figure 2.1.
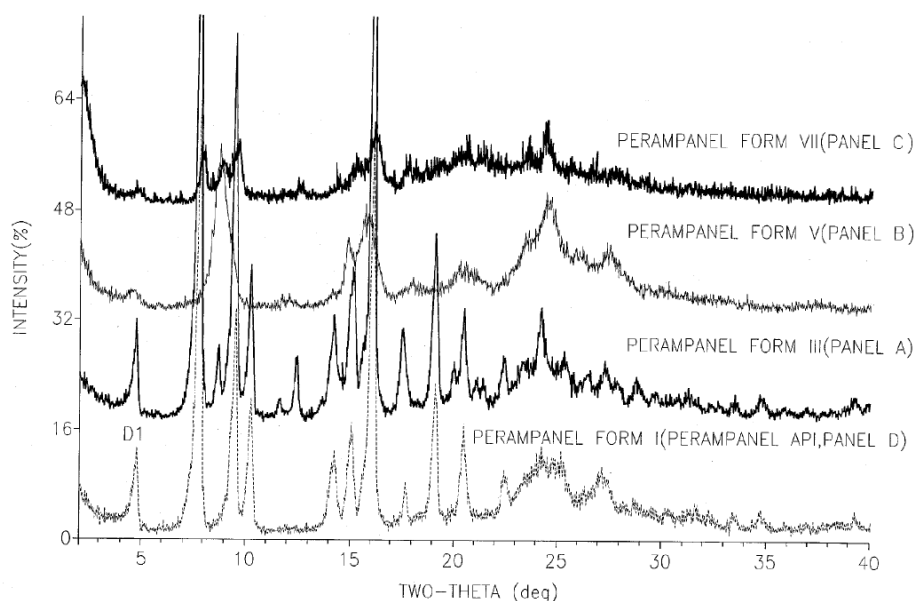
Figure 2.1: Comparison of XRPD patterns of four crystalline PER polymorphs (taken from [39]).

The active substance is 3/4 hydrate PER (molecular weight = 362.90 g/mol) and is available in film-coated tablets containing 2, 4, 6, 8, 10 and 12 mg of the drug [38]. The molecular structure of PER is depicted in figure 2.2.
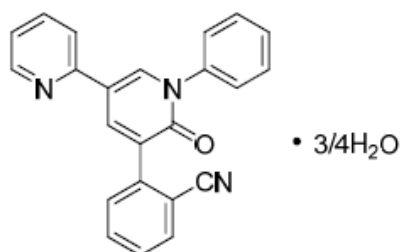
Figure 2.2: Chemical structure of $C_{23}H_{15}N_3O \cdot 3/4\ H_2O$ (taken from [38]).

In recent years, quantum chemical calculations by means of DFT, molecular modelling and conformational analysis were carried out in order to understand the biological behaviour of PER and its accommodation in the binding site of AMPA receptors [40].

The planarity of its moieties, the influence of the pyridine nitrogen and cyano group, and the formation of hydrogen bonds were highlighted and the results may contribute to the design of novel AEDs [40].

In the previous master's theses by N. Villa [8] and L. Giuliani [9], both solid PER and PER solutions have been characterized through UV-VIS and Raman spectroscopy, in order to identify the main molecular markers and to investigate the best conditions for SERS sensing. The most important outcomes of both theses are summarized in the next paragraphs. Villa collected the Raman spectra of pure solid PER powder using three different laser wavelengths, i.e. 458 nm, 514 nm and 785 nm. Fluorescence emission was dominant at 458 nm and the assignment of the main vibrational modes was performed using the spectrum obtained with 785 nm excitation, which is reported in figure 2.3.
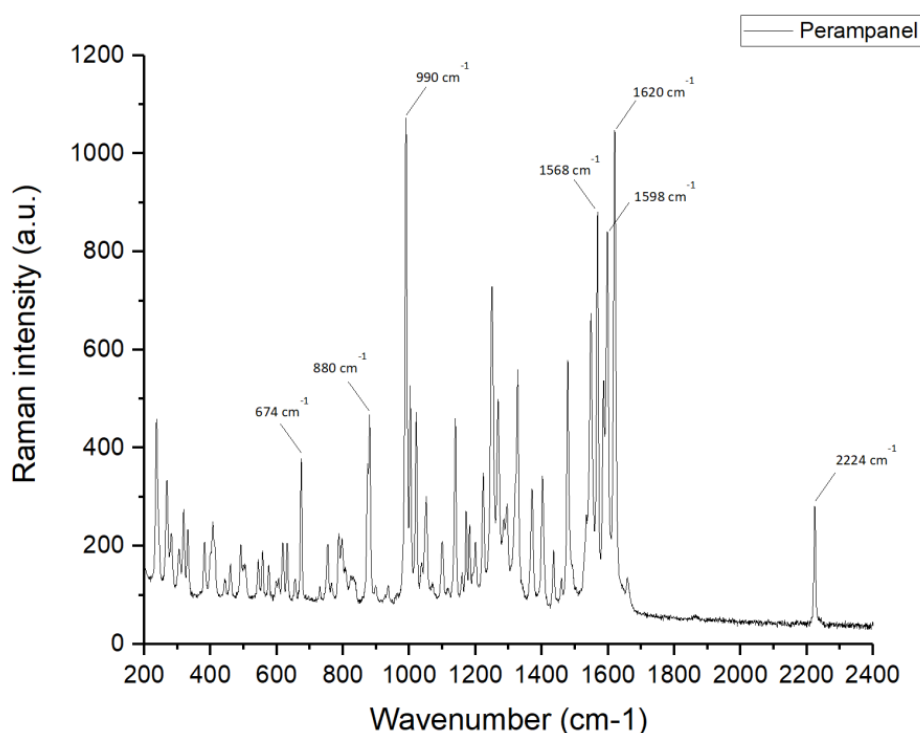
Figure 2.3: Raman spectrum of a PER powder sample (excitation wavelength: 785 nm; power: 10 mW; exposure time: 10 s, 3 averages). Image taken from [9].

The comparison between the low-wavenumber region of the recorded Raman spectrum and the FT-Raman spectrum reported in [39] allowed Villa to identify the specific PER sample with PER polymorphic form VII, even if some discrepancies were present [8]. Based on Density Functional Theory calculations (DFT B3LYP/6-31G(d,p)), the main vibrational modes of PER were assigned, as reported in table 2.1 [6, 12].

Wavenumber (cm^{-1})	Mode
670	Collective in-plane C-H bending
875	Collective out-of-plane C-H bending of the three outer rings
1000	Trigonal ring deformation of the three outer rings
1018	Ring deformation
1135	Collective in-plane C-H bending of the ring carrying the CN
1568, 1598, 1620	Aromatic ring stretching mode
2224	C $\equiv$ N bond stretching

Table 2.1: Assignment of PER main vibrational modes (after [12] and [6]).

Most of the characteristic features in table 2.1 were observed also in the SERS spectra of PER recorded on gold and silver substrates at different drug concentrations. Some changes in the relative intensities and slight wavenumber shifts were highlighted by Villa, probably caused by a change in the chemical environment during SERS experiments. Indeed, SERS measurements were performed on acidified solutions of PER in methanol, because protonation was identified as a successful way to increase the interaction with the metallic substrate and to foster the SERS activity of PER [6]. In particular, the most suitable condition for reliable SERS detection was achieved by Villa at pH=2, obtained by mixing a proper amount of hydrochloric (HCl) and sulphuric (H_2SO_4) acids in molar ratio 1:9 [8]. Sulphuric acid was required to reach the right acidification condition while reducing the total amount of chloride ions, whose excess was expected to hinder the electrostatic interaction between protonated PER and the metal nanostructures.

A comparison between the Raman spectrum of solid PER and the SERS spectrum of a 3×10^{-4} M acidified PER solution in methanol is reported in figure 2.4. The SERS signals corresponding to a collective in-plane C-H bending, combined with collective ring deformations, were considered as a fingerprint of Perampanel [6]. Specifically, SERS measurements performed later by Giuliani on gold substrates, produced by pulsed laser deposition (PLD), were able to detect the markers around 670 cm^{-1}, 880 cm^{-1} and 1000 cm^{-1} at any concentration within the therapeutic range of PER (3×10^{-7} M - 3×10^{-6} M) [9]. Giuliani also managed to push to lower concentrations, down to 3×10^{-9} M, which was identified as the lowest limit of detectability [9, 10]. On the contrary, the peak around 2224 m^{-1} and corresponding to C$\equiv$N stretching was not always clearly visible due to its low relative intensity [9].
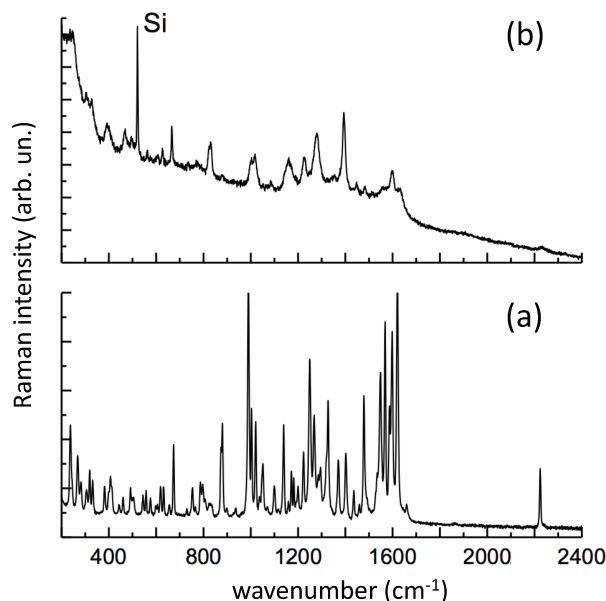
Figure 2.4: (a) Raman spectrum of solid Perampanel (laser 785 nm); (b) SERS spectrum of a 3×10^{-4} M PER aqueous solution prepared at pH=2 with a mixture of HCl:H$_2$SO$_4$ in 1:9 molar ratio (laser 458 nm). The SERS spectrum was recorded on a silver substrate prepared by ps-PLAL on a (100) silicon support (taken from [6]).

The effect of protonation and pH on PER was investigated by Villa by UV-VIS spectroscopy. The corresponding spectra were collected both in neutral methanol solutions and in acidified aqueous solutions at different PER concentrations. As expected, the results were strongly dependent on the acidification of the solution and the protonation process was observed to start at pH=3 (figure 2.5). Parallel DFT calculations showed that the possible protonation sites were on the N and O atoms of PER [8].
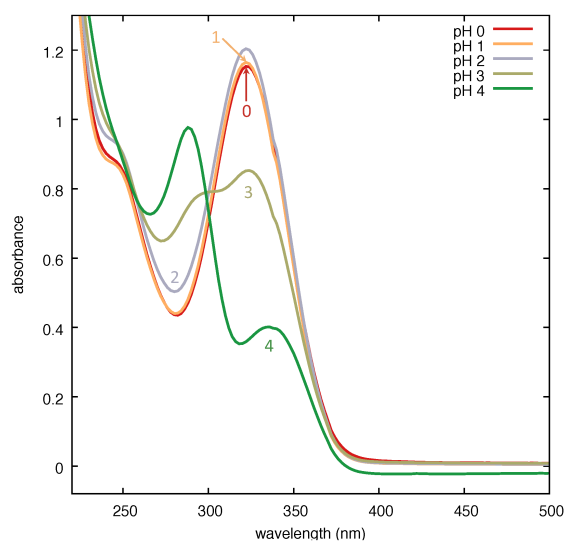
Figure 2.5: UV-VIS absorption spectra of aqueous solutions of PER 5×10^{-5} M at various pH (taken from [6]).

2.2 Cannabidiol

In the recent decades, the therapeutic and pharmacological values of cannabis-related products have been significantly explored, with both *in vitro* experiments and clinical trials. More than 565 chemical compounds have been extracted from *Cannabis Sativa* and at least 120 cannabinoids have been identified [41]. In particular, research has focused on Cannabidiol (CBD), a non-psychotropic phytocannabinoid which exhibits anti-inflammatory, anti-emetic, anti-psychotic, and anti-epileptic activity, together with good neuroprotective properties in several neurological diseases [42, 43]. Both anecdotal and scientific reports have confirmed the effectiveness of CBD as an anticonvulsant treatment, primarily for some specific epileptic syndromes in paediatric age. CBD shows effective anti-seizure activity with higher specificity, good safety profile and fewer adverse effects compared with traditional AEDs. Moreover, contrary to tetrahydrocannabinol (THC), CBD is characterized by very low addictive, hallucinogenic and toxic effects and does not exhibit euphorigenic, psychedelic and psychoactive properties [41]. The exact mechanism of action of CBD is still unclear, even if it may promote the modulation and normalization of intracellular Ca^{2+} by binding to non-cannabinoid receptors [41, 44]. CBD is highly lipophilic and practically insoluble in water, and has poor oral bioavailability. The elimination half-life is quite long, up to 2-5 days with a daily administration of 10 mg/kg/day [44].

The highly purified preparation of Cannabidiol (>98% CBD), known as *Epidyolex®*, has been developed by GW Pharmaceutical plc., and approved by both the U.S. Food and Drug Administration (FDA) in 2018 and the European Medicines Agency (EMA) in 2019 "*as adjunctive therapy of seizures associated with Lennox-Gastaut syndrome (LGS) or Dravet syndrome (DS), in conjunction with Clobazam, for patients 2 years of age and older*" [45]. The recommended dosage ranges between 2.5 and 10 mg/kg twice a day, and the individual response should be carefully monitored, especially when CBD is administered in combination with other AEDs. Indeed, several drug-drug interactions have been observed, including the most relevant ones with Clobazam (CLB) and Valproate (VPA), which may be responsible for adverse events [43]. More studies are required to better evaluate the possible drug interactions, as well as the proper dose, the risk of side effects, the effectiveness of the treatment, and the precise pharmacology, together with a thorough therapeutic drug monitoring of the serum concentrations of all the drugs involved [42, 44].

2.2.1 Molecular characterization of Cannabidiol

All the cannabinoids have a typical C_{21} terpenophenolic structure [41]. Cannabidiol, whose chemical name is 2-[(1R,6R)-3-methyl-6-(1-methylethenyl)-2-cyclohexen-1-yl]-5-pentyl-1,3-benzenediol ($C_{21}H_{30}O_2$, molecular weight = 314.5 g/mol), is basically a cyclohexene which is substituted by a methyl group at position 1, by a 2,6-dihydroxy-4-pentylphenyl group at position 3 and by a prop-1-en-2-yl group at position 4 [43, 45], as represented in figure 2.6.
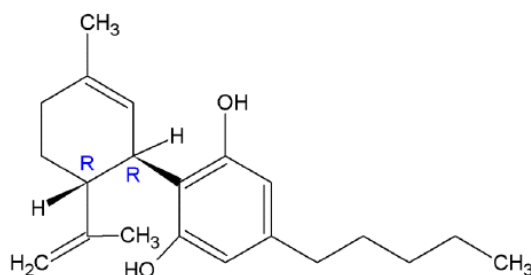
Figure 2.6: Chemical structure of Cannabidiol (taken from [45]).

Because of the presence of two chiral centres, CBD molecule exhibits stereoisomerism. In particular, two optical isomers have been identified, i.e. (−)-CBD and (+)-CBD, which differ in the stereochemistry of the bond between the resorcinol moiety and the terpene unit (figure 2.7). As confirmed by several reports, the absolute configuration of all natural CBD molecules is (−)-trans-(1R,6R), while (+)-CBD can only be obtained by synthesis [41, 46].
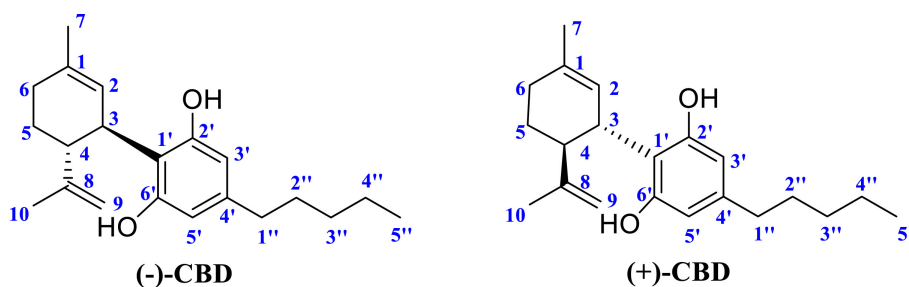
Figure 2.7: Optical isomers of CBD (taken from [41]).

Solid CBD displays a monoclinic crystalline structure, as determined by single-crystal X-ray crystallography, with an asymmetric unit cell containing two independent molecules with different orientations of the pentyl side chain [46]. The active substance of *Epidyolex*® is a white-yellow crystalline solid, which is insoluble in aqueous solutions at any pH but soluble in some organic solvents and oils. The finished product consists of an oral solution of CBD (100 mg/mL) dissolved in a lipid-based solvent, like sesame oil [45].

In a recently published study, normal Raman and SERS spectra of CBD and other analogue molecules have been collected to implement a fast and reliable method for the forensic detection of cannabis-related substances [47]. The authors collected the Raman spectra using solid crystalline powders of the drugs, while they acquired the SERS spectra from 10^{-4} M methanol solutions by exploiting silver nanoparticles as the enhancing substrate. In addition, the enhancement effect of different salts was tested, reporting that the best intensification effect of CBD signal was obtained with magnesium chloride ($MgCl_2$). All the measurements were carried out using the 633 nm excitation wavelength of a diode laser, focusing it on the sample with a $50\times$ objective, corresponding to an on-stage power of 10 mW [47]. A comparison between the SERS and normal Raman spectrum of CBD is reported in figure 2.8.
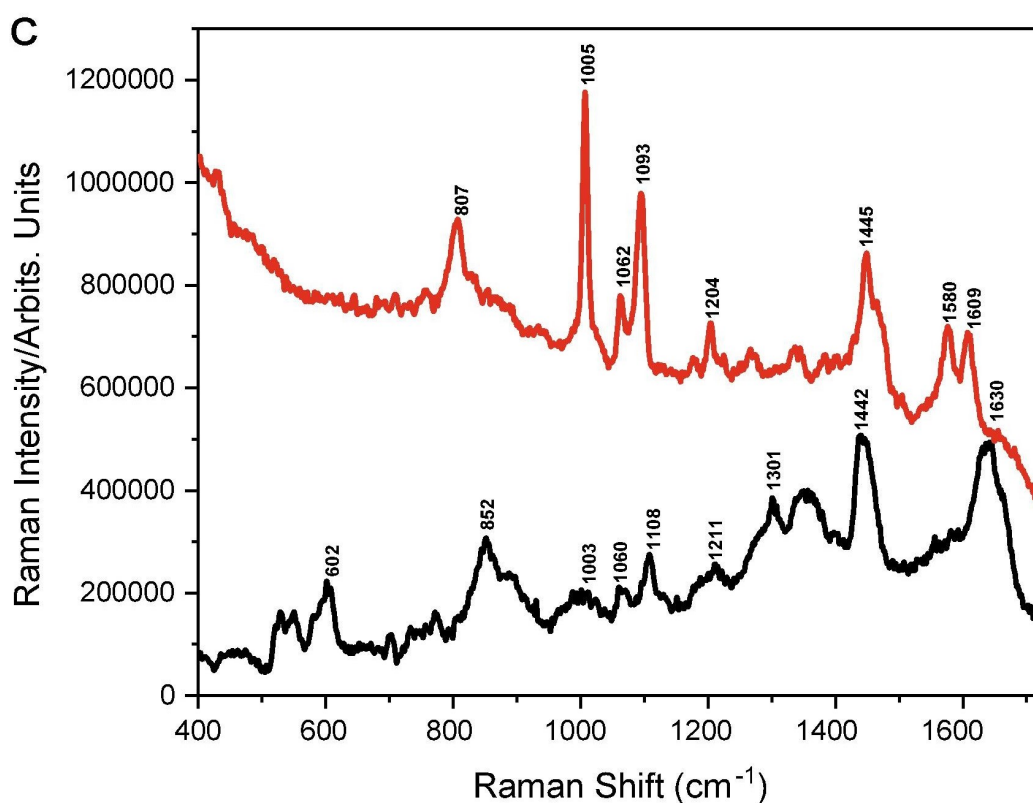
Figure 2.8: SERS spectrum (*red*) and normal Raman spectrum (*black*) of CBD (excitation wavelength: 633 nm; power: 10 mW; exposure time: 10 s, 3 averages). Image adapted from [47].

The relative intensities of the lines in the SERS spectrum are different from those in the normal Raman spectrum, as well as the position of the peaks, with a shift between 2 and 10 cm^{-1}. Strong enhancement of the peaks at 807 cm^{-1}, 1005 cm^{-1}, 1093 cm^{-1}, 1204 cm^{-1}, 1580 cm^{-1} and 1609 cm^{-1} is observed, whereas other peaks are suppressed in the SERS measurement because of the interaction between the molecule and the

substrate. To determine the adsorption geometry of CBD molecules onto the silver substrates and to make a vibrational assignment of the main peaks (as reported in table 2.2), DFT calculations were performed [47]. The authors came to the conclusion that Cannabidiol has a parallel surface geometry on silver through the benzene ring, the oxygen atoms of the OH groups and the $=CH_2$ group [47].

Raman	SERS	DFT	Mode
602		628	Benzene ring stretching; cyclohexene ring twisting; $=CH_2$ and CH_3 twisting
	807	849.63	Alkyl chain CH_2 and CH_3 twisting
852		896.97	Cyclohexene ring in-plane CH and CH_2 bending; CH_3 and $=CH_2$ wagging; alkyl chain CH_2 and CH_3 wagging
1003	1005	1036.69	Benzene ring symmetric stretching; alkyl chain CH_2 and CH_3 wagging
1060	1062	1100.12	Cyclohexene ring asymmetric stretching and twisting; CH_3 wagging; $=CH_2$ twisting
	1093	1125.78	Alkyl chain CH_2 and CH_3 wagging
1108		1157.26	Cyclohexene ring in-plane stretching and out-of-plane bending; benzene ring symmetric stretching; CH_3 wagging; OH bending
1301		1354.67	Benzene ring symmetric stretching; cyclohexene ring CH_2 and CH wagging; alkyl chain CH_2 wagging
	1580	1611.19	Benzene ring symmetric stretching; OH in-plane bending
	1609	1661.42	Benzene ring symmetric stretching; OH in-plane bending
1630		1684.16	C=C stretching ($=CH_2$); CH wagging ($=CH_2$); CH_3 twisting

Table 2.2: Assignment of CBD main vibrational modes (after [47]). The experimental wavenumbers from normal Raman and SERS experiments are compared with the theoretical values derived from DFT (all the values are reported in cm^{-1}).

2.3 The usefulness of therapeutic drug monitoring

Therapeutic drug monitoring (TDM) is a clinical procedure used to determine the concentration of a drug in the blood, plasma, serum or, recently, also saliva [20] of a patient. TDM is primarily aimed at optimizing and tailoring the individual drug dosage to achieve the best possible therapeutic response with minimal risks and adverse effects

[5, 48]. This practice is particularly relevant for drugs with a narrow therapeutic index and large inter-individual variability, such as anti-epileptic, anti-cancer, psychiatric and immunosuppressant drugs, for which even small fluctuations in the drug concentration may result in negative effects: when the drug concentration is too small, it could be subtherapeutic or ineffective; on the other hand, when the drug concentration is too high, the incidence of toxicity and adverse effects might increase [5, 48, 49].

Regarding AEDs, the optimal dosage should ideally lead to complete seizure prevention with no negative effects and TDM should be performed at the beginning of the treatment or when it is modified [5], especially in the case of complex therapies involving multiple drugs. The relationship between the plasma levels of AEDs and the clinical effects has been clearly demonstrated and, sometimes, the optimal therapeutic range for individual patients may be significantly different from the reference therapeutic range reported in the literature [49, 50]. For instance, the reference plasma concentration of Perampanel ranges between 180 and 980 μg/L (about 5×10^{-7} - 3×10^{-6} M) [50], but side effects tend to increase with increasing dosages and PER is susceptible to drug-drug interactions which may reduce its concentration in a dose-dependent way. In addition, a careful monitoring should be carried out during pregnancy and after birth [51]. A similar situation also holds for Cannabidiol, whose use along with Clobazam requires TDM before administration of CBD and after each dosage increase [42].

Currently, the techniques employed in clinical laboratories for TMD are the immunoassays and the High Performance Liquid Chromatography (HPLC) combined with mass spectrometry, which are very sensitive and reliable. However, they are typically expensive and require long waiting times and significant amount of blood. Therefore TDM is not very widespread and novel complementary techniques are welcome to combine analytical capability with lower cost and a shorter time. Efficient SERS sensors with high sensitivity and spatial uniformity may represent a valuable complementary technique, even if current research is still in its early stage and many important challenges have to be addressed before applying SERS technology to clinical practice [4, 5]. Among others, the production of standardized substrates according to precise guidelines, the maximization of the repeatability at reasonable cost, the improvement of reliable quantitative detection, the definition of standard methods for data analysis and calibration, the intrinsic chemical complexity of biofluids, and the ease of use and interpretation of the results should be carefully considered [4].

Chapter 3

Production of Ag SERS Substrates

During a SERS experiment, molecules adsorb on properly designed metallic nanostructures able to provide a strong intensification of the Raman signal by means of *surface plasmon resonance* (SPR) [1]. Nanostructured substrates made of aggregates of noble metals like gold and silver exhibit the best optical properties and are the most used materials for plasmonic applications. Indeed, gold and silver operate in the visible range of the spectrum, with an absorption peak around 520 and 410 nm, respectively, and show the most intense electromagnetic enhancement, in many cases combined with a chemical intensification mechanism [5]. Different techniques can be used to fabricate such SERS substrates; in my thesis work, I used a chemical method based on colloidal synthesis of silver nanoparticles, which were subsequently deposited onto filter paper supports.

3.1 Colloidal synthesis

Metallic colloidal dispersions are systems in which metal nanoparticles of different size are distributed in a liquid phase; the dimension of the particles, in the range of tens to hundreds of nanometres, is sufficiently small to avoid precipitation but big enough to scatter light. Colloidal systems made of noble metals are characterized by a strong colouration given by the absorption of visible light. The starting point for the chemical synthesis of colloidal metals is the dissolution of a metal precursor into distilled water, typically a metallic salt. Then, two other components are necessary to obtain the desired nanoparticles, i.e. a reducing agent and a stabilizer: the former reduces the metallic ions released by the salt promoting the growth of the particles, while the latter prevents the agglomeration and sedimentation of nanoparticles by creating a mechanical or electrostatic barrier on the dispersed phase. In this case, silver particles were prepared using trisodium citrate (TSC) as reducing agent, which ensures a high

yield and also acts as a stabilizer. Unreacted citrate anions and oxidation products adsorb on the surface of the forming metallic nanoparticles, creating a charged layer against aggregation [52]. Reduction by citrate is promoted only at relatively high temperatures, close to the boiling point of the solution.

Silver colloids were prepared according to the procedure (c) reported in [53], known as the Lee-Meisel method. The metallic precursor is silver nitrate ($AgNO_3$ 99.8-100%, CAS: 7761-88-8), while the reducing agent/stabilizer is TSC ($C_6H_5Na_3O_7 \cdot 2H_2O \geq$ 99.0%, CAS: 6132-04-3). Both chemicals were purchased from *Sigma-Aldrich*.
The procedure is summarized in the following:

- 72 mg of $AgNO_3$ were dissolved in 400 mL of distilled water into a glass flask;

- 80 mg of TSC were dissolved in 8 mL of distilled water into a glass beaker. The resulting concentration of TSC is 1%;

- Both solutions were separately heated up on a heating plate and mixed when the boiling point was reached;

- The resulting solution was kept boiling for 45 minutes to promote the reaction and it was continuously agitated through a magnetic stir bar. The solution was initially uncoloured and transparent but, as soon as the nanoparticles started nucleating and growing, it turned greenish-yellow with a dull appearance (figure 3.1);

- At the end of the reaction, the solution was cooled down to room temperature while keeping the stirring.

In order to avoid impurities and heterogeneous nucleation on the surface of the glass flask, all the glassware had been thoroughly cleaned with nitric acid (HNO_3 64-66%, CAS: 7697-37-2, *Sigma-Aldrich*) and rinsed with distilled water before the preparation of the colloid. Solvent loss because of evaporation was reduced by covering the flask during boiling.

Once cooled, the colloid was concentrated by means of a centrifuge (*Hettich Eba 21*); six glass vials were filled with 8 mL of colloid and centrifuged for 10 minutes at 5000 RPM (acceleration ramp: level 5; deceleration ramp: level 2). Large and heavy nanoparticles and aggregates settled at the bottom of the vials, while the supernatant became clear and transparent. Using a pipette, the supernatant of each vial was gradually removed ($\approx$ 7.5 mL), while the remaining colloid ($\approx$ 0.5 mL) was agitated and picked up. At the end of the process, about 300 mL of clear supernatant and 25 mL of concentrated

colloid were obtained. During my thesis, the synthesis and concentration process has been replicated three times, trying to maintain all the experimental parameters as constant as possible.
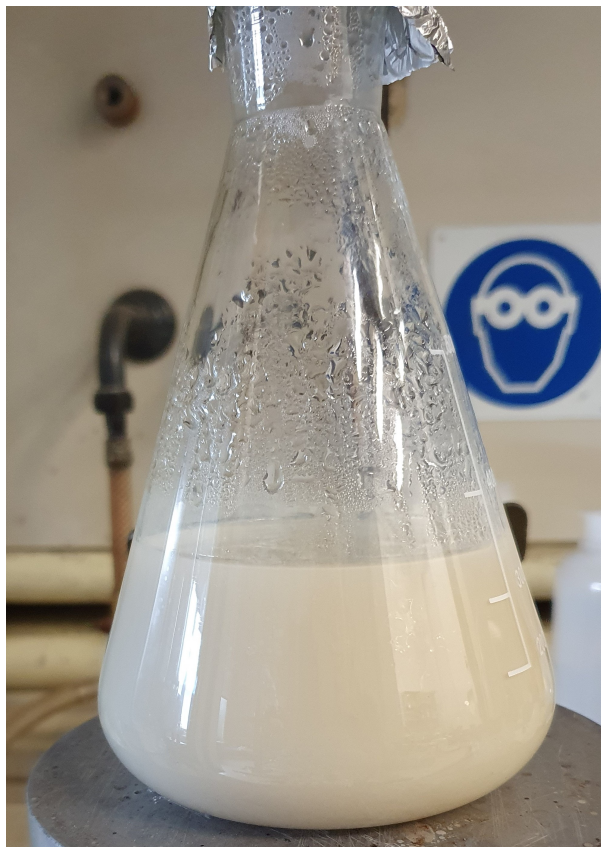
Figure 3.1: Silver colloid prepared according to the Lee-Meisel method.

3.2 UV-VIS characterization of the produced silver colloid

The silver colloid was characterized by means of UV-VIS spectroscopy. Two quartz cuvettes (optical path = 1 cm) were accurately cleaned with propanol and acetone and rinsed with distilled water, then a baseline was acquired with both cuvettes filled with water. UV-VIS spectra were recorded using a Jasco V-570 spectrophotometer and processed with the *Spectra Manager* software.

The spectra of the concentrate and of the supernantant are reported in figure 3.2. The SPR is peaked at 407 nm for the supernatant and shifted to 422 nm for the concentrate; as expected, the presence of larger particles in the concentrated colloid shifts the resonance condition to higher wavelengths and contributes to the broadening

of the peak up to 800-1000 nm. The broad shape of the absorption spectrum of the concentrate is an indication of the presence of nanospheres with different sizes and of nanorods. Indeed, the longitudinal plasmon resonance of nanorods is located at larger wavelengths and it spans from the visible to the near-infrared depending on the aspect ratio [54]. The simultaneous incidence of nanospheres and nanorods results in larger SERS enhancements and allows the use of an excitation frequency far from the absorption peak [7, 8].
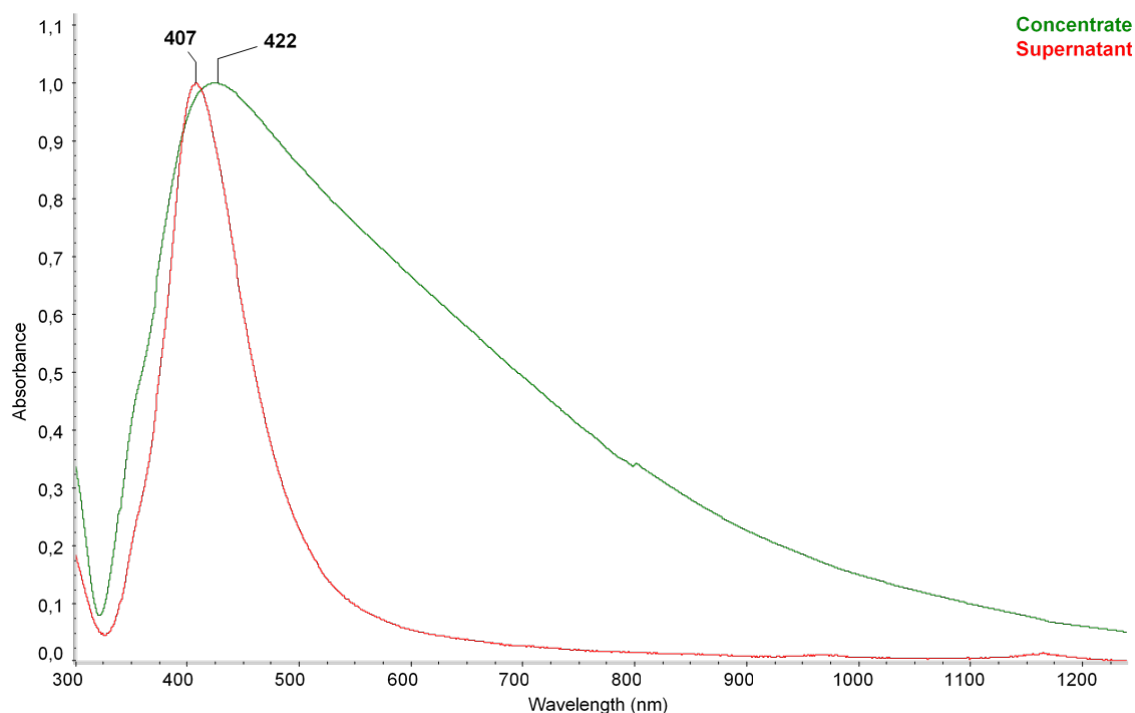
Figure 3.2: UV-VIS absorption spectra of colloidal silver concentrate (diluted 1 to 50 in distilled water) and supernatant. The intensity of both plasmon peaks is normalized to 1.

It is important to highlight that, because of aggregation, the position of the SPR and the shape of the UV-VIS spectrum of the colloid after deposition will be significantly different from that reported in figure 3.2. This point will be discussed further in section 3.5.

3.3 Preparation of Ag-based substrates by natural sedimentation

SERS substrates were first prepared by depositing the silver nanoparticles onto filter paper supports, slightly modifying the dip-coating procedure reported in [15]. The filter paper was purchased from *Colaver s.r.l.* (Via dell'Artigianato 23, 20090 Vimo-

drone, Milan) in the form of 50×50 cm² sheets, with a grammage of 67 g/m² and a thickness of 135 μm (Cod: 29SF6081).

Pieces of 4×5 mm² of paper were cut out of the sheet and thoroughly cleaned with water and ethanol to remove, respectively, undesired salts and organic contaminants. Then they were dried at room temperature under a fume hood. The pieces of paper were placed on the bottom of 3 mL glass vials and covered with 1 mL of concentrated silver colloid; before the use, the concentrated colloid was vigorously agitated, in order to make it uniform and homogeneous. The vials were stocked for 3 days in dark and at room temperature, in order to promote the natural sedimentation of the nanoparticles on the paper. After the incubation, the supernatant and the excess of colloid were carefully removed without touching the substrates, which were dried for one hour under the hood and stored in air until their use (figure 3.3).
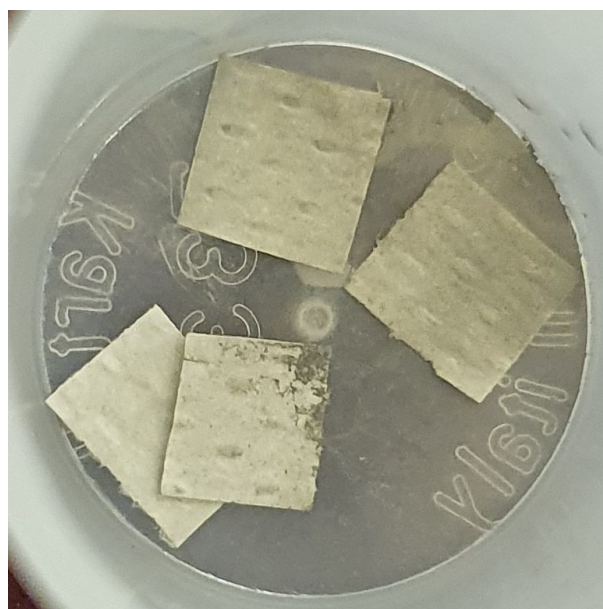
Figure 3.3: Four substrates after incubation and drying. The yellow-grey colour of the paper is an indication of the presence of silver nanoparticles.

The substrates were analysed with the Olympus SZX16 stereo-microscope available at the WIBIDI Lab (Energy Dept., PoliMi). Such microscope is equipped with the Olympus SDF PLAPO 1XPF objective and with LC30 digital colour camera connected to a computer. The sample was illuminated from the bottom by a LED and an optical zoom provided magnification in the range 0.7× - 11.5×. Some details of the substrates are shown in figures 3.4 - 3.9.
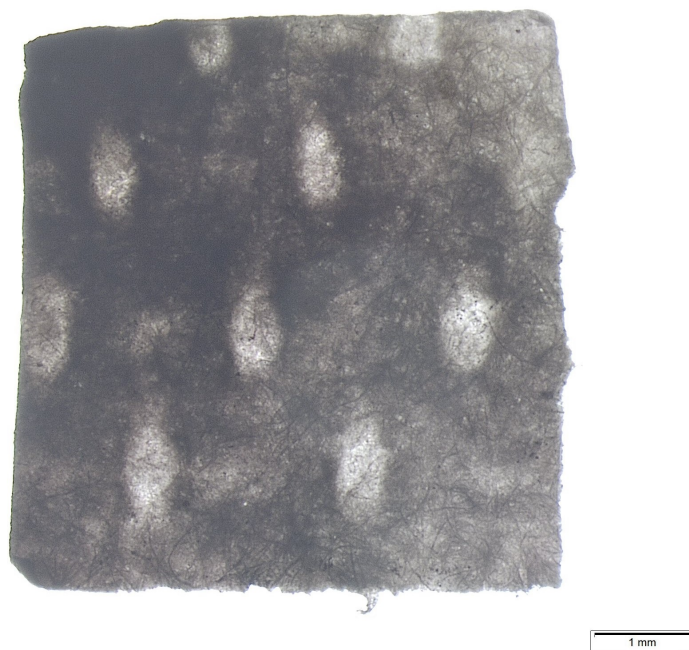
Figure 3.4: Optical image of one of the substrates (0.7×), highlighting the characteristic pattern of imprints on filter paper.
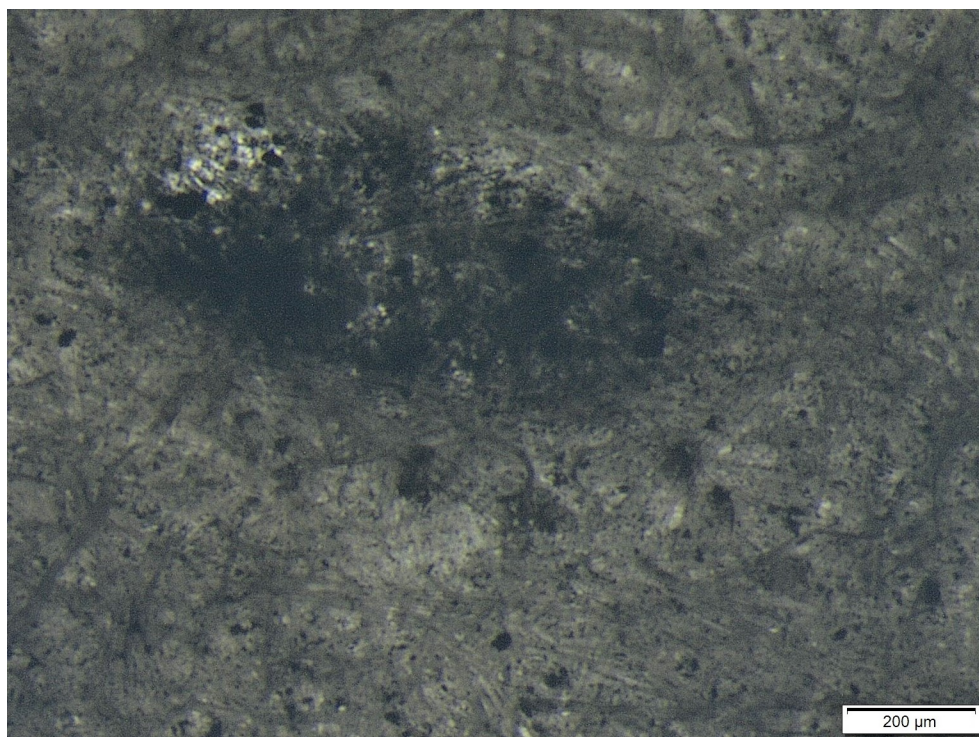
Figure 3.5: Optical image of one of the substrates (3.2×).
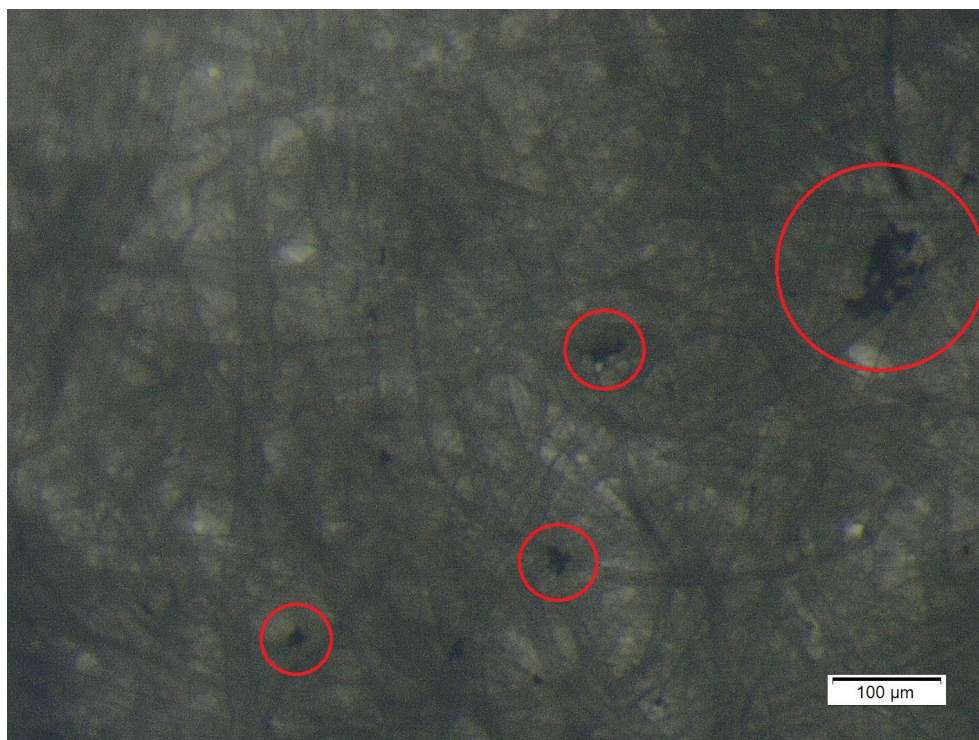
Figure 3.6: Optical image of one of the substrates (5×). The dark spots observed among the paper fibres (highlighted by red circles) correspond to aggregates of metallic silver.
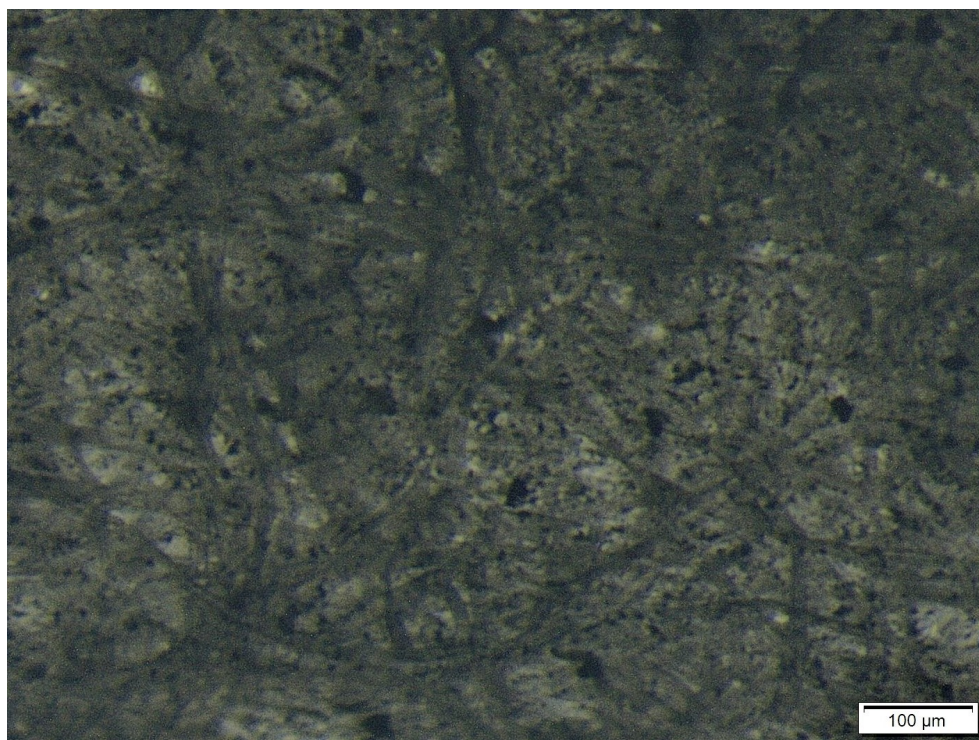
Figure 3.7: Optical image of one of the substrates (5×).
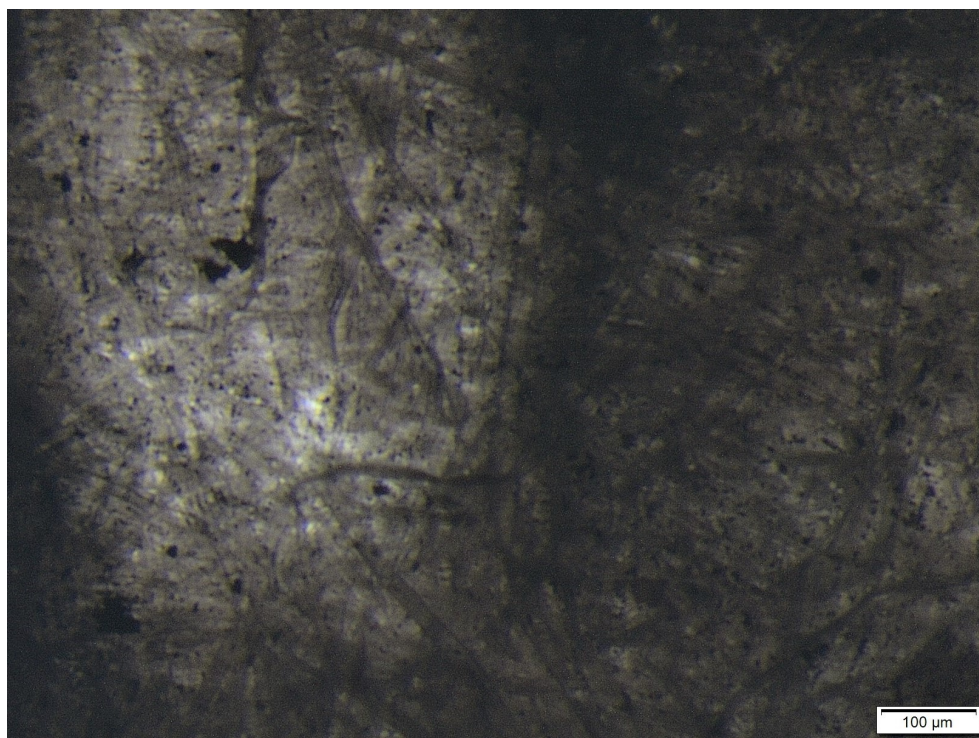
Figure 3.8: Optical image of one of the substrates (5×).
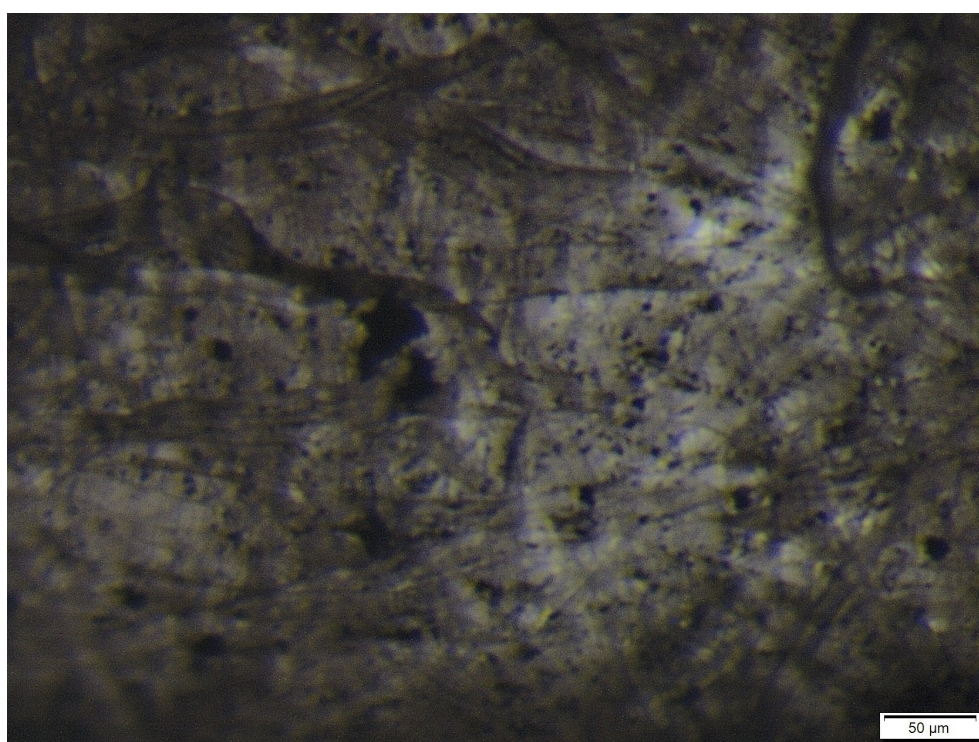
Figure 3.9: Optical image of one of the substrates (10×).

The fibrous structure of the paper is clearly visible at any magnification, with fibres having a characteristic size of some tens of μm. The dark spots attached to the fibres,

highlighted at larger magnifications, are μm-sized aggregates of silver nanoparticles, which are responsible for the SERS behaviour of the sensor. In figure 3.4, the substrate displays a highly non-uniform surface with a pattern of cavities and depressions; accordingly, the problem related to the spatial uniformity of the sensors should be carefully addressed during SERS measurements.

The production method that has just been presented and that is reported in [15] is very time-consuming because of the incubation period. In order to shorten the preparation process to make it feasible in common practice, an alternative production cycle was investigated and tested, as discussed below.

3.4 Preparation of Ag-based substrates by centrifugation

After cutting, cleaning and drying the filter paper as described in the previous paragraph, the 4×5 mm² pieces were placed on the bottom of 8 mL glass vials and covered with 2 mL of concentrated colloid. The vials were then centrifuged for 20 minutes at 5000 RPM, exploiting the centrifugal force inside *swing-out* rotors to directly press the nanoparticles onto the paper. After removing the transparent supernatant, the pieces of paper (SERS substrates) were extracted and dried under a fume hood. As shown in figure 3.10, the substrates produced using the centrifuge are darker than those obtained by natural sedimentation, which may indicate a larger amount of silver and a better SERS sensing behaviour.

Figure 3.10: Two dried substrates produced by centrifugation.

However, the first SERS tests carried out with this kind of substrates were characterized by a strong background signal, which could be ascribed to the SERS enhancement of citrate anions forming the stabilizing shell around the nanoparticles (see chapter 4 for details). Compared to natural sedimentation, the SERS measurements indicate that this effect is amplified by the use of the centrifuge, whose basic operation will be briefly described in the following lines.

In a non-inertial reference frame rotating at angular velocity ω, a particle of mass m placed at distance r from the axis of rotation experiences a centrifugal force given by:

$$F = m \cdot r \cdot \omega^2 = m \cdot G \tag{3.1}$$

where G is the applied centrifugal acceleration. Typically, the performance of a centrifuge is expressed with a more practical formula, i.e. as a relative centrifugal force (RCF) with respect to the gravitational force mg (g= 9.81 m/s^2) [55]:

$$RCF = \frac{mG}{mg} = \frac{G}{g} = 1.12 \cdot r \cdot \left(\frac{RPM}{1000} \right)^2 \tag{3.2}$$

where RPM is the number of revolutions per minute and r is the radius of the rotor expressed in millimetres. The RCF is a dimensionless parameter and can be interpreted as a multiple of g. Since both the applied centrifugal field and the RCF have a quadratic dependency on the angular velocity of the centrifuge, a simple way to reduce the force acting on the substrates is to decrease the number of revolutions per minute. In particular, the centrifugation process was replicated at 3500, 2000 and 500 RPM for progressively longer times (30, 40 and 50 minutes, respectively), so as to evaluate how the SERS background changes and to identify the best condition for the production of a low-background SERS substrate.

Another problem to face was the possibility of confusing one side of the substrate with the opposite one, especially during the extraction from the vial and during the conservation. The need to avoid any source of contamination prevents from labelling one side with a graphical mark, therefore it was decided to properly shape the paper pieces. In particular, chiral shapes that cannot be superimposed to their mirror images even upon rotation are the easiest approach (see figure 3.11).

Figure 3.11: Example of the one-corner truncated rectangular shape adopted for the production of the SERS substrates by centrifugation.

3.5   Characterization of the Ag SERS substrates

3.5.1   UV-VIS reflectance

Silver colloids after deposition were investigated with a UV-VIS-NIR spectrometer equipped with the integrating sphere setup (Jasco V-570). The substrates were mounted on a PTFE white board using a double-sided tape and placed in front of the sample port (figure 3.12).
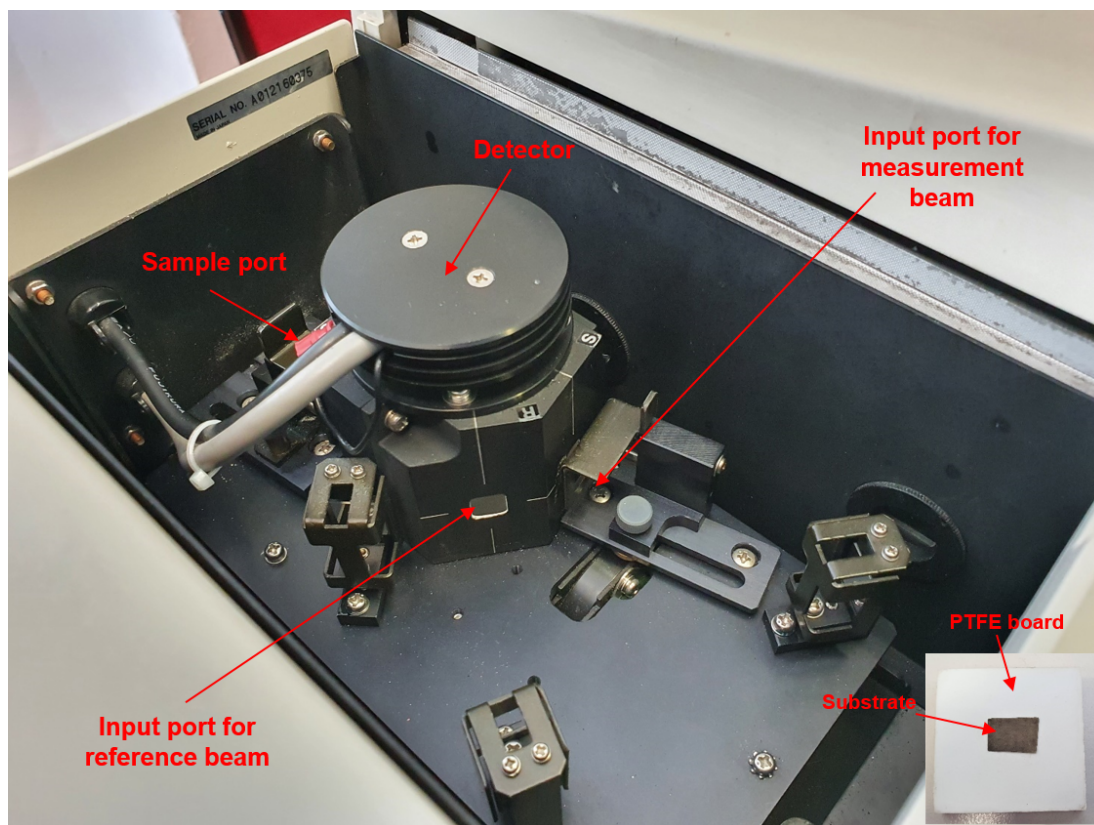
Figure 3.12: Integrating sphere setup and sample positioning (in the inset).

Reflectance spectra were collected over the wavelength range from 300 to 1500 nm, i.e. from the near-ultraviolet (NUV) to the near-infrared (NIR). In figure 3.13, the spectrum of filter paper alone (after proper cleaning with water and ethanol) is reported; as expected, reflectance approaches 98% for the majority of wavelengths in the visible, indicating that absorption by the support material is not a problem when green or red excitation lasers are used. The paper sample absorbs deep blue and UV light. The absorption onset, corresponding to a noticeable decrease of reflectance, is found around 450 nm. Moreover, the reflectance dip in the NIR ($\approx$ 1200 nm) is related to the activation of vibrational overtones of the OH groups belonging to the cellulosic material.
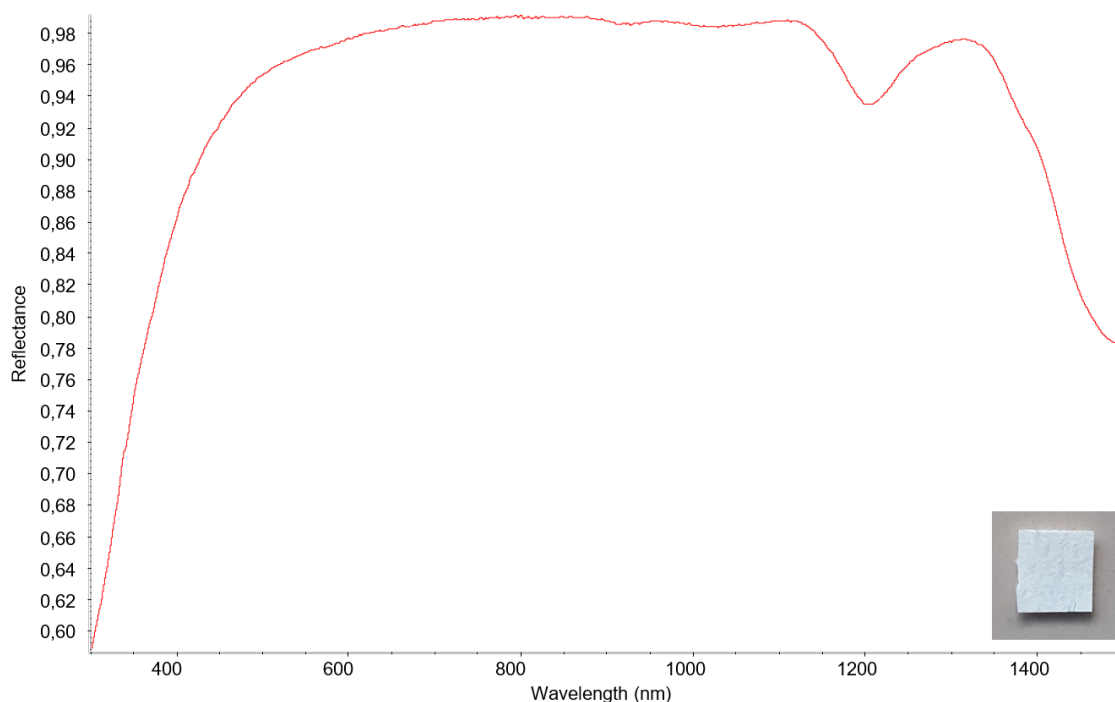
Figure 3.13: UV-VIS reflectance spectrum of filter paper (shown in the inset) after cleaning with ethanol and water.

The UV-VIS reflectance spectrum of a completely dried SERS substrate obtained by centrifugation (5000 RPM, 15 minutes) is depicted in figure 3.14. The corresponding SPR is peaked at about 384 nm, with a shoulder around 500 nm and a broad tail up to 700 nm. In particular, the shoulder indicates the presence of large aggregates or nanorods, whose longitudinal plasmon resonance is located at larger wavelengths and contributes to the broadening of the peak.

The shift of the plasmon resonance with respect to the concentrated colloid (as shown in the inset) can be ascribed to a change in the local refractive index around silver nanoparticles. Indeed, the position of the surface plasmon wavelength is linearly blue-shifted when the refractive index of the surrounding medium decreases [1]; if water (n=1.33) is replaced by air (n=1.0), the SPR peak moves towards smaller wavelengths and, at constant particle size, the estimated shift is 38 nm [56]. This value is coherent with data reported in the inset of figure 3.14.

For instance, this strong dependence of the SPR frequency on the dielectric properties of the embedding medium is exploited in the so-called plasmonic sensors. When the local refractive index around properly functionalised metallic nanostructures changes as a result of the adsorption of an analyte, the position of the plasmon resonance is shifted and any modification in the surrounding environment can be monitored [27, 56].

The step observed in the reflectance spectrum at 800 nm is caused by the grating change during the wavelength scan and it is visible because of imprecise compensation of the instrument. In addition, the substrate was quite small compared to the probed area, resulting in a weak useful signal coming from the sample.
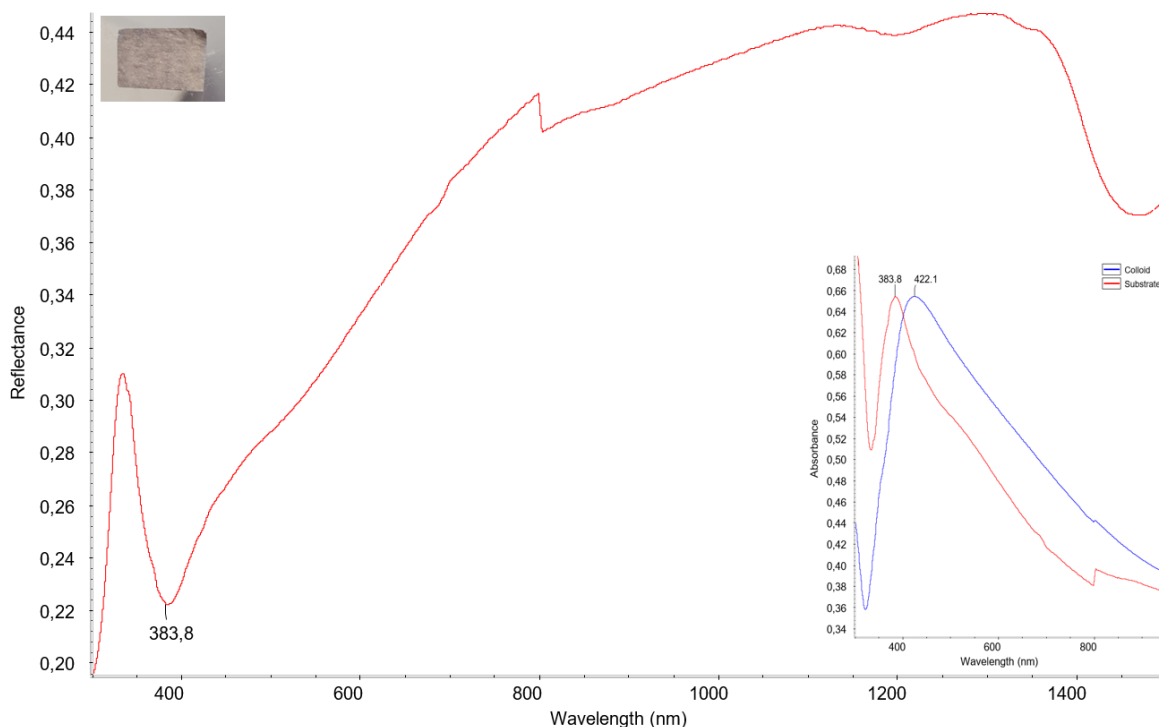
Figure 3.14: UV-VIS reflectance spectrum of a silver substrate produced by centrifugation. In the inset, the same spectrum (converted into absorbance scale by Kubelka-Munk transformation and rescaled) is compared to the one of the concentrated silver colloid. The sudden step at 800 nm is due to imprecise compensation of the instrument when the grating is changed across different wavelength ranges.

3.5.2 Morphological investigation by SEM

Scanning Electron Microscopy (SEM) was employed to investigate the morphology of one of the substrates produced by centrifugation at 5000 RPM for 15 minutes. All the images were acquired in the *NanoLab* (Energy Dept., PoliMi) by the *Zeiss* Supra 40 Field-Emission Scanning Electron Microscope (FE-SEM), operating in high-vacuum and equipped with the GEMINI column.

As shown in figure 3.15 and in panels (a)-(b) of figure 3.16, silver nanoparticles tend to accumulate in cavities and depressions on the fibre surface and in the interstices among fibres. This process is probably induced during the substrate drying and can be viewed as a *coffee ring* effect at the microscopic scale. It is important to note that the non-

conducting nature of paper, along with the non-uniform distribution of nanoparticles on fibres, leads to local charge build-up on the sample surface and is responsible for the presence of glowing and very bright regions, and for geometry distortions in the image [57].
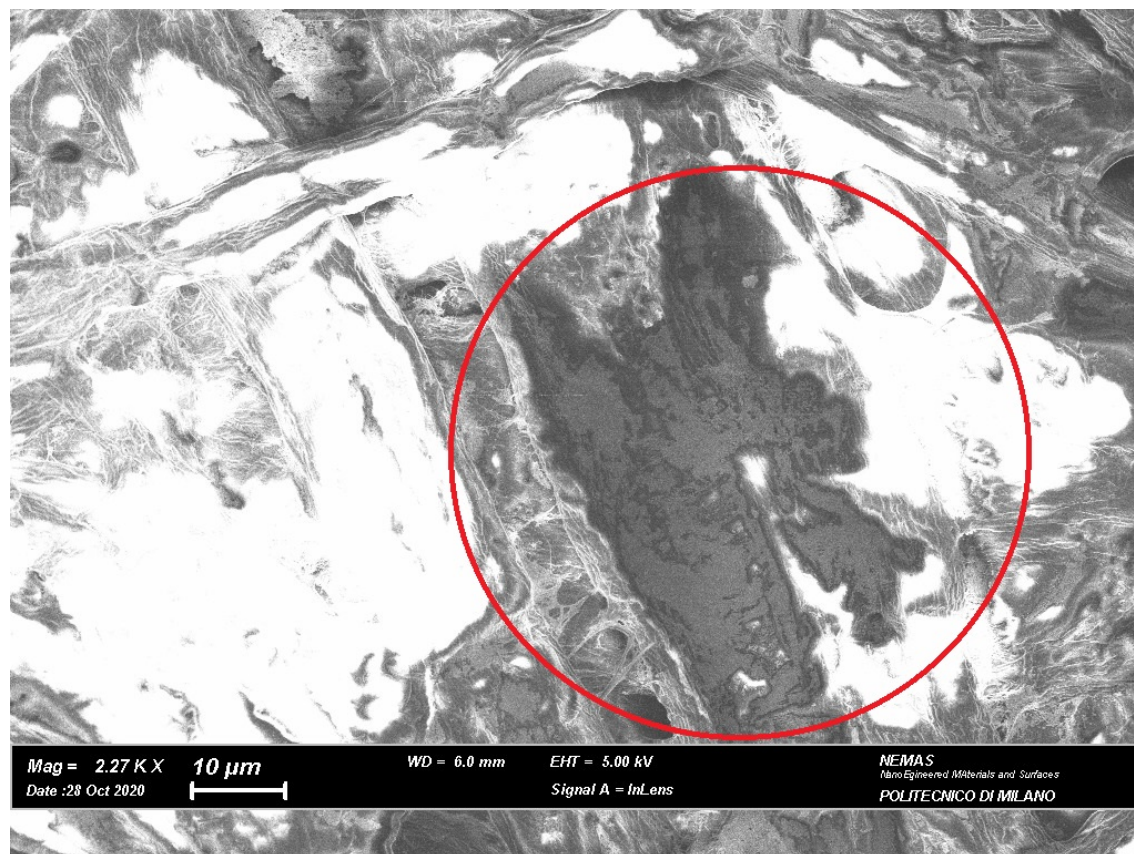
Figure 3.15: SEM image of SERS substrate produced by centrifugation (EHT = 5 kV, WD = 6.0 mm, 2270×). Nanoparticles aggregation is highlighted by the red circle.

Considering panels (c) and (d) of figure 3.16, both uniform expanses of particles and large, disordered aggregates can be observed, indicating a poor spatial uniformity of the final substrate.

A close-up of one of the nanoparticles expanses is reported in figure 3.17, in which not only spherical and elliptical nanoparticles but also nanorods with different aspect ratios can be noted. Interestingly, the longest and thinnest rods have a tendency to self-assemble in clusters of parallel nanorods. The presence of rods is in agreement with the broad shape of the UV-VIS spectrum of the concentrated colloid and is expected to be beneficial to the SERS applications of the substrate.
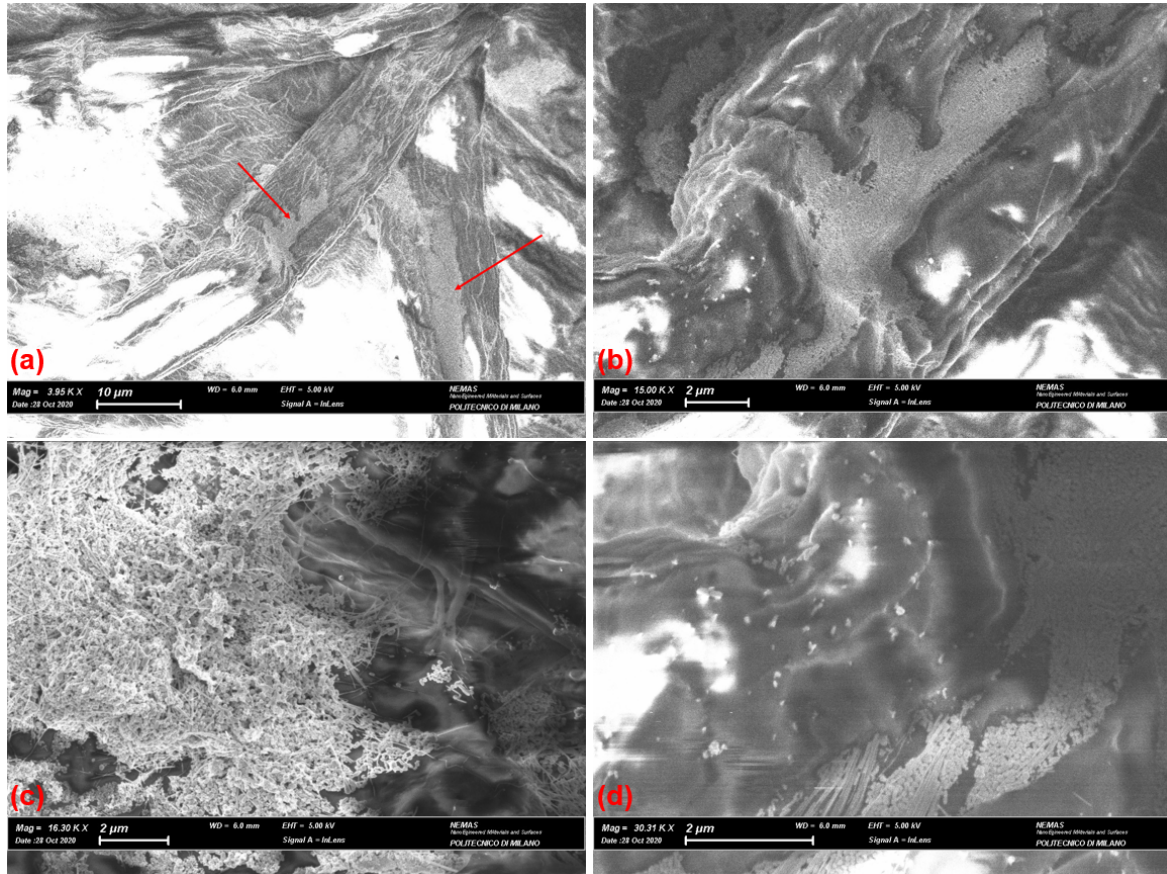
Figure 3.16: SEM images of SERS substrate produced by centrifugation, highlighting different details and with increasing magnification (EHT = 5 kV, WD = 6.0 mm).

Using the processing software *ImageJ* [58], the size of nanoparticles and nanorods was estimated. The average diameter of the spherical particles is 70 nm (max: 158 nm; min: 35 nm), whereas the average length and width of rods are, respectively, 232 nm (max: 890 nm; min: 125 nm) and 50 nm (max: 90 nm, min: 22 nm), with the aspect ratio ranging from 2 to 28. Apparently, the average size of particles is not consistent with the one predicted looking at the position of the absorbance peak in the UV-VIS spectrum of the concentrated colloid, i.e. about 50 nm [59] (see figure 3.2 for comparison). This discrepancy can be explained considering that small nanoparticles are less clearly discriminated using *ImageJ* and remembering that the production process via centrifugation is more effective in depositing heavier and larger particles. In both cases, smaller particles are not accounted for and the average deviates towards higher values. Moreover, particle aggregation effects are certainly non-negligible on the paper substrate and affect the overall plasmonic response.
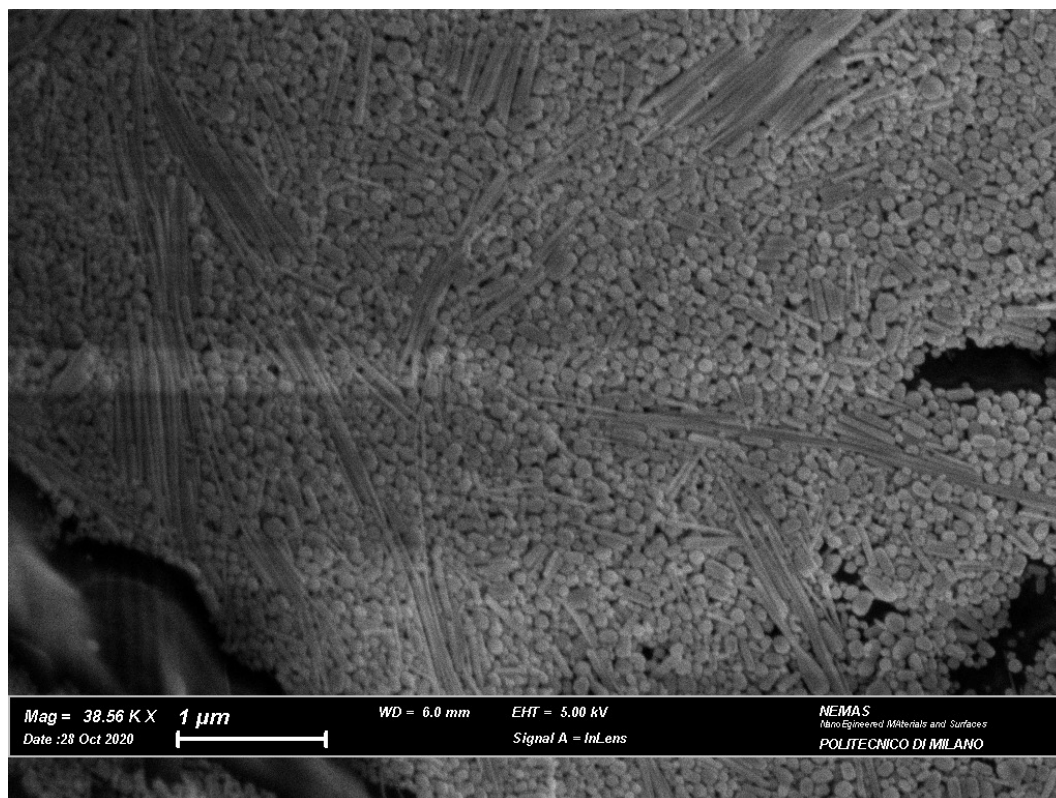
Figure 3.17: SEM close-up of one of the Ag nanoparticles and nanorods expanses observed in the SERS substrate produced by centrifugation (EHT = 5 kV, WD = 6.0 mm, 38560×).

Finally, in figure 3.18 a SEM image acquired on my substrate is compared with a micrograph reported in the supplementary material of reference [15], which represents filter paper fibres coated with silver during one-week incubation in 10× concentrated colloid and in the absence of an external aggregating agent. In spite of slightly different magnification, the non-uniform contrast suggests that the silver layer is not perfectly homogeneous in both cases.
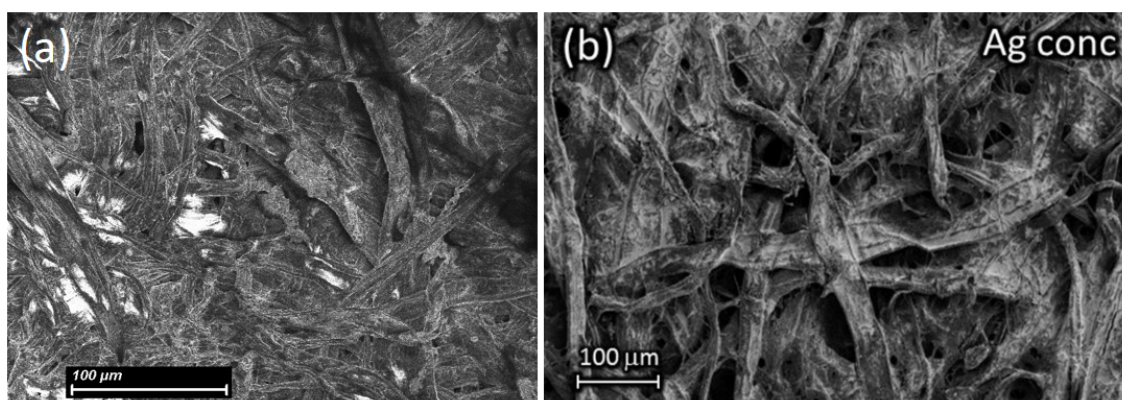
Figure 3.18: Comparison between the SEM image of my substrate produced by centrifugation ((a); EHT = 5 kV, WD = 6.0 mm, 619×) and the SEM image reported in [15] for a substrate produced via natural sedimentation during one-week incubation in 10× concentrated silver colloid (b).

Chapter 4

Optimization of the Ag SERS Substrates

An ideal high-performance SERS substrate for practical use in TDM and other very demanding practices should display some qualities such as high average enhancement, spatial uniformity, good reproducibility, chemical stability and ease of fabrication in addition to high sensitivity. Typically, a real substrate is a compromise and one feature can be optimized with respect to the others depending on the final application [3]. In this chapter, the substrates prepared as described in chapter 3 will be extensively tested to identify the best treatment and preparation process for optimized SERS sensing of the analytes of interest.

4.1   Raman instrumentation and setup

All the tests and the SERS measurements presented in this thesis work were performed using the dispersive Raman instrument Horiba Jobin Yvon LabRAM HR8000 (figure 4.1), equipped with an Olympus BX41 microscope and with several laser sources. In particular, two laser radiations were used, i.e. a 532 nm green laser from a frequency-doubled Nd:YAG source (with a maximum nominal power of 300 mW) and a 632.8 nm red laser from a He:Ne source (with an average nominal power of 50 mW). The incident power on the sample can be tuned using a series of filters with decreasing optical densities, able to reduce the nominal power by a half, a quarter, 10, 100, 1000 and 10000 times. After the interaction with the sample, the backscattered radiation passes through an edge (or notch) filter that eliminates the elastic Rayleigh component and travels towards a grating, whose specific configuration (600 or 1800 lines/mm) is selected according to the laser wavelength. After being dispersed by the grating, the light is steered to a Peltier-cooled CCD detector, where the Raman photons are

detected. Finally, the signal is processed by the computer software *LabSpec* and a Raman spectrum is delivered, depicting the intensity (in instrumental units, e.g. detector counts) as a function of the Raman shift (in cm⁻¹).

Figure 4.1: The Horiba Jobin Yvon LabRAM HR8000 used to acquire spectral data (taken from [8]).

4.1.1 The spinning cell

One of the main drawbacks of chemically-synthesized SERS substrates is the absence of spatial uniformity, which implies high sensing variations across different points of the same substrate. The measured intensity may deviate significantly from point to point and reliable quantitative measurements may become unfeasible. This problem could be further amplified when paper-based SERS sensors are considered: the paper support itself has not a homogeneous texture (as shown in figure 3.4) and the three-dimensional structure of fibres can foster the accumulation of nanoparticles in localized regions of the substrate. In previous thesis works [8] and [7], a practical procedure was introduced to obtain spatially-averaged SERS spectra on non-uniform substrates in short times and with easy implementation. In particular, a rotating Hard Disk Drive (HDD) was used to spin the substrates, while the objective and the laser beam were kept fixed during the entire experiment. In my thesis work, the so-called *single-centred drop spinning cell* (SCDSC) approach was selected, consisting of placing one substrate at the centre of the rotating device (figure 4.2).

After careful cleaning of the moving part with propanol to avoid contamination issues, the substrate is mounted on the cell using a double-sided tape. The rotation angular frequency of the device is fixed and equal to 7200 RPM (754 rad/s) and the laser beam is off-centred with respect to the rotation axis. As a result, the laser-sample interaction during the mechanical rotation of the substrate occurs along a circular path and the

Raman signal is collected from different points, leading to a net spectrum which is a spatial average of all the points probed during the measurement along the path. The more the laser spot is eccentric with respect to the axis of rotation, the more efficient this approach will be compared to the static mode in terms of exposure time on each spot along the circular path and of number of spots that are averaged out.
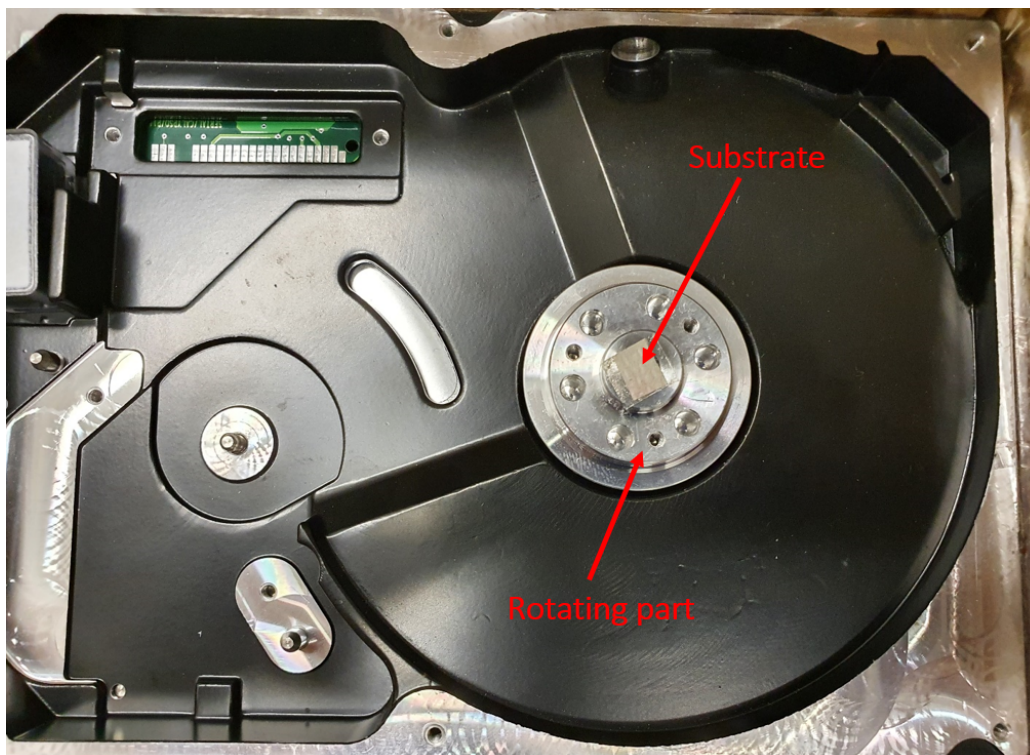
Figure 4.2: The spinning-cell setup.

An important improvement related to the spinning-cell setup is the reduced residence time of the laser in any point, which allows the increase of the laser intensity on the sample even by orders of magnitude with no risk of photo-induced damage. A simple model can be introduced to justify the previous consideration [7, 8]. The minimum theoretical diameter d of a laser spot at focus is affected by the laser wavelength and by the magnification of the objective and can be calculated using the approximated formula for the Airy disk diameter [60]:

$$d = 1.22 \frac{\lambda}{NA} \tag{4.1}$$

where λ is the wavelength and NA is the numerical aperture of the objective and depends on the magnification and on the surrounding medium. Typically, the actual laser spot size is larger than the value estimated from equation 4.1 because of many deviations from ideality in the real optical components (e.g., finite laser bandwidth, imperfect alignment and focus, penetration of the laser in the sample) [60].

In a static measurement, the energy delivered to the sample per unit area is given by:

$$E_{st} = \frac{P}{A} \cdot T_m \tag{4.2}$$

where P is the incident laser power, A is the area of the laser spot at focus and T_m is the duration of the measurement. On the other hand, in dynamic mode the energy is distributed over an annulus whose average radius coincides with the distance between the laser and the rotation axis and whose thickness is equal to the laser spot diameter. Thanks to the high rotational speed of the device, the residence time of the laser on a single circular spot of diameter d is much smaller and, consequently, the energy deposited per unit area is decreased. Considering an annulus of average radius r and thickness d (figure 4.3), the residence time on a single spot can be calculated if the angular frequency of rotation ω is known:

$$\tau = \frac{d}{\omega \cdot r} \tag{4.3}$$

To conclude, the total energy delivered per unit area during a dynamic experiment is given by:

$$E_{dy} = \frac{P}{A} \cdot N \cdot \tau \tag{4.4}$$

where N is the number of revolutions of the device:

$$N = \frac{\omega \cdot T_m}{2\pi} \tag{4.5}$$

Using the parameters reported in table 4.1, a numerical assessment of equations 4.1 - 4.5 can be provided.

λ	632.8 nm
NA	0.45 (20×)
d	1716 nm
P	5 mW
A	2.31 μm^2
T_m	100 s
r	2 mm
ω	754 rad/s
N	12000

Table 4.1: Typical parameters during my SERS measurements.

It results that the residence time τ is 1.14 μs and the energy delivered per unit area during a dynamic measurement is around 3×10^7 J/m^2. This value can be compared with the energy per unit area deposited during a static measurement in the same experimental conditions, i.e. 2.2×10^{11} J/m^2, which is four orders of magnitude larger.

Figure 4.3: The substrate is mounted at the centre of the rotating device and the laser is kept fixed at distance r from the rotation axis. During the SERS measurement, the laser track on the substrate describes an annular surface (in red).

4.1.2 Test molecules

Two molecular species were used to test and optimize the SERS substrates, i.e. Perampanel (whose chemical and vibrational properties have been extensively described in chapter 2) and Rhodamine 6G, whose structural formula is depicted in figure 4.4. Rhodamine 6G (RH6G) is an organic dye and, thanks to its high Raman and fluorescence yield, is commonly used as an effective SERS probe [61].
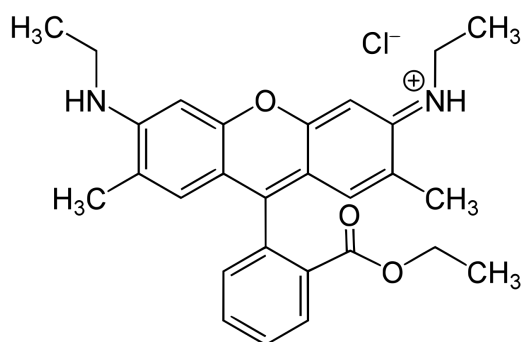
Figure 4.4: Molecular structure of Rhodamine 6G (RH6G). Image taken from [62].

A typical UV-VIS spectrum of RH6G in neutral conditions is reported in figure 4.5. The main absorption peak at 528 nm is highlighted.
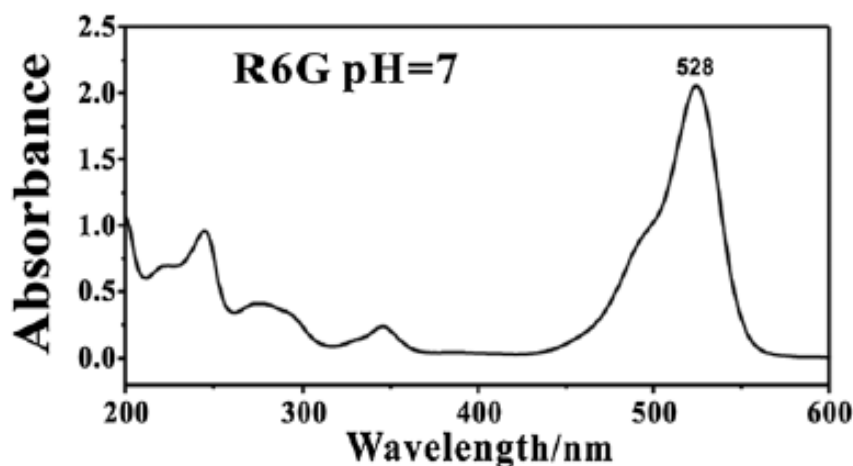
Figure 4.5: UV-VIS spectrum of RH6G in neutral conditions (adapted from [61]).

In table 4.3, the main Raman peaks of RH6G are listed, along with their vibrational assignment [63].

Wavenumber (cm⁻¹)	Mode
612	C-C ring in-plane bending in xanthene/phenyl rings
772	C-H out-of-plane bending
797	hybrid mode (xanthene/phenyl rings and NHC_2H_5 group)
1127	C-H in-plane bending in xanthene/phenyl rings
1187	C-H in-plane bending in xanthene ring
1204	hybrid mode (xanthene/phenyl rings)
1275	C-O-C stretching in $COOC_2H_5$ group on phenyl ring
1312	hybrid mode (xanthene/phenyl rings and NHC_2H_5 group)
1363	C-C stretching in xanthene ring
1449	C-N stretching in NHC_2H_5
1509	C-C stretching in xanthene ring
1575	C-C stretching in phenyl ring
1595	hybrid mode (phenyl ring with $COOC_2H_5$)
1651	C-C stretching in xanthene ring

Table 4.2: Assignment of RH6G vibrational modes (after [63]).

4.1.3 Preparation of solutions

A stock aqueous solution of RH6G 10^{-4} M was properly diluted to obtain 3 mL solutions with molar concentrations of 10^{-5}, 10^{-6} and 10^{-7} M.

As for Perampanel, a stock solution of 10^{-3} M PER in methanol (stored in a refrigerator at 2 °C) was used to produce acidified PER solutions with molar concentrations of 10^{-4}, 10^{-5} and 10^{-6} M. The UV-VIS absorption spectrum of the diluted stock solution of PER is reported in figure 4.6, where the expected characteristic peaks at 288 nm and 335 nm are highlighted. Furthermore, 3 mL of an acidic solution at pH 0 were prepared by mixing 25 μL of HCl 37% (CAS: 7647-01-0, *Sigma-Aldrich*) with 150 μL of H_2SO_4 96% (CAS: 7664-93-9, *Carlo Erba*) and with 2.825 mL of distilled water. Then, 50 μL of the solution at pH 0 were diluted with 4.95 mL of distilled water to obtain 5 mL of an acidic aqueous solution at pH 2, with a molar ratio HCl:H_2SO_4 of 1:9. All the pH values were checked with a universal halochromic pH indicator ($DF^{®}$). The final step to prepare 1 mL of PER solution at the desired concentration is summarized in table 4.3, which shows the mixed volumes of PER 10^{-3} M in methanol and pH 2 water solution (HCl:H_2SO_4, 1:9).

PER (M)	PER 10^{-3} M in methanol (μL)	pH 2 solution (mL)
10^{-4}	100	0.9
10^{-5}	10	0.99
10^{-6}	1	0.999

Table 4.3: Volumes of a 10^{-3} M PER solution in methanol and of a pH 2 aqueous solution to be mixed to obtain the desired acidified PER solutions.
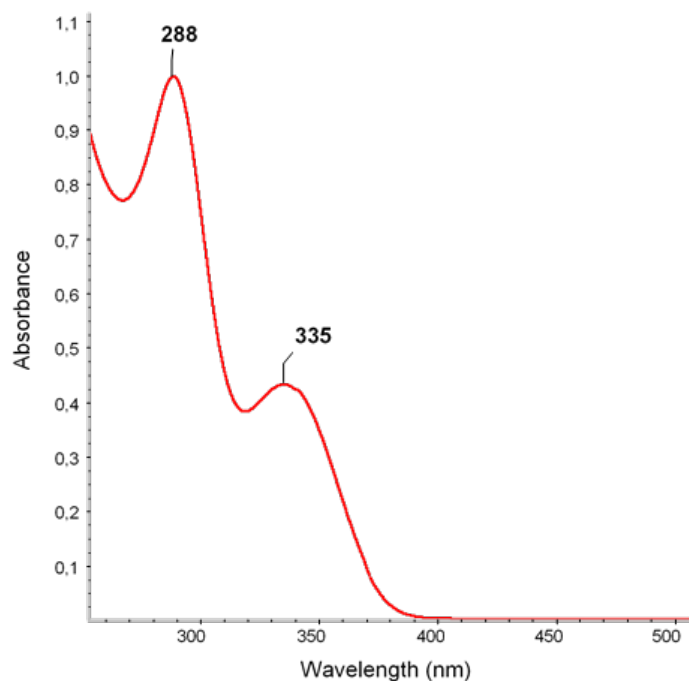
Figure 4.6: UV-VIS absorption spectrum of the PER stock solution in methanol diluted with distilled water to 10^{-4} M. The absorbance is normalized to the tallest peak.

4.2 Testing the Ag-based SERS substrates produced by natural sedimentation

All the substrates were tested using 10 μL droplets of a 10^{-7} M RH6G solution. The SERS spectra were collected on completely dried substrates using the 632.8 nm excitation laser, with a 20$\times$ objective and different incident powers (10 s of acquisition time, 5 averages). Both static and dynamic measurements were performed. Before casting the solution, the spectrum of the substrate background alone was recorded under the same experimental conditions.
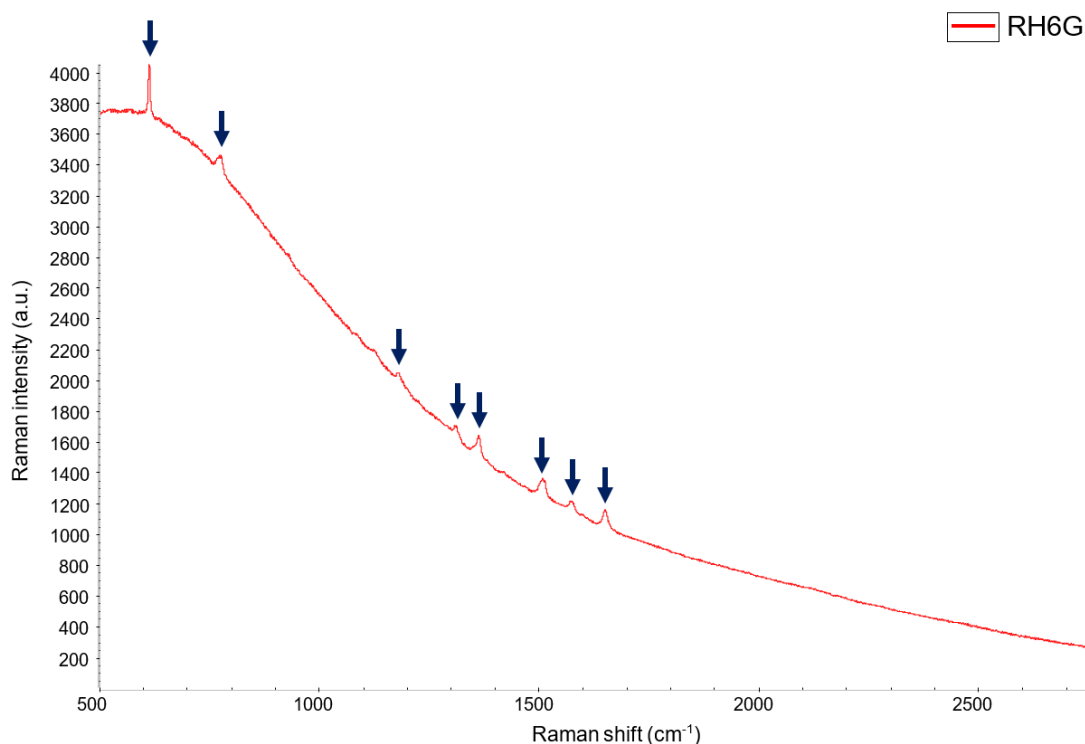
Figure 4.7: SERS spectrum of RH6G 10^{-7} M above intense fluorescence background. 532 nm excitation, 20$\times$ objective, 0.03 mW power, 10 s exposure time (5 averages), static measurement.

In a first attempt, the SERS measurements were carried out using the 532 nm excitation laser. However, as clearly shown in figure 4.5, this laser wavelength is extremely close to the resonance condition, being the main absorption band of RH6G centred around 528 nm. As a result, a strong fluorescence emission coming from Rhodamine molecules that were not adsorbed onto silver nanoparticles completely overwhelmed the Raman signal, leading to saturation of the detector. Only if the incident power was dramatically decreased down to 0.03 mW, some of the characteristic Raman peaks of RH6G started becoming visible above the intense fluorescence background, as seen in figure 4.7. A significant improvement was obtained by changing the excitation wavelength to 632.8

nm: the laser was far from electronic absorption and most of the Raman peaks of Rhodamine could be identified and resolved with a good signal-to-noise ratio, even at high incident power (5 and 0.5 mW), as show in figure 4.8.
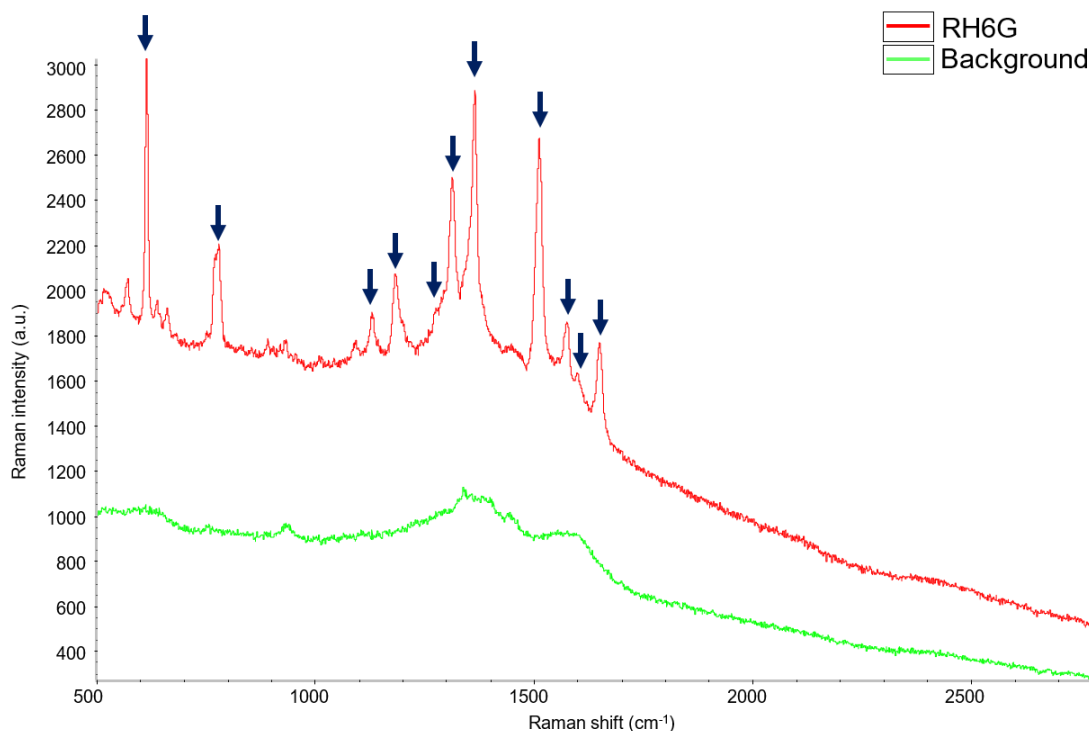
Figure 4.8: SERS spectrum of RH6G 10^{-7} M. 632.8 nm excitation, 20× objective, 0.5 mW power, 10 s exposure time (5 averages), dynamic measurement. The background of the SERS substrate corresponds to the green spectrum.

4.3 Testing the Ag-based SERS substrates produced by centrifugation

4.3.1 The background issue

Centrifugation allows a significant reduction of the substrate production times, avoiding the long incubation period required to have natural sedimentation of nanoparticles by gravity. However, a substantial problem related to this kind of substrates is the strong and structured background signal that seriously inhibits the detection of any signal coming from the analytes. Figure 4.9 compares the background signal of three different substrates obtained by centrifugation at 5000 RPM for 20 minutes and that of a substrate produced by natural sedimentation. The background is non-zero in all the cases, but the difference between the two production methods is clearly visible:

centrifugation induces in all the substrates an intense background characterized by several and well-defined peaks.
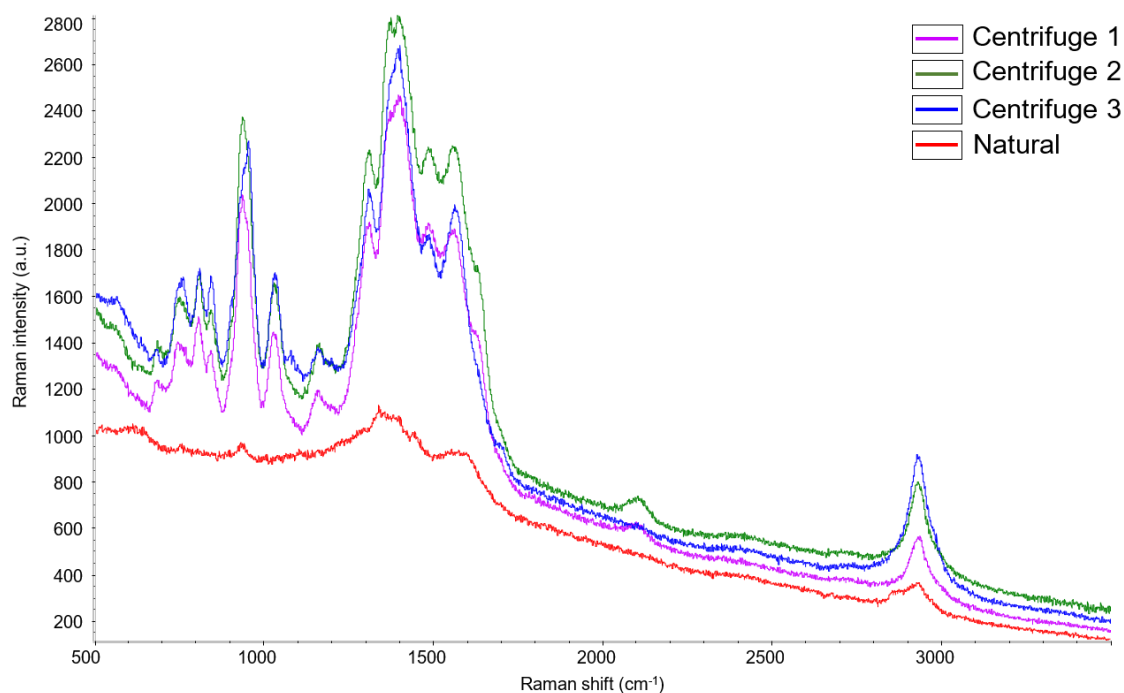
Figure 4.9: SERS signal coming from four different substrates, three of which produced by centrifugation and one by natural sedimentation. 632.8 nm excitation, 20× objective, 0.5 mW power, 10 s exposure time (5 averages), dynamic measurement.

First of all, the paper support and the silver colloid were separately analysed to eliminate any doubt about contamination. The Raman spectra of the paper before and after cleaning with ethanol were collected, but the background was weak and substantially flat in both cases (spectra not shown). As for the colloid, some 4 μL droplets were deposited onto an aluminium support coated by DLC and, after drying, the SERS spectrum was recorded using 632.8 nm laser (0.5 mW incident power and 50× objective). The background signal of the bare colloid was relatively intense and with certain peaks, but all the structured features seen in figure 4.9 were absent. Moreover, the SERS spectrum of the concentrated silver colloid resembles the background spectrum of the substrate produced via natural sedimentation, as reported in figure 4.10. The intense and sharp peak at 1054 cm^{-1} can be assigned to nitrate anions [64].
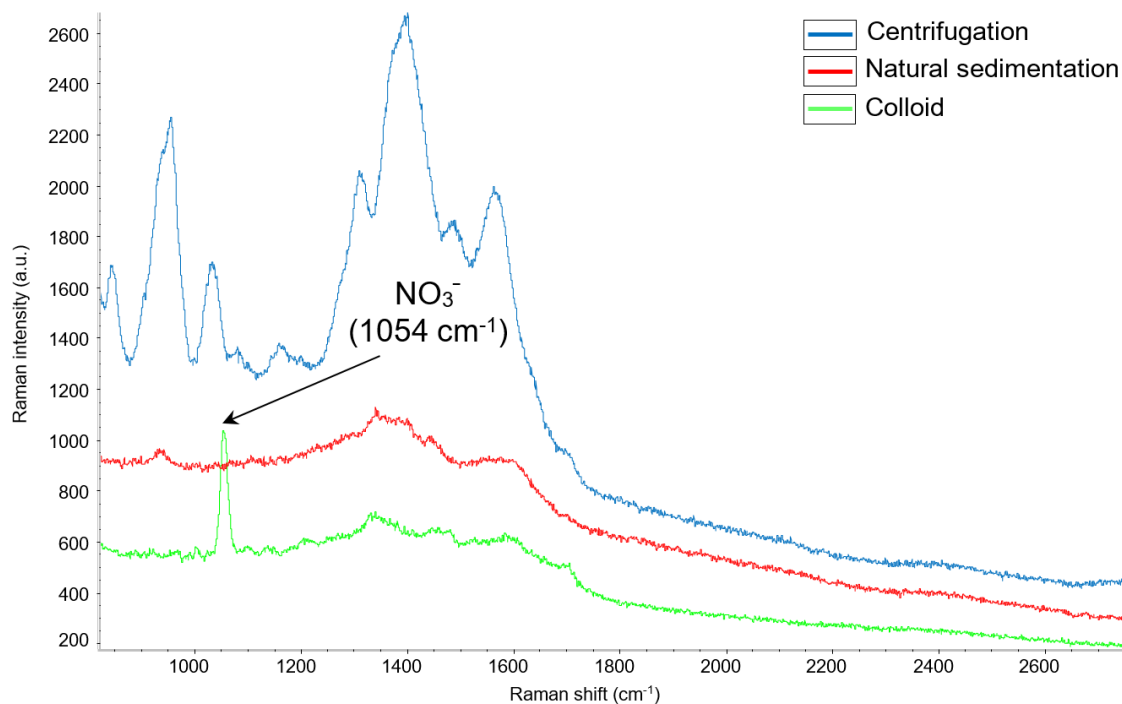
Figure 4.10: SERS signal of the bare colloid (in green) compared to the background signal coming from two substrates produced via centrifugation and natural sedimentation. 632.8 nm excitation, $20\times$ objective, 0.5 mW power, 10 s exposure time (5 averages).

Therefore, the structured background observed in figure 4.10 for the SERS substrate obtained by centrifugation is caused by neither the paper nor the colloid. One possible explanation may ascribe the background to the SERS enhancement of the cellulose material of the paper, because of the onset of interactions between the fibres and the nanoparticles during the centrifugation process at high speed. However, the peaks between 800 and 1600 cm^{-1} observed in figure 4.9 are not consistent with the spectral markers of cellulose found in the literature [65]. In addition, cellulose is reported to have a weak SERS response and to produce minimal interference and background signals during measurement [14].

The previous considerations, along with a comparison with spectral data reported in the literature [66], suggested that the observed signal could be originated from unreacted citrate molecules adsorbed onto silver nanoparticles and forming the stabilizing shell. Although some citrate peaks are visible also in the case of natural sedimentation, the centrifugation process enhances the citrate background in a RPM-dependent way (figure 4.11). However, the use of low revolutions per minute implies longer centrifugation times and incomplete precipitation of silver nanoparticles, without resulting in a significant flattening of the background. Consequently, the next substrates were produced by centrifugation at 5000 RPM for 15 minutes in order to accelerate the

production process and to exploit as much silver as possible.
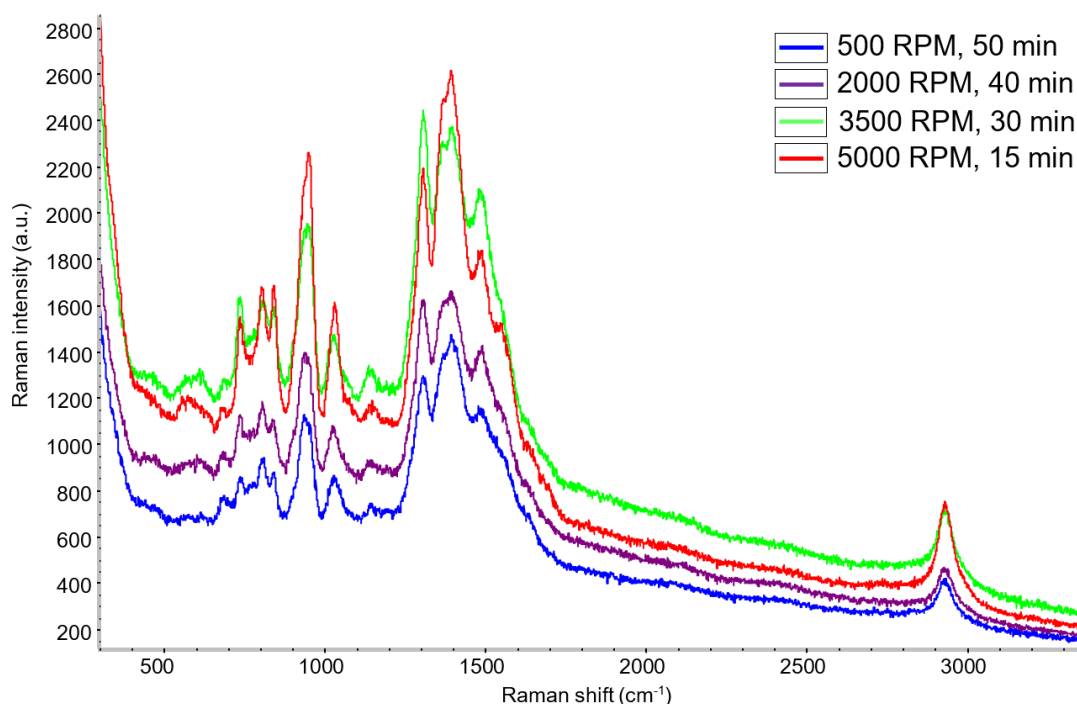
Figure 4.11: Influence of the centrifuge angular velocity on the background signal. 632.8 nm excitation, 20× objective, 0.5 mW power, 10 s exposure time (5 averages).

The background shown in the previous figures is so intense that the detection of SERS signals of other molecules, even of those with the highest response, may become very hard. For example, as-prepared substrates were tested with 10^{-6} and 10^{-7} M RH6G solutions but all the characteristic markers of this molecule were weak or absent. However, the first tests with acidified PER solutions were satisfactory and most of the characteristic peaks of Perampanel were evident and clearly distinguishable from the background. Moreover, the background itself was not as structured and intense as before, suggesting that the acidic environment or the presence of chlorides had induced chemical modifications in the SERS substrate.

Therefore, bare substrates were separately treated with hydrochloric acid (pH=3), sulphuric acid (pH=3), and sodium chloride (10^{-3} M) and the background spectra were compared. As seen in figure 4.12, the intensity is reduced with all the treatments, but the use of sulphuric acid is almost ineffective in eliminating the structured features of the background. On the other hand, the treatment with hydrochloric acid and sodium chloride provides a strong reduction of the background and, especially in the case of HCl, induces a significant flattening of the spectrum. Notably, with both HCl and NaCl, the peaks around 807 and 2900 cm^{-1} are intensified and a new peak at 1440 cm^{-1} appears.
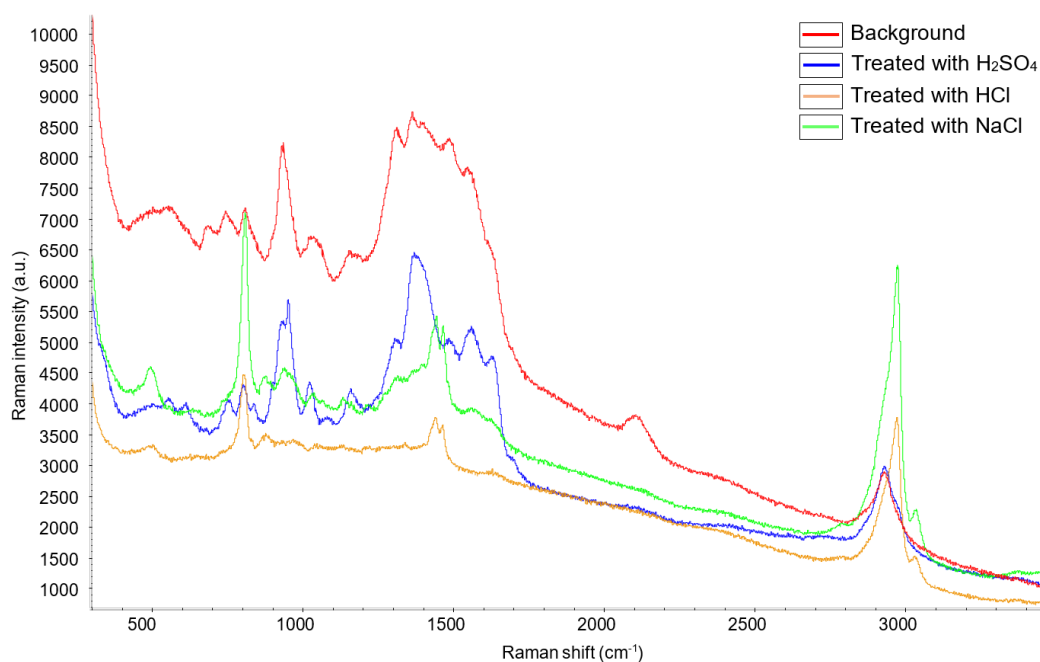
Figure 4.12: Modification of the background spectrum according to different chemical treatments. 632.8 nm excitation, 20× objective, 5 mW power, 10 s exposure time (5 averages).

Taking everything into account, the previous modifications could be ascribed to chlorides rather than to the acidity, in particular to the so-called *chloride activation* effect [1]. Chlorides and other halide ions have a strong affinity with silver and are able to detach and replace the anchoring group of the stabilizer, triggering the spontaneous aggregation and coalescence of nanoparticles [67, 68]. According to [69], the chemical interaction between silver nanoparticles and citrate has an ionic nature and occurs through the two oxygen atoms of the carboxylate unit. In particular, the low-frequency band at 227 cm^{-1} observed in the untreated substrates can be assigned to the symmetric stretching of Ag-OCO$^-$ (figure 4.13). When chlorides are present in a fairly high concentration, carboxylate groups are displaced and Cl$^-$ ions attach to the silver surface. This process can be confirmed looking at the spectrum reported in figure 4.13: the main peak becomes more intense and shifts from 227 to 244 cm^{-1}, indicating that Ag-OCO$^-$ interactions have been replaced by Ag-Cl bonds [67, 68]. Conversely, as reported in [70], SO$_4^{2-}$ ions have a weak affinity for silver and cannot displace the tightly bound citrate molecules from the nanoparticles as Cl$^-$ ions do.

As a result, a proper treatment with a chloride-containing solution is a practical and simple way to improve the detection capability of the substrates and to reduce the strong contribution from the background, provided that chlorides do not negatively affect the adsorption properties or the chemical stability of the analyte. In figure 4.14, the SERS spectra of a 10^{-6} M solution of RH6G are reported and chloride activation

is evident. On the untreated substrate, the background signal is so intense that the characteristic bands of Rhodamine cannot be identified; on the other hand, all the main spectral features are clearly visible after treating the substrate with one droplet (10 μL) of hydrochloric acid (pH=3) or NaCl solution with the same chloride content.
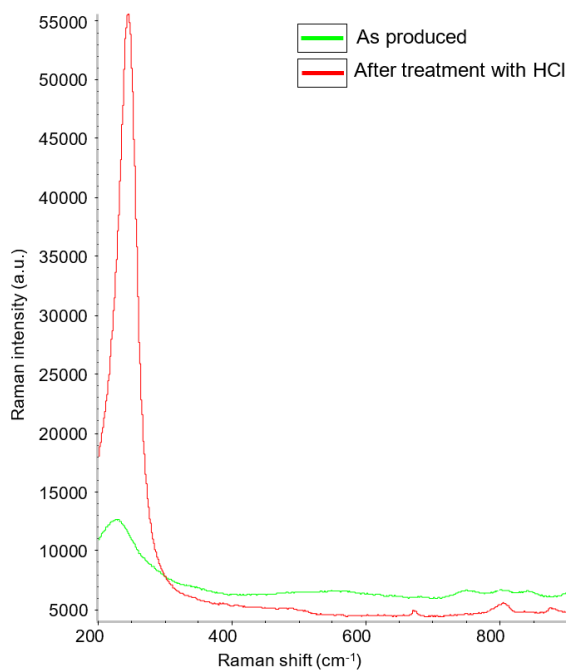
Figure 4.13: Comparison of the low-frequency peak before and after the treatment with chlorides.
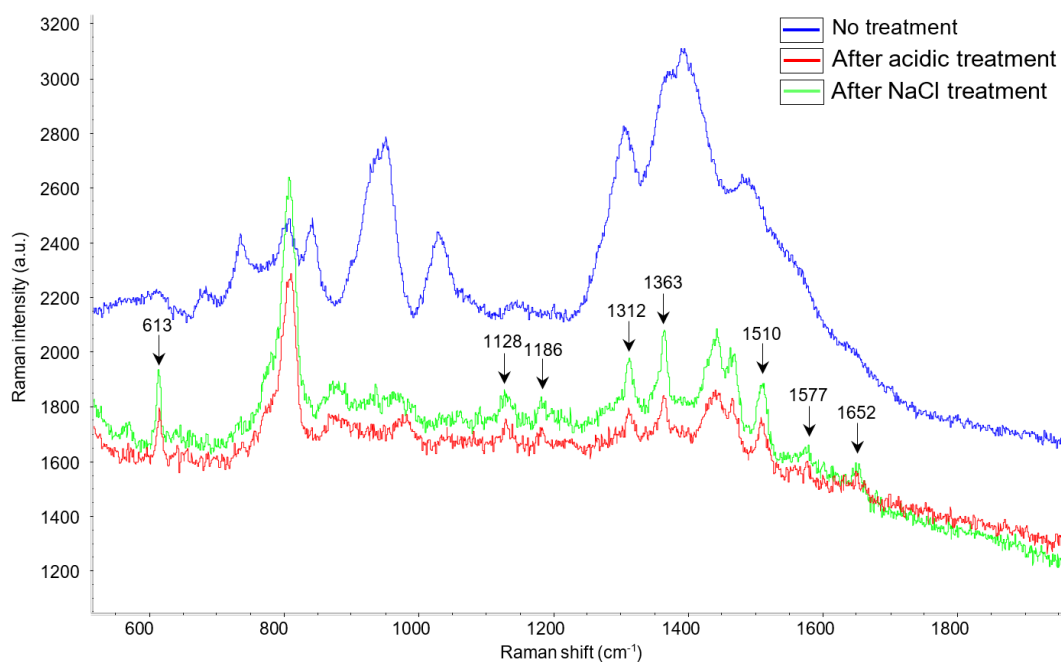
Figure 4.14: SERS spectra of RH6G 10^{-6} M on untreated or treated substrate. 632.8 nm excitation, 20× objective, 0.5 mW power, 10 s exposure time (5 averages), dynamic measurement.

4.3.2   SERS detection of Perampanel

A chloride pre-treatment is not necessary when PER solutions are considered; as discussed in the literature [6, 8], Perampanel requires protonation to be detected and chlorides are already present in the acidified solution. SERS substrates produced via centrifugation at 5000 RPM for 15 minutes were tested using 10 μL droplets of PER solutions at different concentration. The spectra were acquired in dynamic mode using the 632.8 nm laser, focused with a 20× objective on the dried substrate and with an incident power of 5 mW (10 s acquisition time, 5 averages).

The best SERS spectra of Perampanel in acidified environment are shown in figures 4.15 and 4.16, corresponding to concentrations of 10^{-4} and 10^{-5} M. All the characteristic PER bands at 670, 877, 1001, 1019, 1595 and 2230 cm^{-1} are well-resolved, intense and clearly distinguishable from the spectral features of the background. Moreover, additional weak peaks at 1225 and 1447 cm^{-1}, assigned to the in-plane C-H bending coupled with ring deformation, are visible in the spectrum of the most concentrated solution. As expected, the background signal is reduced and flattened by chlorides and does not hinder the SERS detection of Perampanel. Finally, the SERS spectrum of a 10^{-6} M acidified PER solution is reported in figure 4.17: although some weak peaks could be identified around 877, 1001 and 1595 cm^{-1}, the signal-to-noise ratio is too bad to reliably assess the detection of Perampanel.
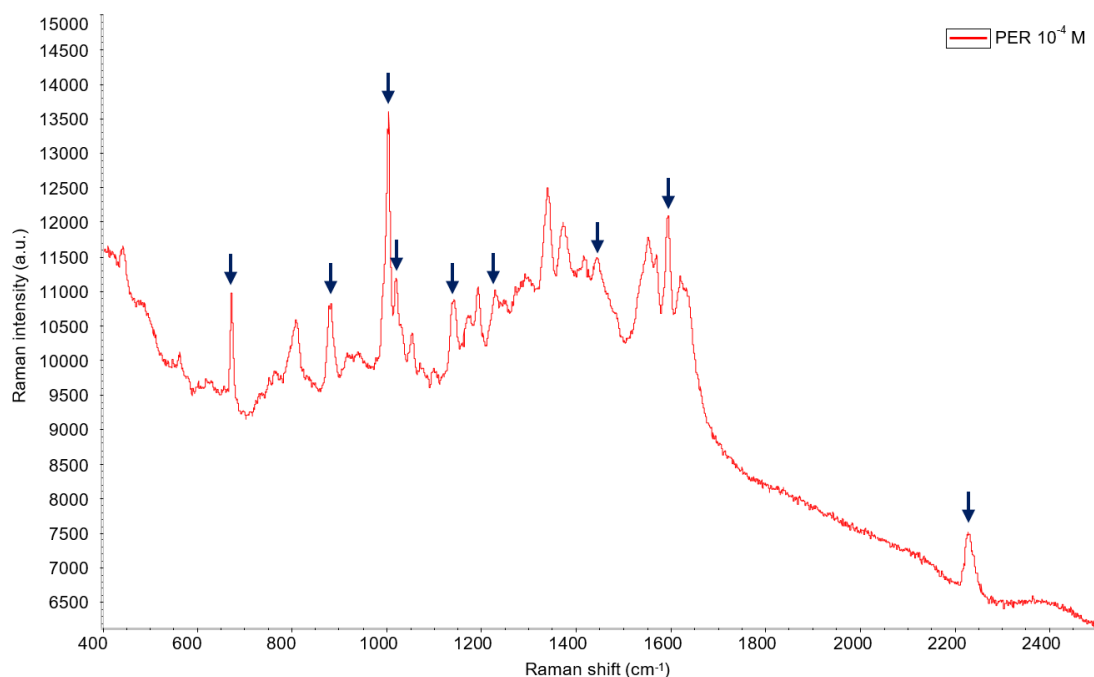
Figure 4.15: SERS spectrum of acidified PER 10^{-4} M. 632.8 nm excitation, 20× objective, 5 mW power, 10 s exposure time (5 averages), dynamic measurement.
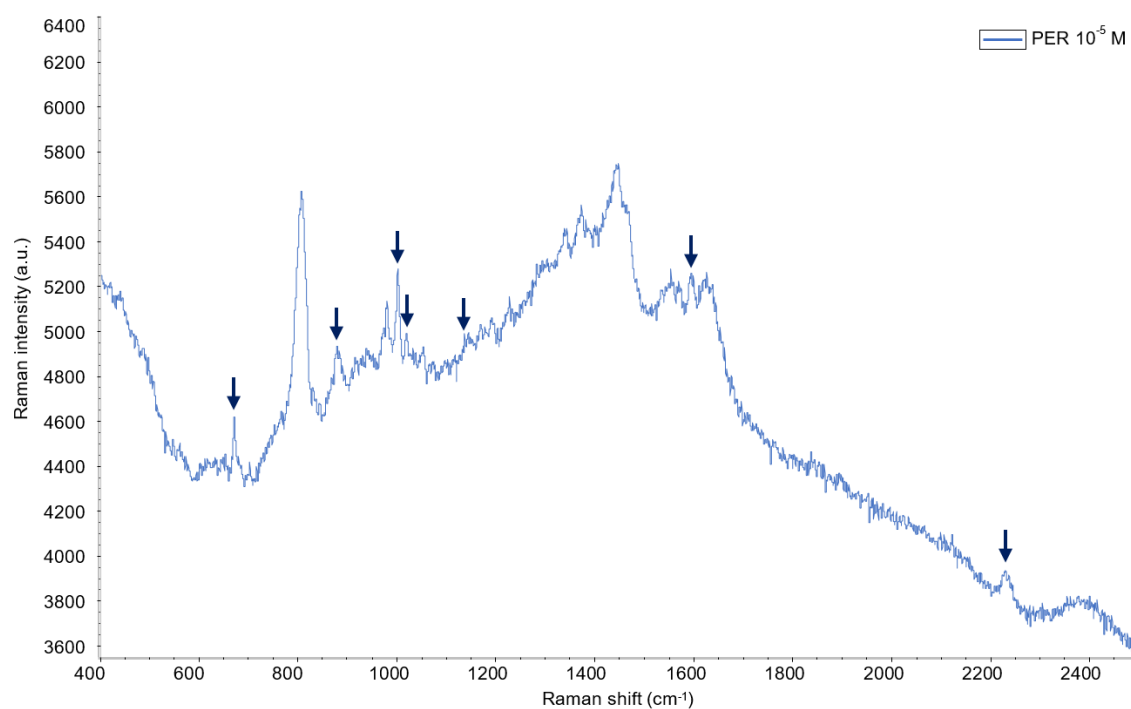
Figure 4.16: SERS spectrum of acidified PER 10^{-5} M. 632.8 nm excitation, $20\times$ objective, 5 mW power, 10 s exposure time (5 averages), dynamic measurement.
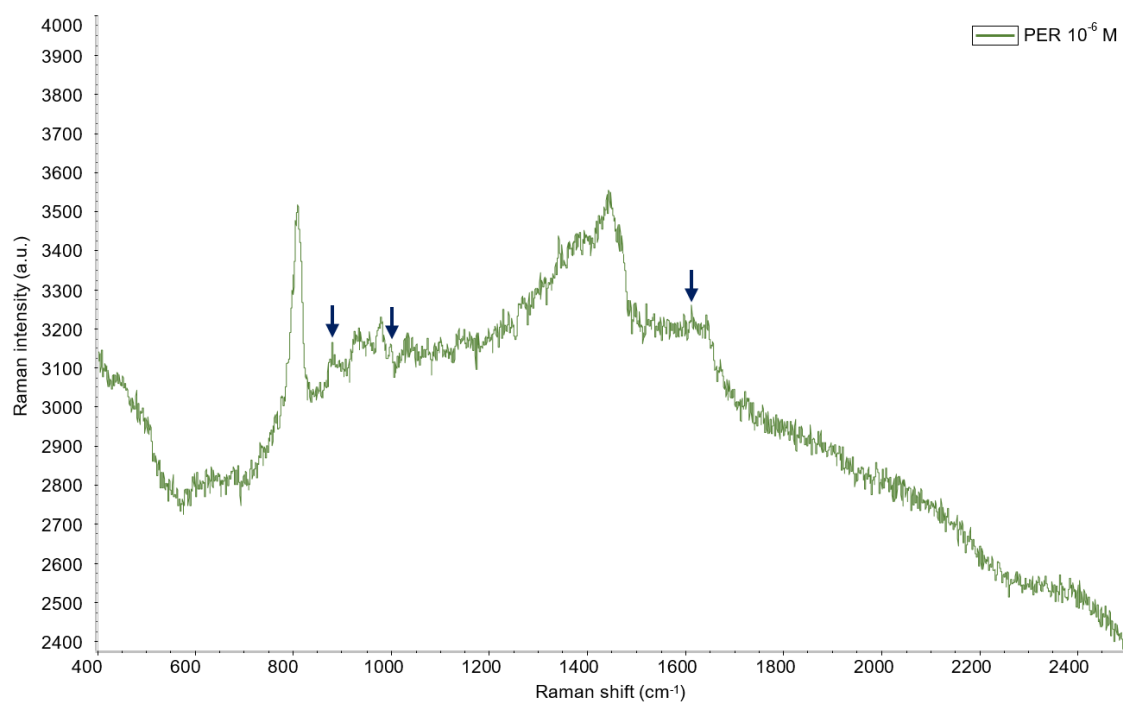
Figure 4.17: SERS spectrum of acidified PER 10^{-6} M. 632.8 nm excitation, $20\times$ objective, 5 mW power, 10 s exposure time (5 averages), dynamic measurement.

4.3.3   The laser choice

In order to assess the dependence of the SERS signal on the excitation wavelength, the SERS spectra of a 10^{-4} M PER solution were collected using both 532 nm and 632.8 nm lasers (20× objective) and compared. The incident power on the sample was comparable, i.e. 3 mW for the 532 nm laser and 5 mW for the 632.8 nm. The results are summarized in figure 4.18; seven main PER bands are clearly visible in both conditions, but the contribution from the fluorescent background (probably arising from the paper support) is much stronger when the 532 nm excitation laser is used. However, if the same spectra are plotted after automatic baseline correction (figure 4.19), most of the differences disappear and similar outcomes are obtained.

Considering that the plasmonic resonance for silver nanoparticles after deposition is peaked at 390 nm, with a shoulder around 500 nm and a broad tail up to 800 nm, both excitation wavelengths can be used for an effective excitation of the plasmon. In order to reduce the fluorescence background presumably coming from the support paper material, the red laser operating at 632.8 nm was selected for all the measurements concerning Perampanel.
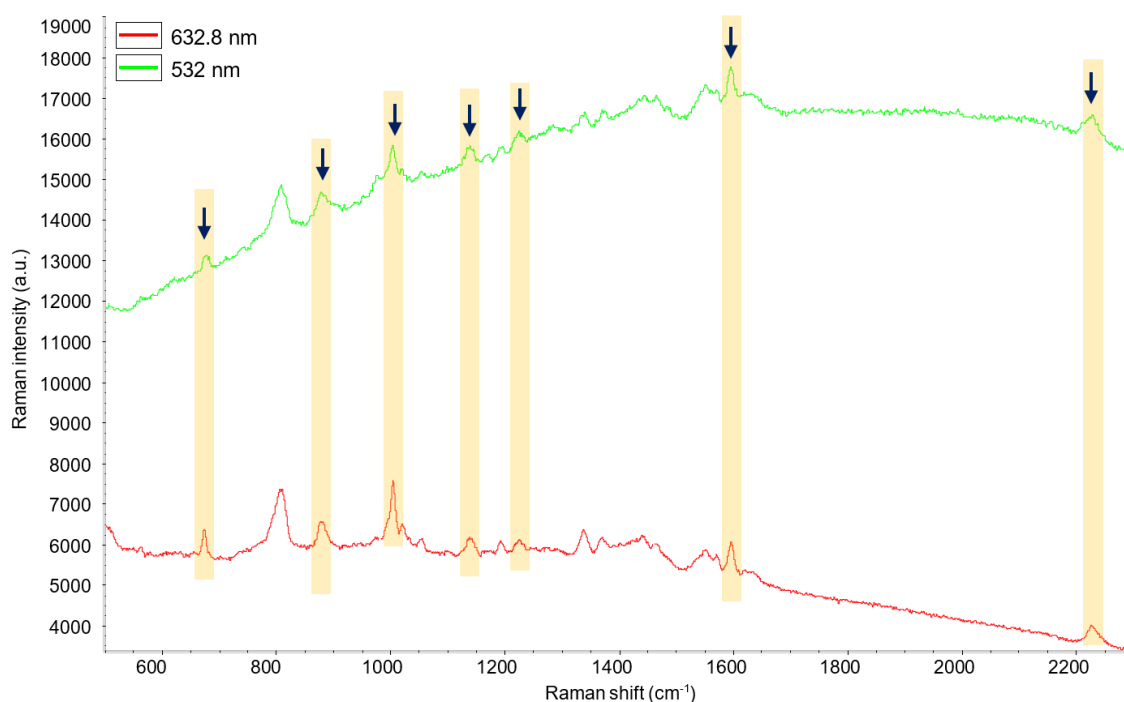
Figure 4.18: SERS spectra of acidified PER 10^{-4} M, recorded with 532 nm (3 mW) and 632.8 nm (5 mW) excitation wavelengths. 20× objective, 10 s exposure time (5 averages), dynamic measurement.
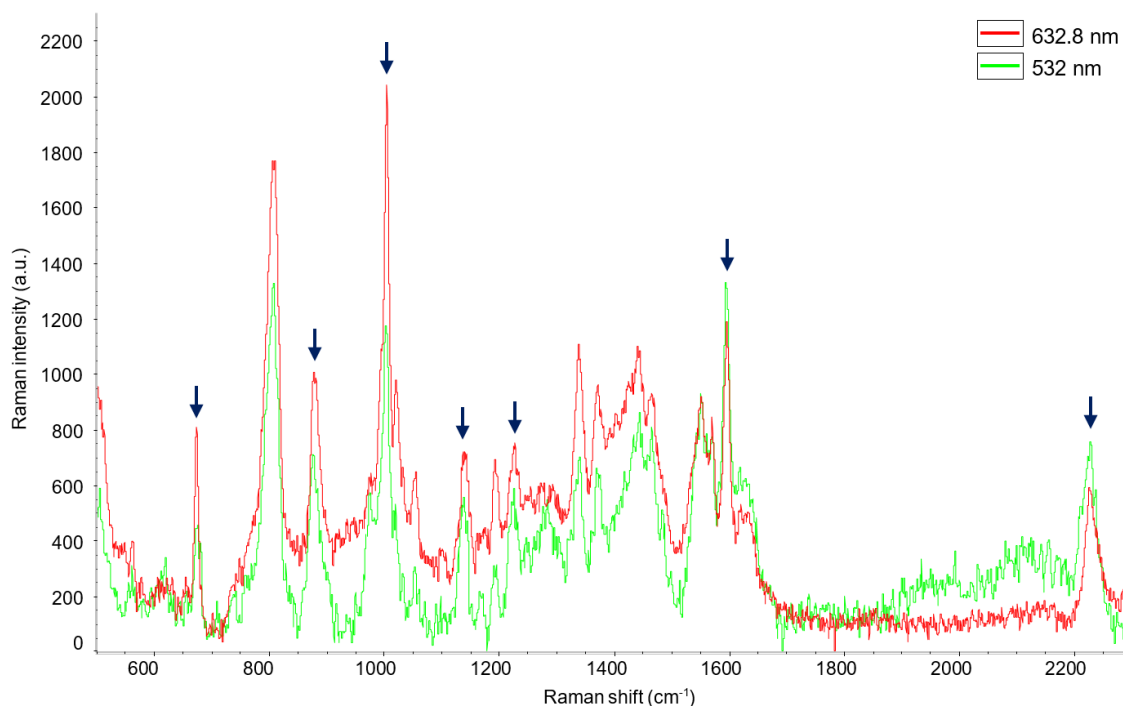
Figure 4.19: SERS spectra after automatic baseline correction of acidified PER 10^{-4} M, recorded with 532 nm (3 mW) and 632.8 nm (5 mW) excitation wavelengths. $20\times$ objective, 10 s exposure time (5 averages), dynamic measurement.

4.3.4 Spatial uniformity

The intra-sample repeatability of the SERS substrates produced by centrifugation (5000 RPM, 15 minutes) was assessed collecting a static SERS spectrum in five different and randomly selected spots within the same substrate. A 8 μL droplet of acidified 10^{-4} M PER solution was deposited onto the substrate and the SERS spectra were recorded after complete drying using the 632.8 nm excitation laser, with $20\times$ objective and 5 mW incident power.

The five static spectra are reported in panel (a) of figure 4.20, with intensities on a common scale. The main PER peaks are visible in any spot, however large differences regarding the peak intensity, the contribution from the background, the signal-to-noise ratio and the relative peak intensity ratios are observed from point to point. In addition, several ephemeral bands are present in static spectra, e.g. at 835 cm^{-1} (spot 1), 977 cm^{-1} (spot 1 and 4) and 1053 cm^{-1} (spot 3). Such peaks, related to thermal fluctuations and local chemical variations, disappear in the spatially-averaged spectrum obtained at the same concentration in dynamic mode (panel (b) of figure 4.20). The dynamic spectrum is also characterized by better resolution and signal-to-noise ratio and, except for bands at 1595 and 2230 cm^{-1}, by a larger peak intensity.
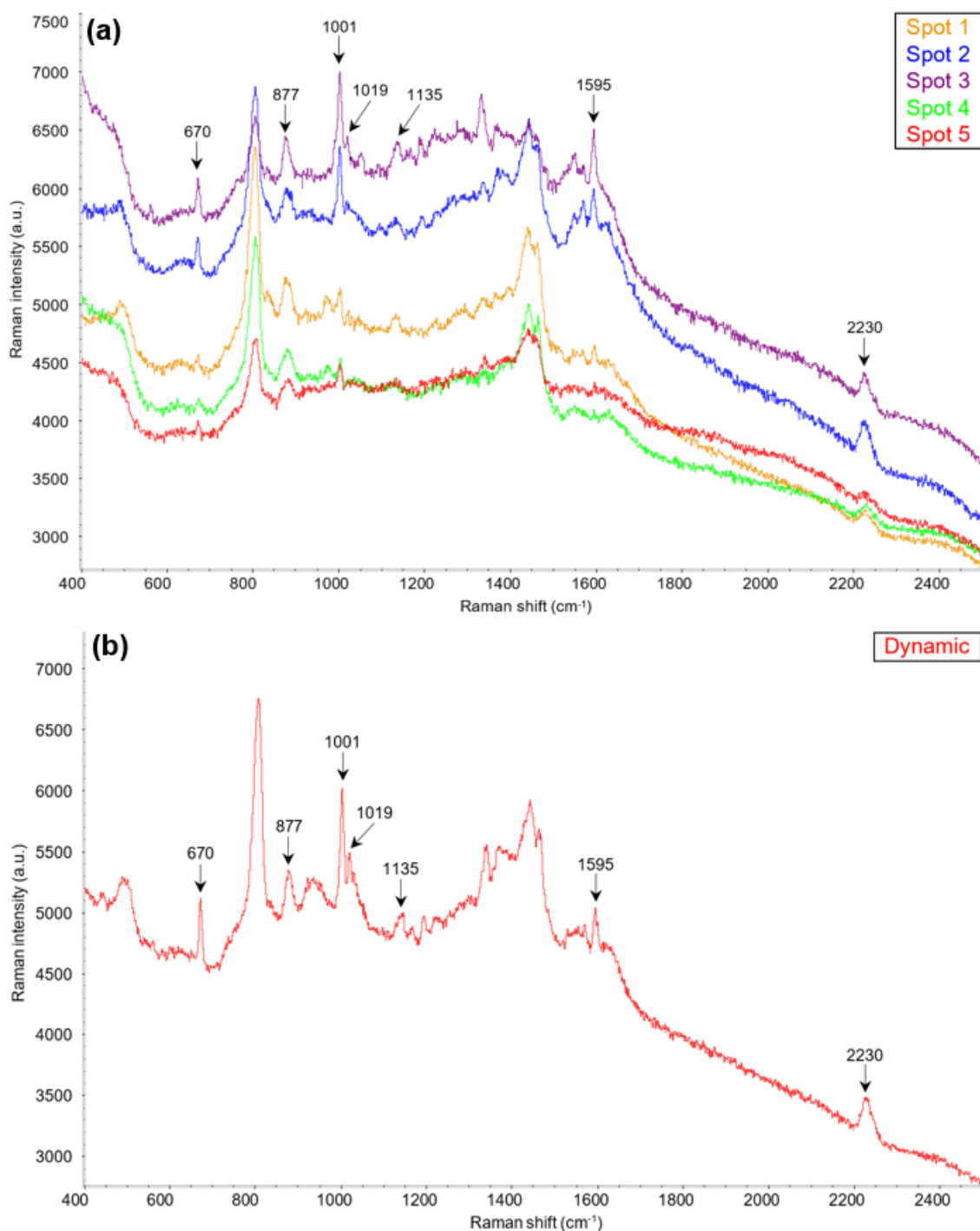
Figure 4.20: SERS spectra of PER 10^{-4} M recorded in static mode in five different spots (a) or in dynamic mode (b). 632.8 nm excitation, 20× objective, 5 mW power, 10 s exposure time (5 averages).

All the intensity values, measured as baseline-corrected peak heights using the tool of the *Omnic* software, are reported in table 4.4 for static and dynamic measurements. The significant variability among the intensities, as well as the locally weak signal of the bands at 1019, 1595 and 2230 cm^{-1} (in spot 4, the peak at 1019 cm^{-1} is not even

visible), indicate that static measurements cannot be used for reliable quantitative SERS detection of PER and should be replaced by dynamic measurements through the spinning cell.

	670 cm^{-1}	877 cm^{-1}	1001 cm^{-1}	1019 cm^{-1}	1595 cm^{-1}	2230 cm^{-1}
Static 1	136	309	310	128	115	138
Static 2	257	259	695	238	326	334
Static 3	271	355	899	339	497	195
Static 4	103	255	208	/	86	129
Static 5	148	178	207	71	90	91
Dynamic	505	372	1021	576	373	274

Table 4.4: Summary of the intensities recorded at six selected peaks during static and dynamic measurements for 10^{-4} M PER.

Chapter 5

Quantitative SERS Detection of Perampanel

In this chapter, the possibility of using paper-based SERS sensors for the quantitative detection of Perampanel will be addressed, considering substrates produced via both natural sedimentation and centrifugation. At the same time, the inter-sample repeatability and the reproducibility of these substrates will be discussed.

5.1 Preparation

5.1.1 Preparation of substrates

SERS substrates were prepared using the natural sedimentation and the centrifugation methods described in chapter 3. Briefly, 35 filter paper pieces (4×5 mm^2) were cut out in a chiral shape (see figure 3.11), thoroughly washed with water and ethanol, and dried under the hood. Then, they were subdivided in the following way:

- 20 pieces were placed on the bottom of 3 mL glass vials and covered with 1 mL of concentrated silver colloid. After 3 days of incubation, the supernatant was removed and the substrates were carefully extracted from the vials and dried.

- 15 pieces were placed on the bottom of 3 mL glass vials and covered with 1 mL of a 10^{-3} M solution of NaCl. After 3 days of incubation, the pieces were extracted from the saline solution and dried, then they were deposited in 8 mL glass vials with 1 mL of concentrated silver colloid and centrifuged at 5000 RPM for 15 minutes. Finally, the substrates were extracted and dried.

The pre-treatment of paper with NaCl was aimed at introducing chlorides on the paper, so as to reduce the background upon the deposition of silver nanoparticles. The saline

solution was prepared by dissolving 1.2 mg of sodium chloride (NaCl anhydrous $\geq$ 99.0%, CAS: 7647-14-5, *Sigma-Aldrich*) in 20 mL of distilled water.

5.1.2   Preparation of analytes

Aqueous solutions at four different PER concentrations were prepared starting from proper volumes of a stock solution of PER 10^{-3} M in methanol. The final volume of 1 mL was reached by adding suitable amounts of an acidified solution at pH = 2 (as reported in table 5.1), obtained by mixing hydrochloric and sulphuric acids in a molar ratio of 1 to 9 (see also table 4.3 in chapter 4).

PER (M)	PER 10^{-3} M in methanol (μL)	pH 2 solution (mL)
10^{-4}	100	0.9
5×10^{-5}	50	0.95
10^{-5}	10	0.99
5×10^{-6}	5	0.995

Table 5.1: The volumes of a 10^{-3} M PER solution in methanol and of a pH 2 aqueous solution to be mixed to obtain the desired acidified PER solutions.

As discussed in [8], the stability of Perampanel in acidic environment is limited to one week. In order to ensure safe and reliable SERS detection, the acidified solutions were prepared just before the measurements.

5.1.3   Raman instrumentation and data processing

All the SERS measurements were carried out in dynamic mode using the 632.8 nm laser, focused with a 20$\times$ objective. The incident power on the sample was fixed to 5 mW, with an exposure time of 10 s. 3 averages were accumulated for each spectrum. A 8 μL droplet was deposited on the substrate, which was mounted in the centre of the spinning cell after complete drying (about 10 minutes after the deposition). Five substrates were used to repeat the measurements for each concentration.

The collected spectra were analysed with the *Omnic^{TM}* software (©1992-2004 Thermo Electron Corporation, version 7.1) and data were processed using *Miscrosoft Office Excel*.

5.2   Results

5.2.1   Testing the substrates produced by sedimentation

In the following figures 5.1 - 5.4, I report the SERS spectra of Perampanel at four different concentrations, recorded on the substrates produced via natural sedimentation during 3-days incubation.

Figure 5.1: SERS spectra of a 10^{-4} M PER solution (pH=2). 632.8 nm excitation, 5 mW power, 10 s exposure time (3 averages). Intensity is in common scale.
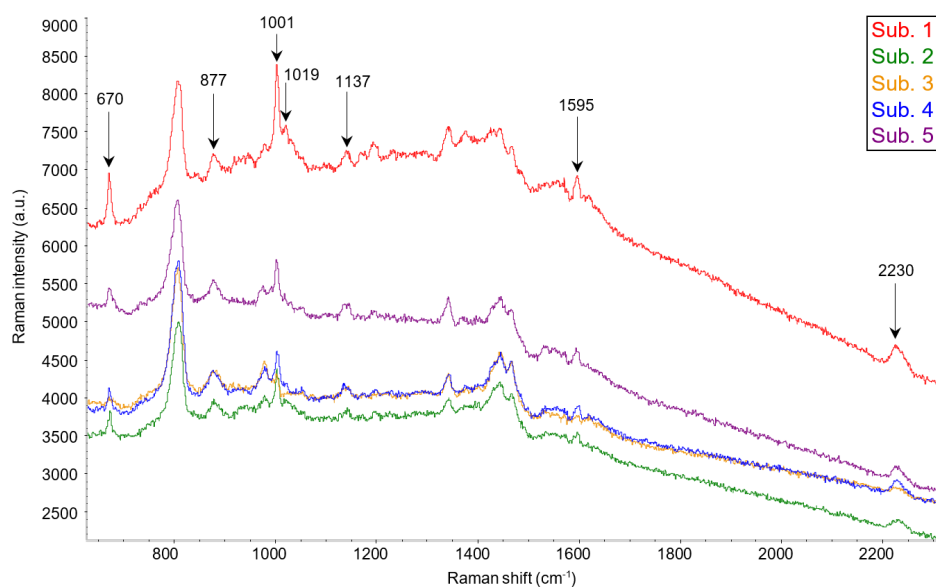
Figure 5.2: SERS spectra of a 5×10^{-5} M PER solution (pH=2). 632.8 nm excitation, 5 mW power, 10 s exposure time (3 averages). Intensity is in common scale.
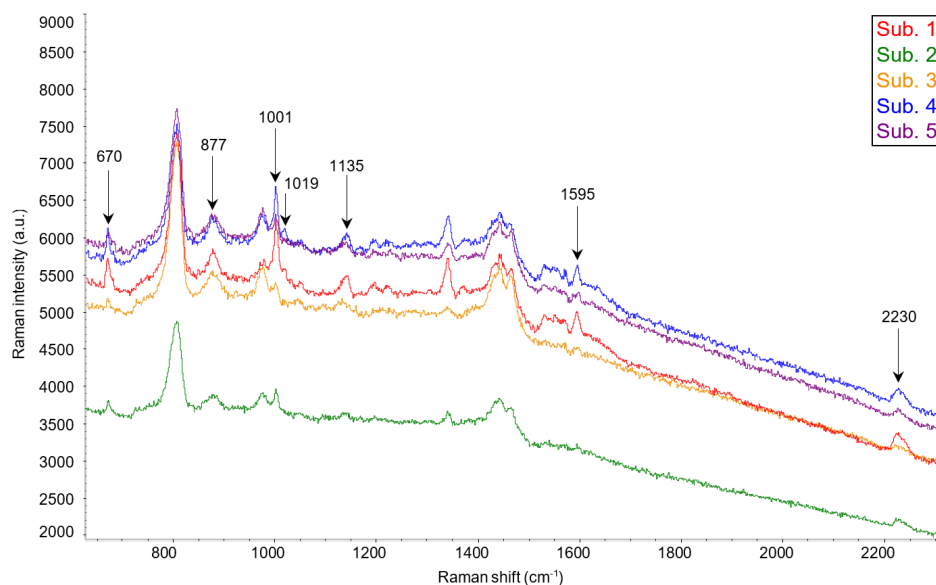
Figure 5.3: SERS spectra of a 10^{-5} M PER solution (pH=2). 632.8 nm excitation, 5 mW power, 10 s exposure time (3 averages). Intensity is in common scale.
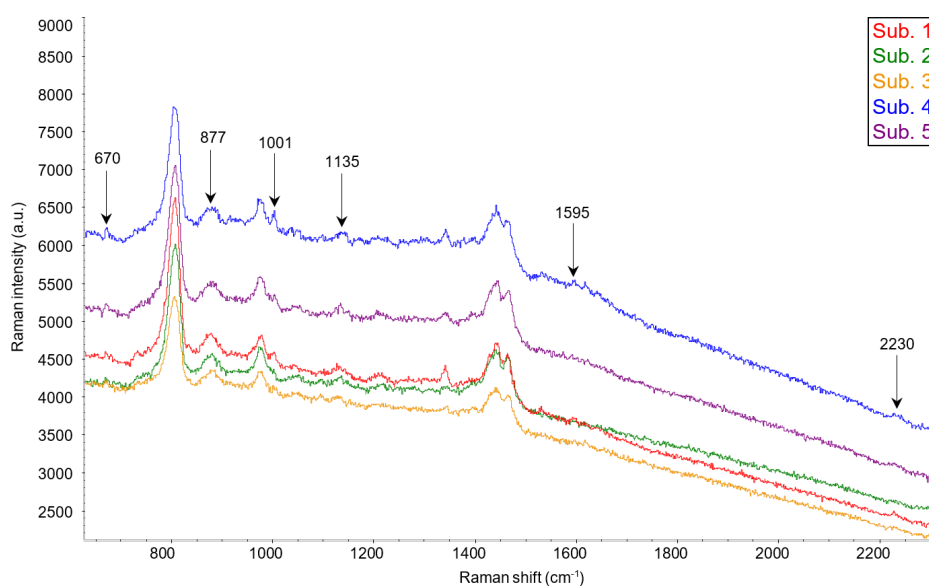
Figure 5.4: SERS spectra of a 5×10^{-6} M PER solution (pH=2). 632.8 nm excitation, 5 mW power, 10 s exposure time (3 averages). Intensity is in common scale.

Looking at the SERS spectra in figures 5.1 - 5.4, seven PER markers (670 cm^{-1}, 877 cm^{-1}, 1001 cm^{-1}, 1019 cm^{-1}, 1135 cm^{-1}, 1595 cm^{-1}, 2230 cm^{-1}) are clearly visible and distinguishable from the background at 10^{-4} M, 5×10^{-5} M and 10^{-5} M. At 5×10^{-6} M, the peak around 1019 cm^{-1} is no more visible, while the peaks at 1135 cm^{-1}, 1595 cm^{-1} and 2230 cm^{-1} are very weak and not always detectable. The intense peak around 807 cm^{-1}, which is not affected by PER concentration, is related to the background, as well as the structured feature between 1300 and 1500 cm^{-1}.

Even if some signals are undoubtedly detected in the spectra corresponding to PER concentration of 5×10^{-6} M, this concentration value can be assumed as the lowest limit of detection for such substrates for reliable PER detection. In figure 5.5, the spectra of PER 10^{-4} M are reported after automatic baseline correction, in order to highlight the peak intensity of the PER markers without the influence of the background. The repeatability across different substrates for the same PER concentration will be examined in detail in the next section.
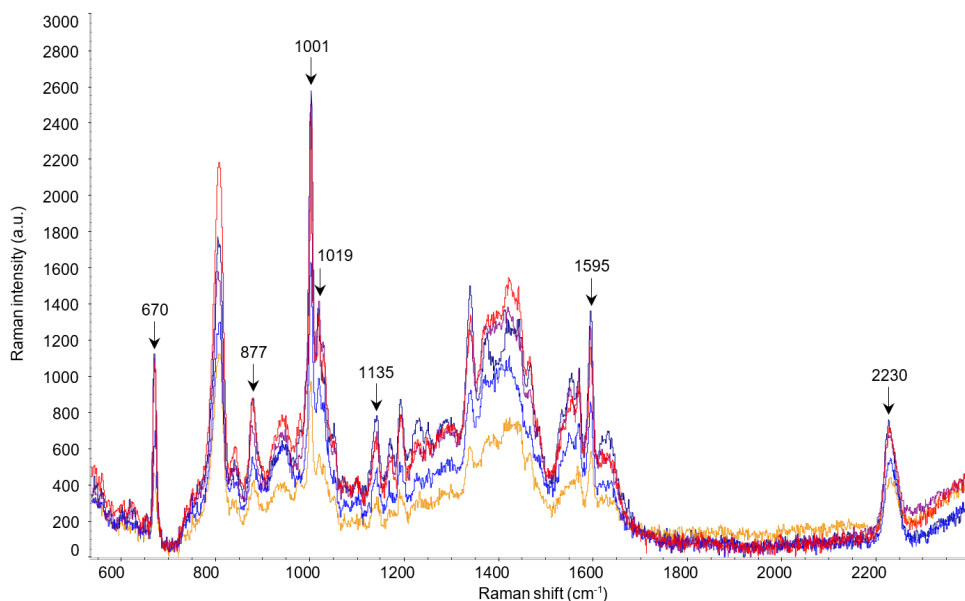
Figure 5.5: SERS spectra of a 10^{-4} M PER solution (pH=2). 632.8 nm excitation, 5 mW power, 10 s exposure time (3 averages). Intensity is in common scale, after automatic baseline correction.

5.2.2   Testing the substrates produced by centrifugation

Before describing the PER spectra, it is worth discussing about the spectral background. The pre-treatment of the paper with NaCl and the subsequent drying before the centrifugation turned out to be ineffective in reducing the background, which was still present in the produced SERS substrates: as reported in figure 5.6, the SERS spectrum collected from the dried bare substrate after centrifugation displays all the typical features of citrate, along with the intense peak at 228 cm^{-1} corresponding to the Ag-OCO^{-} stretching mode. Fortunately, the analyte solution contained additional chlorides coming from hydrochloric acid, therefore the background could be efficiently lowered by the analyte solution itself before the SERS measurements. However, the high content of chlorides on the substrate may have negatively affected PER detection, which could be optimized in future works by avoiding the NaCl pre-treatment.

The SERS spectra of Perampanel at the concentration of 10^{-4} M, 5×10^{-5} M and 10^{-5}

M are reported in figures 5.7, 5.8 and 5.9.
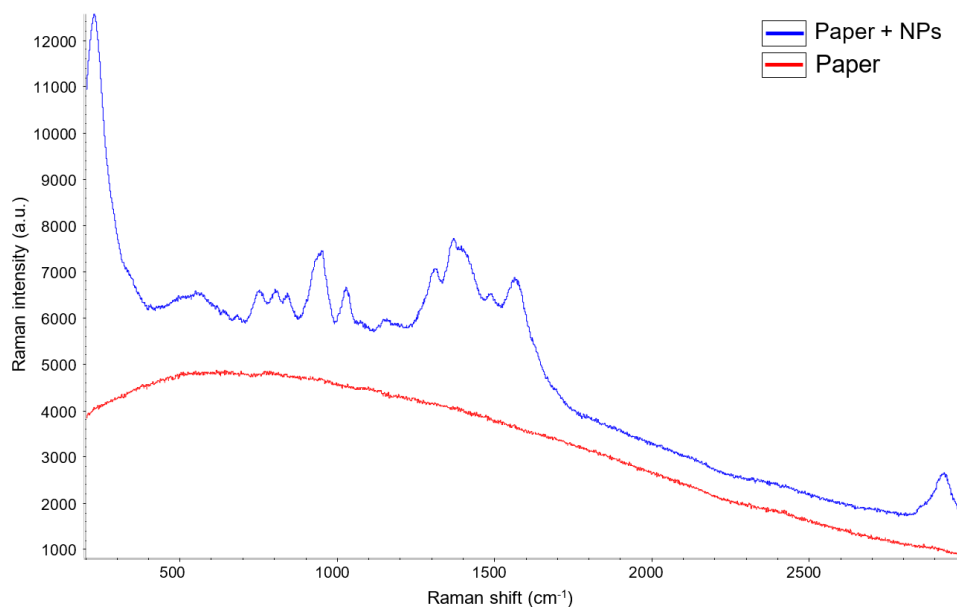
Figure 5.6: Background signal (in blue) coming from a substrate produced via centrifugation and previously treated with NaCl. The red spectrum refers to the treated paper before the deposition of nanoparticles. 632.8 nm excitation, 5 mW power, 10 s exposure time (3 averages).
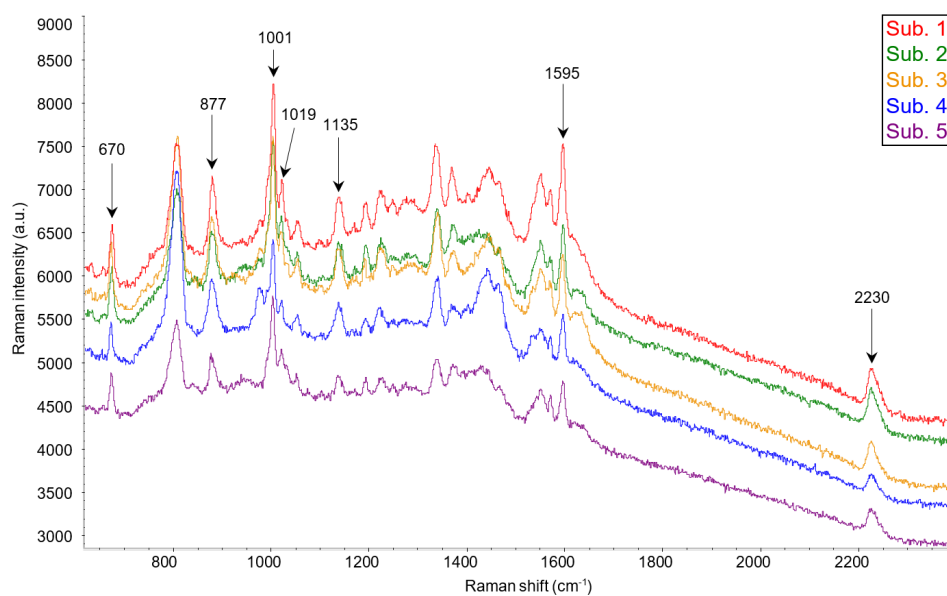
Figure 5.7: SERS spectra of a 10^{-4} M PER solution (pH=2). 632.8 nm excitation, 5 mW power, 10 s exposure time (3 averages). Intensity is in common scale.
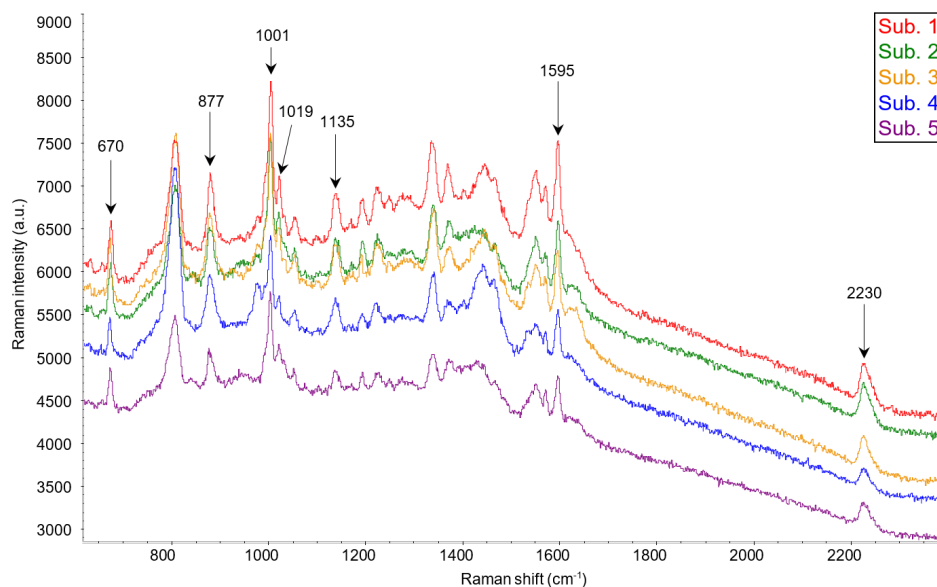
Figure 5.8: SERS spectra of a 5×10^{-5} M PER solution (pH=2). 632.8 nm excitation, 5 mW power, 10 s exposure time (3 averages). Intensity is in common scale.
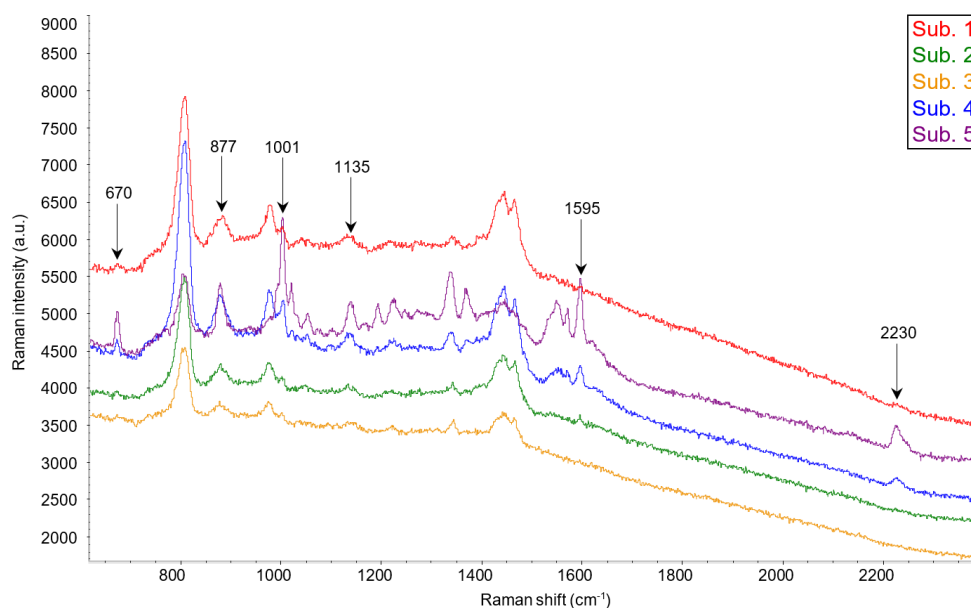
Figure 5.9: SERS spectra of a 10^{-5} M PER solution (pH=2). 632.8 nm excitation, 5 mW power, 10 s exposure time (3 averages). Intensity is in common scale.

The recorded SERS spectra and the background contributions are similar to those obtained with the SERS substrates produced by natural sedimentation. The sensitivity for PER 10^{-5} M is lower than the previous case (see section 5.2.1) and most of the peaks are weak or hardly detectable for this low concentration. Remarkably, the spectrum measured on substrate number 5 is significantly intense compared to the others at the same concentration; since errors during spectra recording or substrate manipulation

cannot be excluded, it will be treated as an outlier and it will not be considered in the following data analysis. The main PER markers (670 cm^{-1}, 877 cm^{-1}, 1001 cm^{-1}, 1135 cm^{-1}, 1595 cm^{-1}, 2230 cm^{-1}) are observable at any concentration, while the most intense features of the background (in particular the peak at 807 cm^{-1} and the structures between 1300 and 1500 cm^{-1}) do not interfere with the most important peaks of Perampanel. In figure 5.10, the spectra of PER 10^{-4} M are reported after automatic baseline correction.
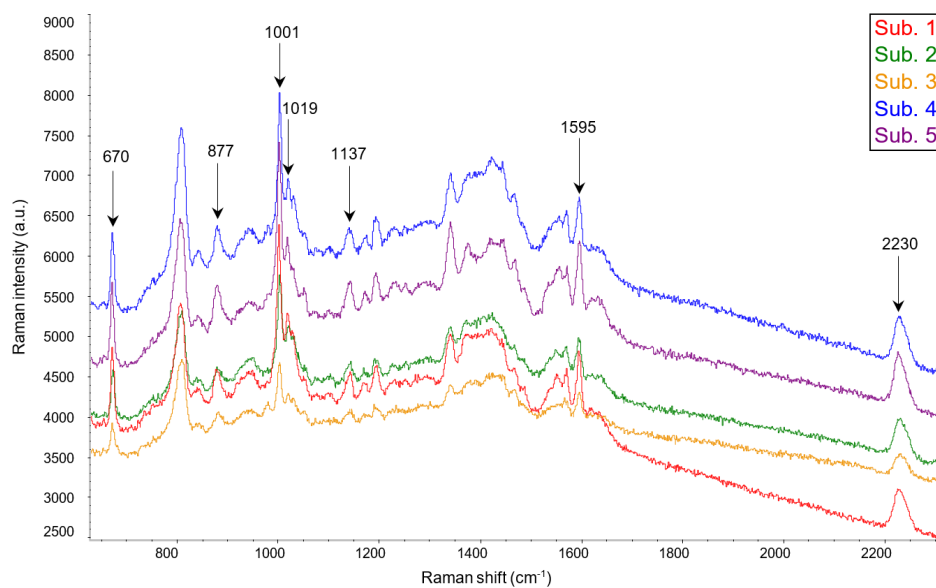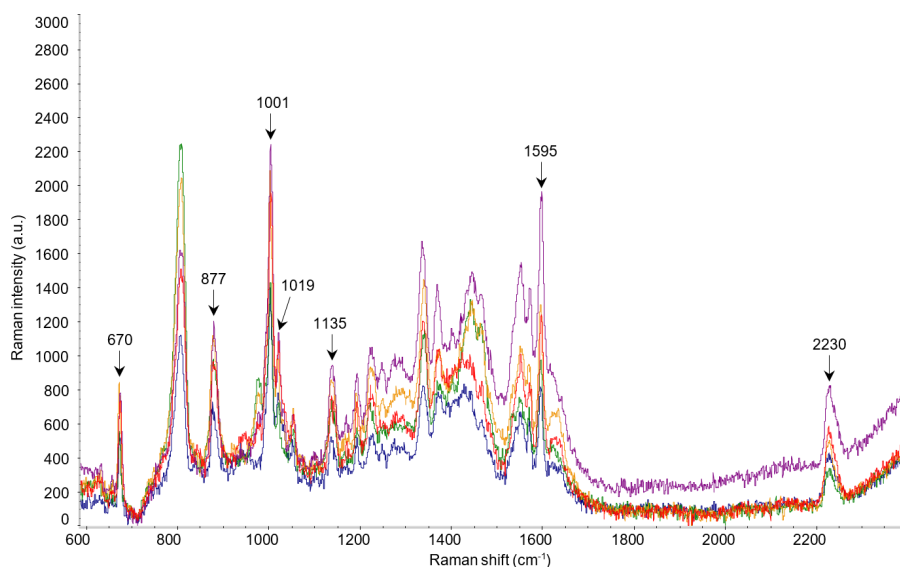

Figure 5.10: SERS spectra of a 10^{-4} M PER solution (pH=2). 632.8 nm excitation, 5 mW power, 10 s exposure time (3 averages). Intensity is in common scale, after automatic baseline correction.

5.3 Assessment of calibration curves

In this section, the response of paper-based sensors as a function of PER concentration is quantified. In particular, calibration curves are produced, which correlate the peak intensity of the main markers with the PER concentration in the range 10^{-4} M - 5×10^{-6} M (for the SERS substrates produced by natural sedimentation) and 10^{-4} M - 10^{-5} M (for the SERS substrates produced by centrifugation). The intensity is reported as peak height with respect to the baseline and is computed using the peak height tool in *Omnic*. To minimize errors during the evaluation of the intensity, only four peaks that are clearly visible and easily resolved at any concentration are considered, i.e. 670 cm^{-1}, 877 cm^{-1}, 1001 cm^{-1} and 2230 cm^{-1}.

For a given concentration, the SERS intensity data are collected over 5 spectra and the average is plotted. Vertical error bars are defined as the average value ± the standard deviation. All the values used in the construction of the calibration curves are reported

in table 5.2 for substrates produced by natural sedimentation and in table 5.3 for those produced by centrifugation.

10^{-4} M	670 cm^{-1}	877 cm^{-1}	1001 cm^{-1}	2230 cm^{-1}
1	1004	398	1989	486
2	573	216	1196	416
3	360	194	664	302
4	898	427	1770	605
5	962	443	2003	616
Average	759	336	1524	485
STDEV	280	121	582	132
5×10^{-5} M	670 cm^{-1}	877 cm^{-1}	1001 cm^{-1}	2230 cm^{-1}
1	630	290	1265	288
2	286	190	593	137
3	93	249	281	78
4	287	260	555	179
5	259	203	620	189
Average	311	238	663	174
STDEV	196	41	363	77
10^{-5} M	670 cm^{-1}	877 cm^{-1}	1001 cm^{-1}	2230 cm^{-1}
1	400	339	844	261
2	155	186	328	110
3	72	230	301	87
4	343	326	757	195
5	182	276	376	121
Average	230	271	521	155
STDEV	137	64	258	72
5×10^{-6} M	670 cm^{-1}	877 cm^{-1}	1001 cm^{-1}	2230 cm^{-1}
1	94	216	205	67
2	98	271	144	51
3	91	192	134	52
4	145	205	261	66
5	129	158	198	47
Average	111	208	188	57
STDEV	24	41	51	9

Table 5.2: Summary of the intensities recorded at each peak and on each substrate (produced by natural sedimentation) for PER concentrations of 10^{-4} M, 5×10^{-5} M, 10^{-5} M and 5×10^{-6} M. The corresponding averages and standard deviations are also reported.

10^{-4} M	670 cm^{-1}	877 cm^{-1}	1001 cm^{-1}	2230 cm^{-1}
1	605	756	1822	436
2	607	571	1458	420
3	649	674	1624	355
4	426	582	1058	214
5	400	388	1050	244
Average	537	594	1402	334
STDEV	115	138	343	101
5×10^{-5} M	670 cm^{-1}	877 cm^{-1}	1001 cm^{-1}	2230 cm^{-1}
1	691	523	1510	409
2	423	414	979	247
3	403	374	824	274
4	655	521	1435	328
5	201	326	600	391
Average	475	432	1070	330
STDEV	201	88	393	71
10^{-5} M	670 cm^{-1}	877 cm^{-1}	1001 cm^{-1}	2230 cm^{-1}
1	64	362	246	72
2	79	268	177	51
3	60	210	130	/
4	195	548	486	146
5	*469*	*601*	*1424*	*318*
Average	100	347	260	90
STDEV	64	148	158	50

Table 5.3: Summary of the intensities recorded at each peak and on each substrate (produced by centrifugation) for PER concentrations of 10^{-4} M, 5×10^{-5} M and 10^{-5} M. The corresponding averages and standard deviations are also reported.
Note: considering PER 10^{-5} M, the peak at 2230 cm^{-1} is not visible on substrate number 3. In addition, data on substrate number 5 are outliers and are not considered in the calculation of average and standard deviation.

For any concentration and peak, the standard deviation was calculated using equation 5.1, where N is the number of values in the data set:

$$\text{STDEV} = \sqrt{\frac{\sum_i (I_i - I_{av.})^2}{N - 1}} \tag{5.1}$$

Finally, the calibration curves of the four main SERS peaks for PER are reported in figures 5.11 and 5.12 for substrates produced by both methods. In spite of non-negligible error bars, the average intensity displays an increasing trend as concentration increases, which can be fitted by linear curves with acceptable coefficients of determination.
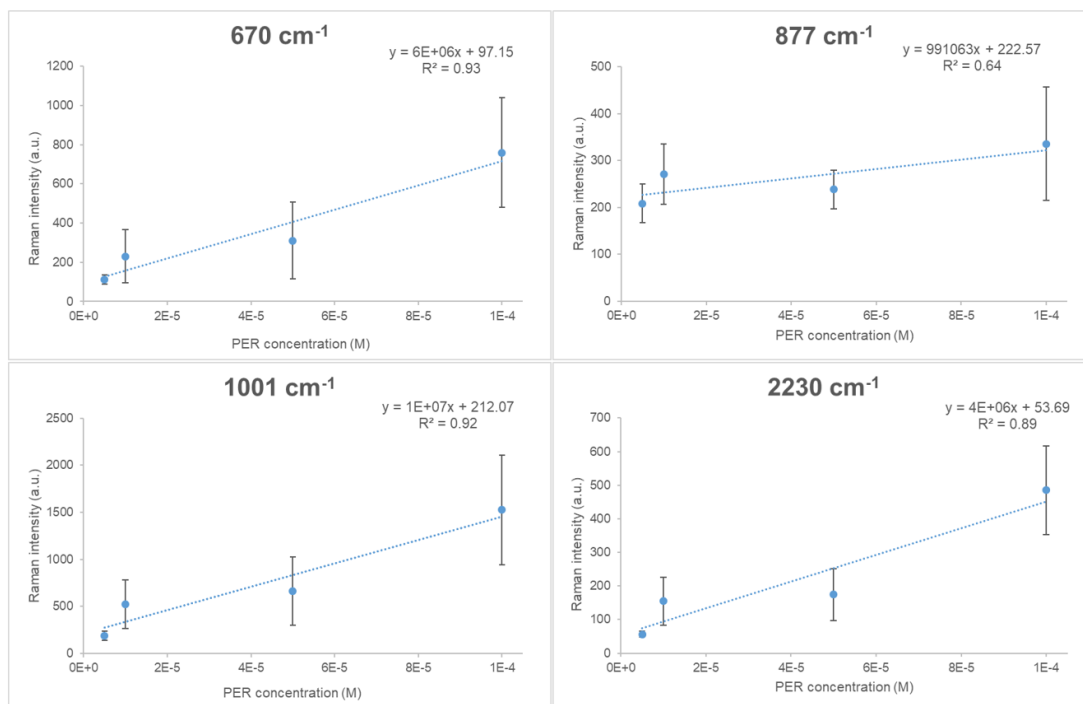
Figure 5.11: Calibration curves at four main PER peaks (substrates via sedimentation). The intensity average is plotted for any concentration and vertical error bars correspond to $\pm$ the standard deviations. The equation of the trendline and the coefficient of determination R^2 are also reported.
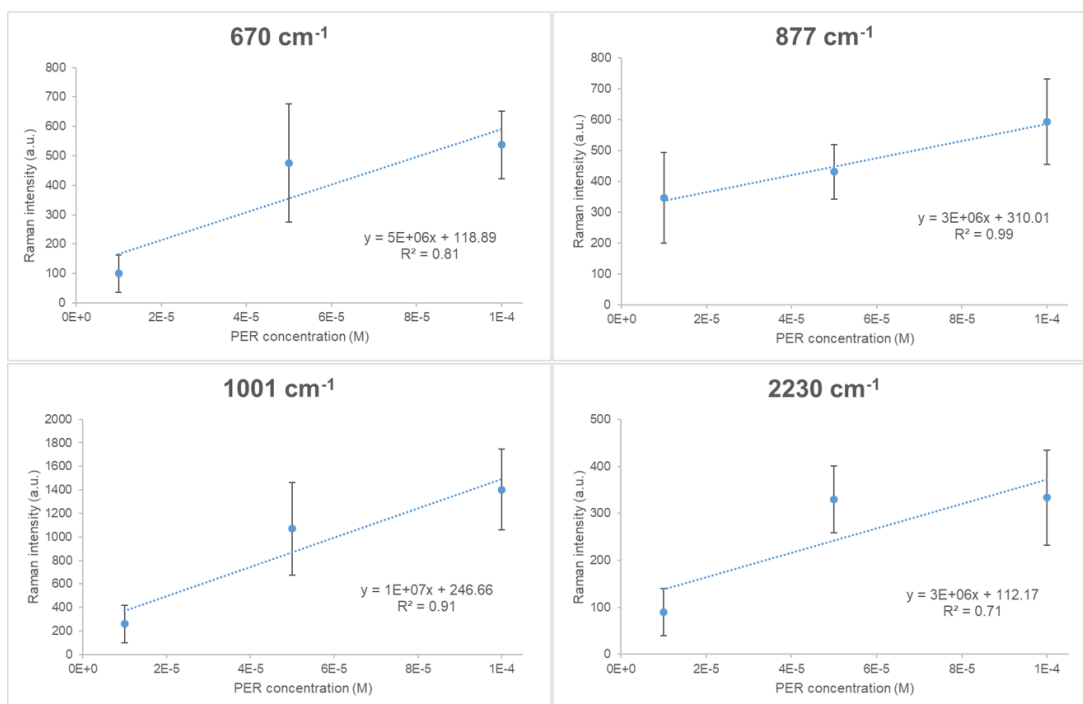
Figure 5.12: Calibration curves at four main PER peaks (substrates via centrifugation). The intensity average is plotted for any concentration and vertical error bars correspond to $\pm$ the standard deviations. The equation of the trendline and the coefficient of determination R^2 are also reported.

Nevertheless, the values reported in the previous tables show a quite large variability of intensity across different substrates for the same concentration and peak, therefore the inter-sample repeatability and reproducibility should be improved. These large variations are clearly underlined by extended error bars and could be ascribed to the production method and to the experimental procedure, which should be optimized to reduce the substrate handling and manipulation as much as possible. Indeed, the extraction of wet substrates from vials, the differential drying, the sample handling using tweezers and the positioning on the spinning cell may not only increase the risk of contamination but also alter the morphology of the silver layer on paper, leading to non-uniform SERS enhancement.

A concluding remark regards the stability of the signal over time. The SERS spectra of PER 10^{-4} M on substrates produced via both natural sedimentation and centrifugation were collected 36 hours after the deposition and compared to the SERS spectra recorded 15 minutes after the deposition (with same experimental parameters). No significant variations were observed and the signal was still good after 36 hours, especially for the substrates produced by centrifugation.

Chapter 6

SERS Detection of Cannabidiol

Paper-based sensors produced via centrifugation have proved their effectiveness in detecting Perampanel in a concentration range between 10^{-4} M and 5×10^{-6} M, with a possible further improvement if the production conditions are optimized. In this chapter, similar substrates will be applied to SERS detection of another analyte, i.e. Cannabidiol (CBD). Similarly to PER, CBD is used in the treatment of epilepsy.

6.1 Preparation

6.1.1 Preparation of substrates and analyte

The SERS substrates were produced following the usual centrifugation procedure: some 4×5 mm^2 filter paper pieces were cut out in a chiral shape (see figure 3.11), thoroughly washed with water and ethanol, and dried. Then, they were placed in 8 mL glass vials with 1 mL of concentrated silver colloid and centrifuged at 5000 RPM for 15 minutes. At the end of the process, they were extracted and dried. To decrease the background, the substrates were treated before SERS measurements with an acidic solution at pH 2 (containing hydrochloric and sulphuric acids in molar ratio of 1:9) or, alternatively, with a 10^{-3} M solution of NaCl. This treatment parallels the one used for PER in chapter 4.

A 10^{-3} M CBD solution was prepared by dissolving 1 mg of CBD powder (courtesy of Cinzia Citti, CNR-NANOTEC, Institute of Nanotechnology, Lecce) in 3.2 mL of ethanol ($\geq$ 99.8%, CAS: 64-17-5, *Honeywell Riedel-de-Haën*$^{\text{TM}}$). The CBD powder was stored in a refrigerator at 2 °C. Then, 100 μL of the prepared solution were diluted with 0.9 mL of ethanol to obtain a 10^{-4} M CBD solution.

In addition, a second solution containing CBD and magnesium chloride ($MgCl_2$) was prepared, in order to test the effect of this salt on the SERS enhancement of CBD, as proposed in [47]. First of all, a 10^{-2} M solution of magnesium chloride was prepared by dissolving 1 mg of anhydrous $MgCl_2$ ($\geq$ 98.0%, CAS: 7786-30-30, *Sigma-Aldrich*) in 1 mL of distilled water; then, 0.1 mL of this solution were mixed with 0.9 mL of an ethanol solution of CBD 10^{-4} M. The final concentrations of CBD and $MgCl_2$ were, respectively, about 10^{-4} M and 10^{-3} M. Remarkably, the use of $MgCl_2$ also provides the activating effect of chlorides, with no need of pre-treating the substrates.

6.1.2   Raman setup

The SERS measurements were performed in dynamic mode on spinning substrates using 632.8 nm and 532 nm lasers, both focused with a 20$\times$ objective. The incident power on the sample ranged from 0.5 mW to 12.5 mW for the red laser and was equal to 0.3 mW for the green laser, with an exposure time of 10 s (5 averages). A 8 μL droplet of the solution to be analysed was deposited on the SERS substrate, which was mounted in the centre of the spinning cell. The SERS measurements were carried out both immediately after the drop casting (i.e. during drying) and on completely dried substrates.

6.2   Results without $MgCl_2$

The SERS spectra recorded with 632.8 nm laser during drying and after complete drying of the ethanol solution do not display any characteristic peak of CBD. This is not surprising, since CBD 10^{-4} M was hardly detectable also on silver substrates deposited on more performing supports like silicon and DLC, as assessed in a parallel master's thesis. The background contribution was effectively reduced by the pre-treatment with both hydrochloric acid and sodium chloride, but the CBD analyte could not be detected in any situation. All these experimental results are reported in figure 6.1.

The detectability of CBD did not improve if the spectra were recorded on wet substrates (differently from silicon-supported solid substrates), while the use of the 532 nm excitation laser caused a further increase of the background because of fluorescence (spectra not shown).
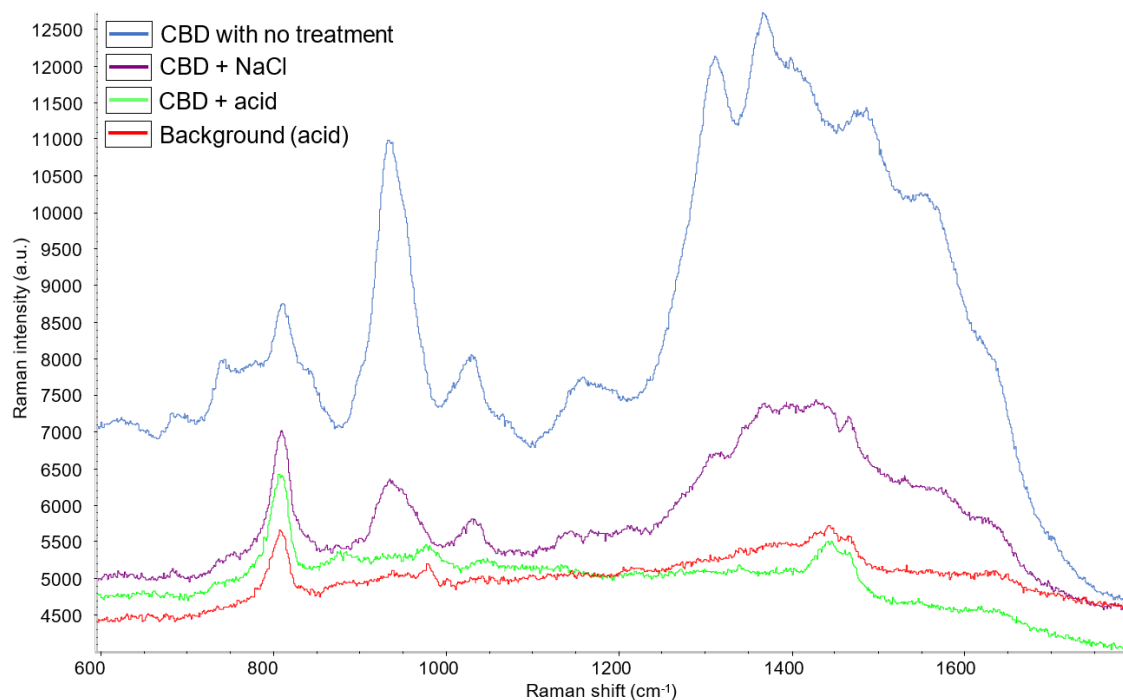
Figure 6.1: SERS spectra of CBD 10^{-4} M in ethanol on untreated and treated dried substrates. The background signal of the bare substrate after acidic treatment is also reported. 632.8 nm excitation, $20\times$ objective, 5 mW power, 10s exposure time (5 averages), dynamic measurement.

6.3   Results with MgCl$_2$

6.3.1   Effect of magnesium cations

The beneficial effect of MgCl$_2$ on the SERS detection has been reported in several works dealing with organic molecules of toxicological interest, including THC, cannabinol, Cannabidiol [47], synthetic cannabinoids [71, 72], and benzodiazepines [73]. Compared to other chloride-containing salts, MgCl$_2$ in optimized concentration provided the largest signal enhancement, the best sensitivity and the lowest limit of detection as a result of a combined effect of chloride anions and Mg cations. However, the exact contribution of Mg^{2+} ions to the enhancement is unclear and just a few studies have systematically investigated the effect of cations on SERS activation (see for instance [73]). Considering the particular case of Cannabidiol, magnesium could form a cationic coordination complex with CBD, mediating the interaction with silver nanoparticles, as discussed below.

Divalent magnesium is the fourth most common metal cation involved in biological activities: it participates in more than 80% of metabolic functions, governing over 350 of enzymatic processes, and is a cofactor for more than 300 enzymes and 800 proteins

[74]. Because of its small ionic radius and relatively high charge density, Mg^{2+} is considered a hard ion and tends to bind to hard oxygen-containing ligands like water, carboxylates, phosphates, hydroxyls, and carbonyls, including many bio-relevant molecules [74, 75]. The oxophilicity of magnesium is so strong that approximately 77% of interactions are Mg-O bonds, while the second most common situation is a Mg-N bond [76]. In the majority of cases, Mg-O complexes are six-coordinated with an octahedral (or distorted octahedral) geometry in the inner coordination sphere [74, 75]. In aqueous environments, Mg^{2+} binds six water molecules and generates the *hexaaquomagnesium* ion. Magnesium-water complexes are so stable and rigid that the removal of a water molecule from the inner coordination sphere of the Mg cation implies a free energy penalty of 40-80 kcal/mol [75] and the complex tends to interact as an independent entity with other organic ligands via hydrogen bonds (outer-sphere coordination) [76]. Water ligands may be effectively displaced in non-aqueous environments and when the dielectric constant of the local medium decreases [75, 76].

Although Mg^{2+}-CBD interactions have not been reported in the literature, the chemical structure of Cannabidiol is suitable for complexation and its hydroxyl groups and double bonds may act as effective ligands. In order to verify the stability of a guess Mg-CBD coordination complex, a DFT calculation at the B3LYP/6-31G(d,p) level was carried out and the optimized geometry was examined with the molecular editor *Avogadro*. The optimization was performed under the following simplifying assumptions:

- The coordination number of magnesium cation is equal to 6.

- The presence of water, coming from the concentrated $MgCl_2$ solution, is neglected, since ethanol is by far the prevalent solvent.

- Because of the relatively low concentration of CBD, only one CBD molecule is involved in the complex.

As a result, the final, stable coordination compound consists of one Mg^{2+} cation interacting with four ethanol molecules and one CBD molecule. The optimized geometry after DFT calculation is reported in figure 6.2, in which a distorted octahedral geometry can be clearly recognized. Magnesium accepts lone pair electrons from the oxygen atoms of the hydroxyl groups (four of ethanol and one of CBD) and π electrons from the double bond of the cyclohexene ring of CBD (figure 6.3).

The binding energy of the complex is estimated (neglecting basis set superposition errors) to be:

$$BE = (4E_{EtOH} + E_{Mg^{2+}} + E_{CBD}) - E_{complex} = 360.5\,\text{kcal/mol} \qquad (6.1)$$

which corresponds to an average BE per ligand of 60 kcal/mol. This value fits in the expected range of 40-80 kcal/mol [75].

	Energy (kcal/mol)
Complex	-1122470.5
EtOH	-97292.965
Mg²⁺	-125017.05
CBD	-607921.08
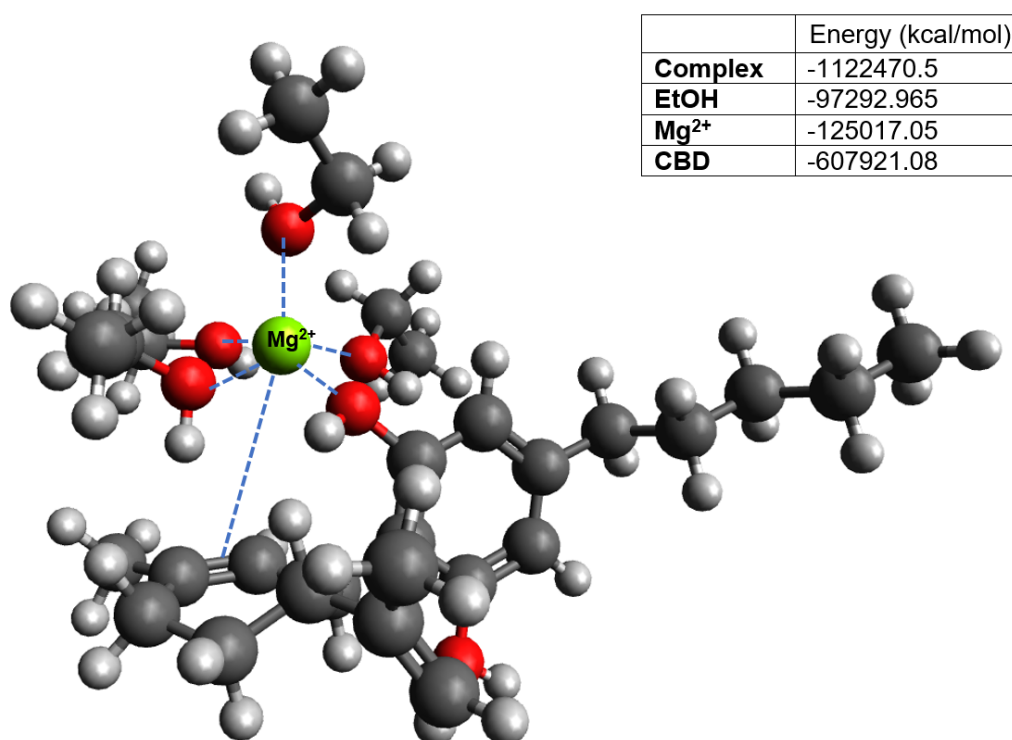
Figure 6.2: Model of Mg-ethanol-CBD complex after DFT optimization (rendering of the model by *Avogadro* software [77]). The energy values used in equation 6.1 are reported in the inset.
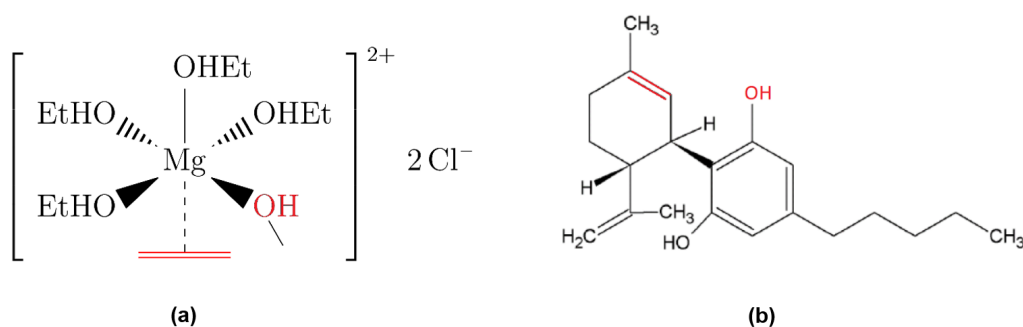
Figure 6.3: (a) Schematic representation of the coordination compound (for sake of simplicity, the entire CBD molecule is not reported); (b) CBD molecular structure. In both panels, the CBD functionalities involved in the complex are highlighted in red.

The resulting complex has a net positive charge (cationic complex) and can interact electrostatically with the negatively charged surface of silver nanoparticles, covered by chloride and citrate anions. Therefore, a neutral molecule like CBD can be driven to the SERS active site via complexation and subsequent polar attraction. Additional

interactions between magnesium and silver, with formation of alloys or intermetallics [78] on the top of the bulk silver nanoparticles, might provide a further contribution to chemical and electromagnetic enhancement, even if more detailed investigation should be performed to prove this idea. It is important to note that the hypotheses about complex formation and magnesium-silver affinity are reasonable and consistent with literature data, but require supplementary theoretical and experimental confirmations that are beyond the scope of my thesis.

6.3.2   SERS spectra of CBD

Unfortunately, the SERS spectra of CBD + $MgCl_2$ were not as satisfactory as expected. Indeed, the strong contribution from the background, along with the intrinsic signal weakness of CBD, hindered the identification of any reliable characteristic peak. In addition, literature data reported two CBD peaks at 807 and 1444 cm^{-1} [47], but such features of CBD are exactly in correspondence of the strongest spectral features of the background (see figure 6.4).
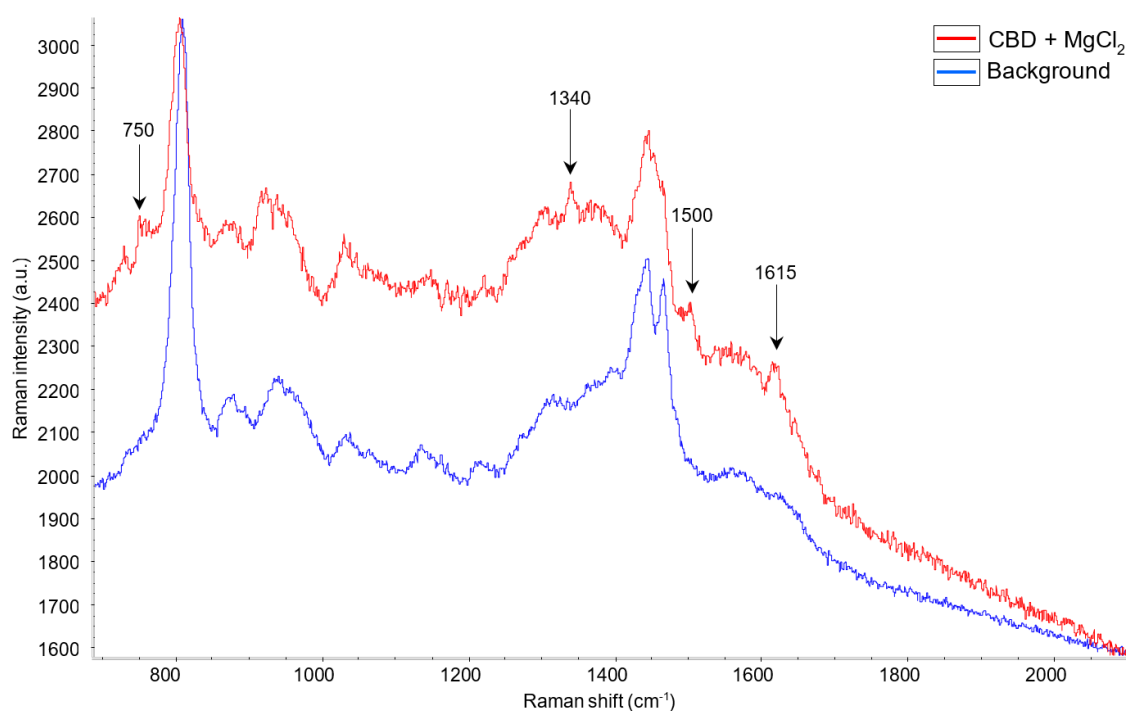
Figure 6.4: SERS spectrum of CBD 10^{-4} M in ethanol + $MgCl_2$ on wet substrate. The background signal of the bare substrate after treatment with NaCl is also reported. 632.8 nm excitation, 20× objective, 5 mW power, 10s exposure time (5 averages), dynamic measurement. Intensities are not in common scale so as to better highlight the differences with respect to the background.

The only peaks that are clearly distinguished from the background are those indicated by arrows in figure 6.4 and centred, respectively, at 750, 1340, 1500 and 1615 cm^{-1}. In

particular, the peaks at 1500 and 1615 cm^{-1} are located in the spectral range of C=C stretching vibrations for alkenes, cyclohexene and benzene rings (approximately 1620-1680 cm^{-1} for alkenes and 1430-1625 cm^{-1} for benzene [64]) and may be originated from the double bonds of CBD. However, the intensity is rather weak on the top of a strong background so that a reliable assignment to CBD modes cannot be made, especially without additional markers in other spectral regions. Finally, the above-mentioned peaks tend to become less intense and to disappear as the substrate dries, indicating a possible influence of the solvent on the SERS detection of the analyte.

To sum up, paper-based SERS sensors produced by centrifugation turned out to be ineffective in detecting Cannabidiol at the concentration of 10^{-4} M, even with the addition of MgCl$_2$, whose enhancing property has been proved in the literature [47, 72]. Since the experimental parameters (CBD concentration, type of solvent, excitation laser) are quite similar to those reported in the literature, the problem may be related to the substrate itself rather than to the analyte, in particular to the strong background and to the low affinity of silver-coated filter paper. Therefore, an optimization of production and recording processes is necessary to make this kind of substrates appropriate for the SERS detection of Cannabidiol.

Chapter 7

Other Production Methods

The fabrication of SERS substrates via centrifugation allowed significantly shorter production times with respect to natural sedimentation during incubation, with comparable final results. In this chapter, alternative methods for an easy, cheap, and fast realization of Ag-based substrates will be described and the sensing behaviour of such substrates will be checked using the same solutions of Perampanel discussed in chapter 4. Lastly, the preparation and testing of a few paper-made substrates based on gold will be presented.

7.1 Alternative Ag-based substrates

7.1.1 Preparation during Lee-Meisel synthesis

To avoid the use of the centrifuge and to increase the number of substrates produced simultaneously, some SERS substrates were directly produced during the synthesis of the silver colloid (*in situ* reduction). A Lee-Meisel starting solution was prepared dissolving 7.2 mg of AgNO$_3$ in 40 mL of distilled water and was brought to boiling, then it was mixed with a 1% solution of TSC (8 mg in 0.8 mL of water) [53]. At the same time, about 20 pieces of filter paper, properly cleaned and prepared (as in chapter 3), were added to the boiling solution and the system was kept reacting under magnetic stirring for one hour. The paper provided sites for heterogeneous nucleation of nanoparticles during the reduction by TSC: a change of the paper colour from white to yellow, and finally to red was a clear evidence of the growth of silver on the paper (figure 7.1). Reduction occurred also in the bulk solution, whose colour turned greyish-yellow as in a traditional Lee-Meisel synthesis without paper. After cooling, the paper pieces were carefully extracted from the flask and dried under the hood.

The magnetic stirring made the paper pieces fluctuate in the solution during the whole

synthesis and cooling, therefore the growth of silver nanoparticles took place on both sides of each paper piece and the problem of recognizing the active side was eliminated. Moreover, the substrates were less manipulated, as the extraction from the synthesis flask was simpler than the one from the centrifugation vials. Finally, the silver colloid was not separately synthesized and concentrated, resulting in a further reduction of the production times.
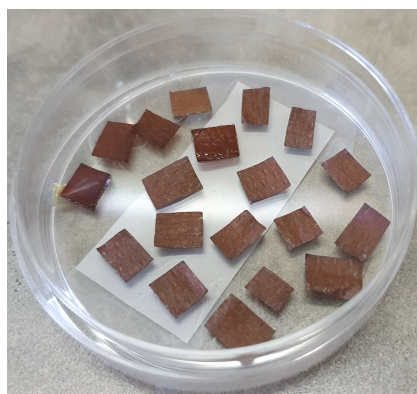
Figure 7.1: SERS substrates produced during Lee-Meisel colloidal synthesis.

7.1.2 *In situ* reduction without TSC

The preparation method described previously can be implemented without the addition of TSC. Indeed, filter paper consists of fibres made of cellulose, a polysaccharide consisting of linear chains of $\beta(1,4)$-linked D-glucose units (figure 7.2) [79]. Glucose is a well-known reducing agent [14] and polysaccharides contain many hydroxyl groups and a hemiacetal end that are able to reduce metallic salts [79]. For example, the oxidation of polysaccharide OH functionalities to carbonyl groups is involved in the formation of gold nanoparticles [79] and nano-crystalline cellulose is exploited as both a reducing and a stabilizing agent for silver nanoparticles [80]. However, cellulose has a weak reduction capability and the exploitation of silver ions is typically low in the absence of additional reducing agents or alkaline compounds able to accelerate the reaction [81].
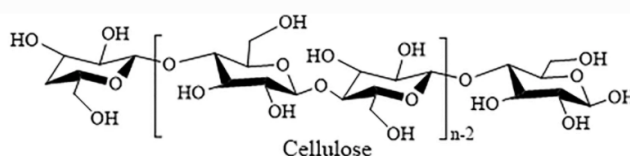
Figure 7.2: Chemical structure of cellulose (adapted from [14]).

The reducing effect of paper itself was tested by dispersing 10 filter paper pieces in a solution of silver nitrate (20 mg of $AgNO_3$ dissolved in 40 mL of distilled water), then

the system was heated under magnetic stirring. The reaction started below the boiling point of the solution and was underlined by a change in the paper colour from white to pale yellow, to orange. After 90 minutes, the colour did not change any more and the reaction was stopped. The final substrates were characterized by a softer colouration with respect to the synthesis with TSC (figure 7.3), probably indicating a decreased silver content. This result agrees with the poor reducing capability of cellulose alone reported in the literature [81].

Figure 7.3: SERS substrates produced by direct paper reduction, without TSC.

Unlike the synthesis with TSC, silver reduction did not start in the bulk solution, which remained clear and transparent during the whole reaction time. After cooling, the paper pieces were carefully extracted from the flask and dried under the hood.

7.2 Characterization of novel Ag-based substrates

7.2.1 UV-VIS reflectance

The substrates were investigated by means of UV-VIS-NIR reflectance spectroscopy with the integrating sphere setup of the Jasco V-570 spectrophotometer. After recording of a proper baseline with the reference blank material (PTFE), the substrates were mounted on the PTFE board through a double-sided tape and placed in front of the sample port. The spectra and the related substrate photographs are reported in figure 7.4, along with the reflectance spectrum of a substrate produced by centrifugation.

The observed colour of each substrate can be explained on the basis of the corresponding reflectance spectrum. The substrate in panel a has a reddish colour: the reflectance starts to decrease significantly already for $\lambda < 600$ nm, with a strong absorption in the green-blue-violet spectral region (380-565 nm). Similarly, the substrate in panel b has an orange colour, because the reflectance in the green region (500-565 nm) is larger than case a and the minimum is shifted towards the blue.
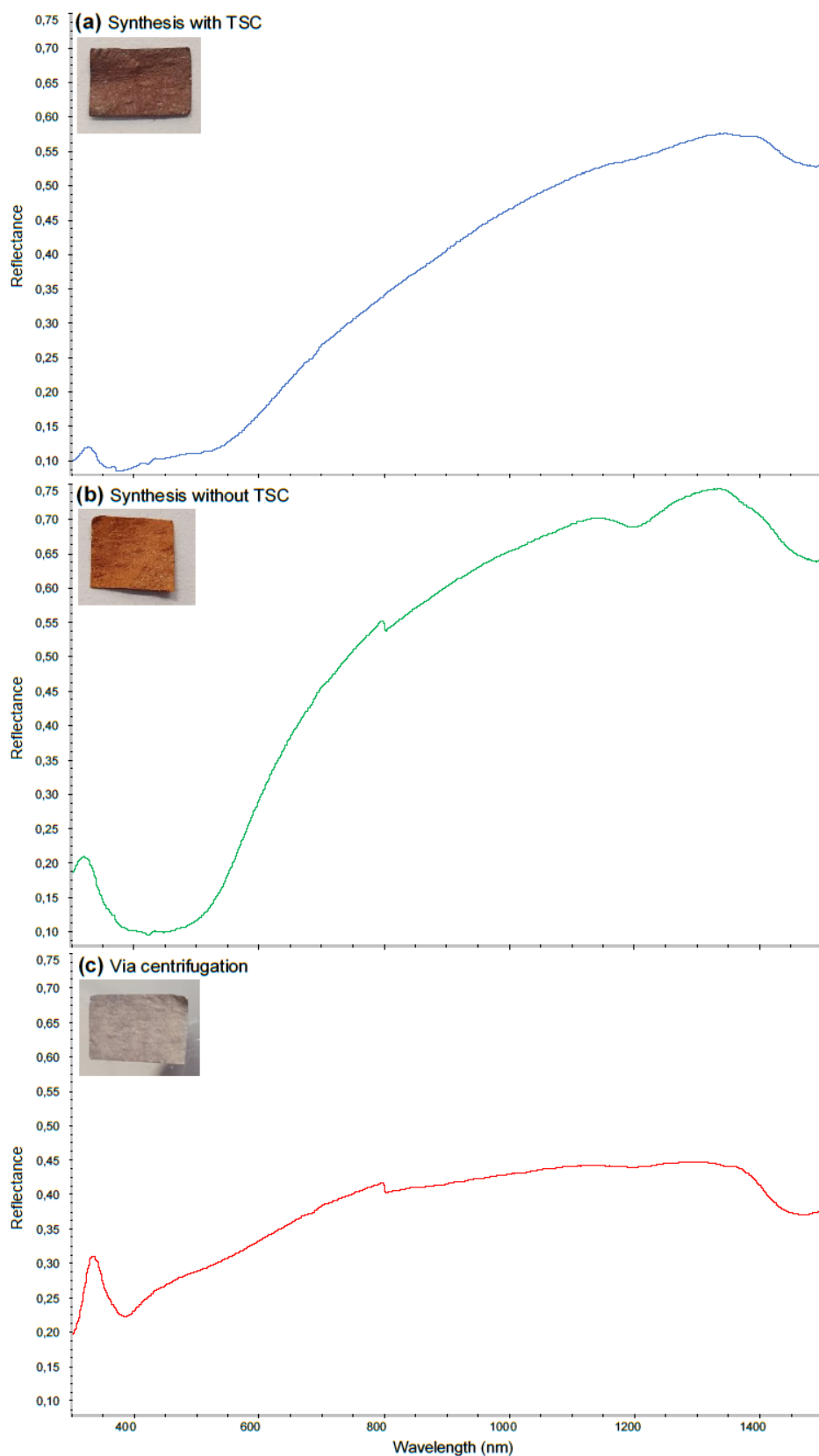
Figure 7.4: (a, b) UV-VIS reflectance spectra of substrates produced during the colloidal synthesis with and without TSC. (c) UV-VIS reflectance spectrum of a substrate produced via centrifugation. A photograph of each substrate is reported in the insets. Spectra are in common scale.

Finally, the spectrum in panel *c* resembles the one of the concentrated silver colloid but it is blue-shifted; compared to the spectra *a-b*, the reflectance has a relatively restricted variation across the visible range (i.e. from 0.4 in the red to 0.22 in the blue), with a minimum at 384 nm. As a result, the spectrum is flatter, all the wavelengths are fairly equally absorbed/reflected, and the substrate appears grey, with a yellowish tone because of the minimum in the violet-blue region. The grey colour, along with a low reflectance in the NIR (i.e. beyond 800 nm), is a proof of nanoparticle aggregation.

A final remark on the spectra *a-c*: the step at 800 nm is an artefact caused by the imprecise compensation of the instrumentation when the diffraction grating is changed during the wavelength scan of the measurement. In addition, the instrument works reliably when the reflectance is larger than 0.2 and, consequently, the shape and the position of the minimum of reflectance in spectra *a* and *b* are not accurate.

7.2.2 Morphological investigation by SEM

The morphology of the substrates produced by *in situ* reduction with and without the use of TSC as reducing agent was also investigated by the *Zeiss* Supra 40 FE-SEM.
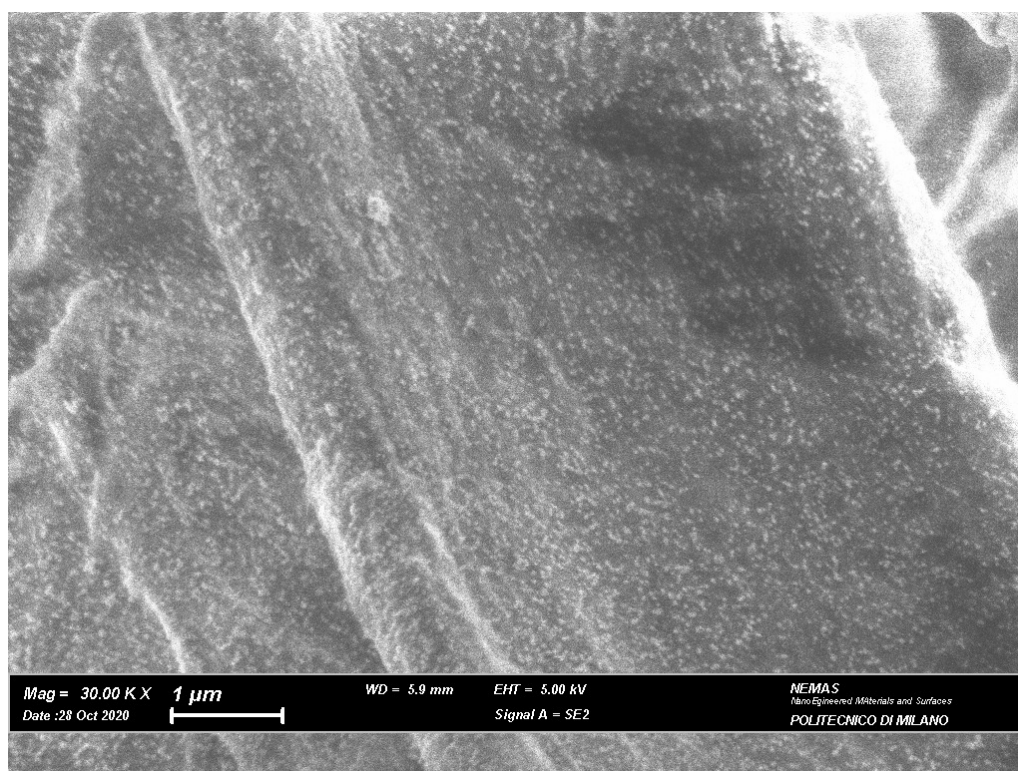
Figure 7.5: SEM image of SERS substrate produced by *in situ* reduction with TSC (EHT = 5 kV, WD = 5.9 mm, 30000×).

When reduction is promoted by citrate, paper fibres are entirely decorated with regular and round nanoparticles that tend to stay apart without aggregating (see figure 7.5). The average size, estimated using *ImageJ* [58], is about 40 nm. Interestingly, no rods are present and, as depicted in the close-ups of figure 7.6, most of the particles are nearly spherical with a relatively uniform size distribution.
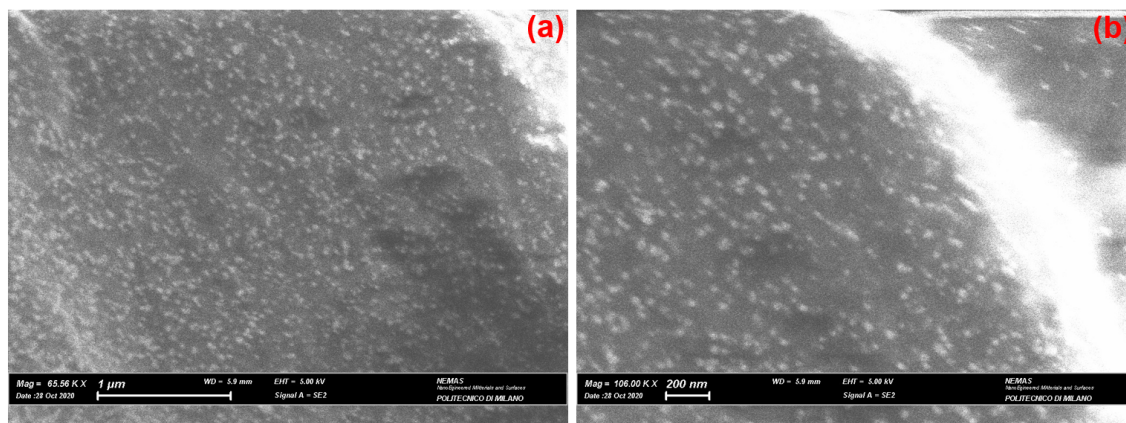
Figure 7.6: SEM images of SERS substrate produced by *in situ* reduction with TSC (EHT = 5 kV, WD = 5.9 mm, 65560× and 106000×).

On the contrary, direct reduction by cellulose functional groups in the absence of TSC leads to more irregular and isolated nanoparticles (see figure 7.7), whose average size, estimated using *ImageJ*, is about 55 nm. Similarly to the previous case, nanorods are absent, however a variety of sizes and shapes is observed, including prismatic and triangular structures as the ones highlighted by the red circles in figure 7.8. Although silver tetrahedrons, truncated tetrahedrons and triangular prisms have been reported in the literature (e.g., [82, 83]), these sharp-edged structures may also be ascribed to residues of unreacted silver nitrate crystallized during substrate drying.
Nevertheless, the colour had already changed from white to orange during the immersion in aqueous environment (where silver nitrate is highly soluble) and the colour was stable upon washing with water, indicating that Ag reduction may have actually occurred and that silver nanoparticles have been synthesized. Indeed, the same orange colour had been detected also during *in situ* reduction with citrate before the paper turned reddish.

Finally, the density of nanoparticles per unit surface differs significantly in the two cases, being approximately 135-150 NP/μm^2 in the substrate produced in the presence of TSC and 30-55 NP/μm^2 in the substrate prepared without TSC, confirming the poor exploitation of silver ions when an additional reducing agent is not used. The combined effect of different average size, shape, density and spacing among particles

determines the final colour and the UV-VIS-NIR reflectance spectrum of the substrate, and affects the SERS behaviour of the sensors, as presented in the next section.
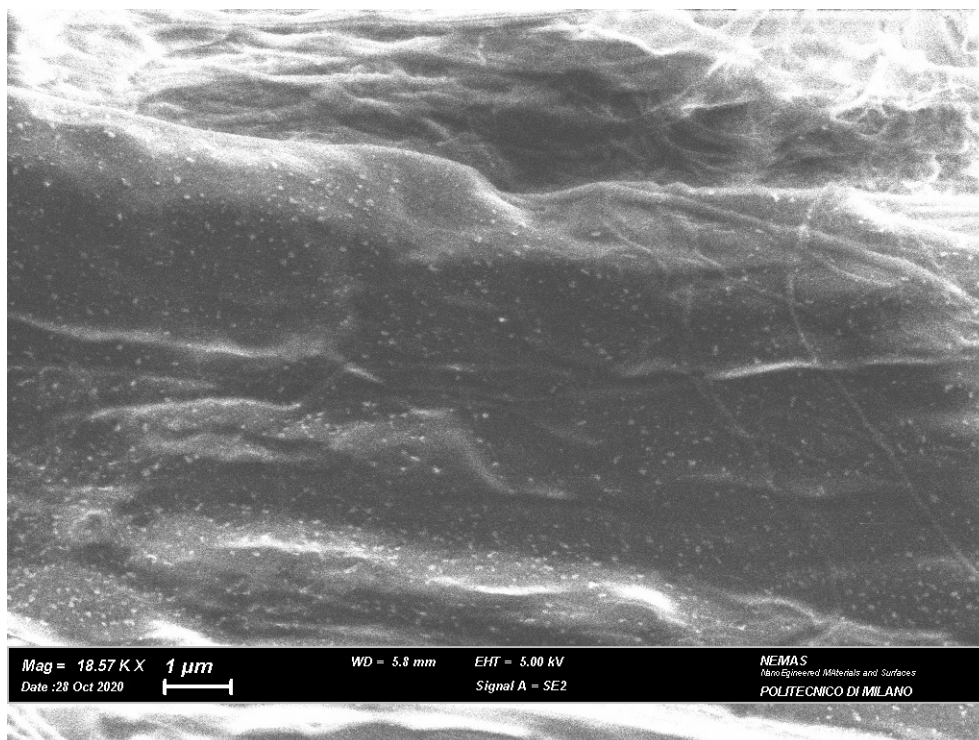
Figure 7.7: SEM image of SERS substrate produced by *in situ* reduction without TSC (EHT = 5 kV, WD = 5.8 mm, 18570×).
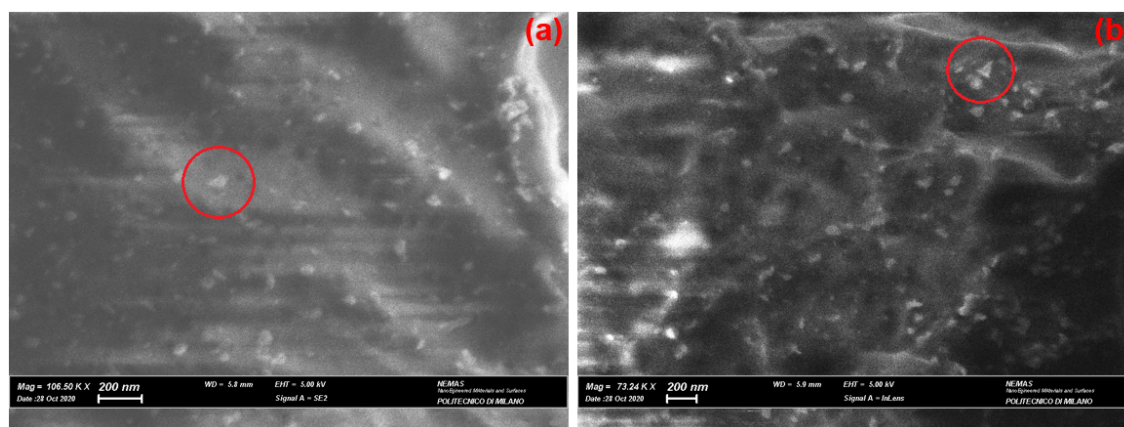
Figure 7.8: SEM images of SERS substrate produced by *in situ* reduction without TSC (EHT = 5 kV, WD = 5.9 mm, 106500× and 73240×).

7.3 Early SERS tests

First of all, the background spectra of the SERS substrates produced with and without TSC were recorded in dynamic mode using the 632.8 nm excitation ($20\times$ objective, 0.5 mW incident power). As depicted in figure 7.9, the background in the presence of TSC as reducing agent is as structured as the one of the SERS substrate produced by centrifugation, even if the intensity (with equal incident power) is lower. On the other hand, the background is still quite intense but almost flat when TSC is not used, and the low-frequency peak (corresponding to the Ag-OCO$^-$ stretching mode of adsorbed citrate) is absent. The latter observation confirms the effect of citrate anions on the background signal of the SERS substrates produced with TSC.
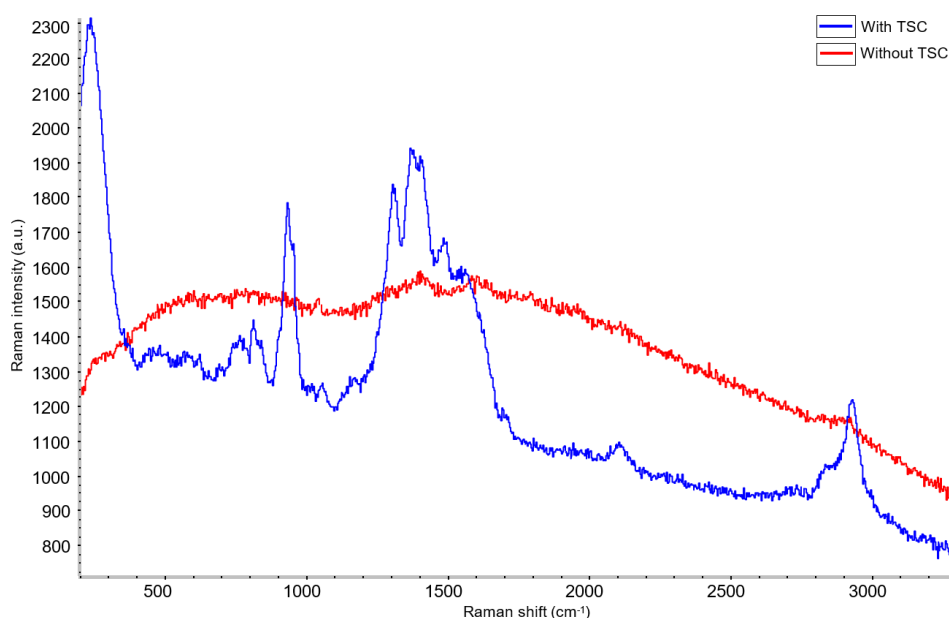
Figure 7.9: Background spectra of the substrates produced during colloidal synthesis with and without TSC as reducing agent. 632.8 nm excitation, $20\times$ objective, 0.5 mW power, 10 s exposure time (5 averages). Intensity is in common scale.

Afterwards, both SERS substrates were tested with 10 μL of acidified PER solutions (10^{-4} and 10^{-5} M) and the corresponding SERS spectra were collected using the spinning-cell setup and the 632.8 nm excitation ($20\times$ objective, 5 mW). The resulting spectra are shown in figures 7.10 and 7.11. Perampanel is clearly detectable on the substrate produced with trisodium citrate as reducing agent: the main PER markers at about 670, 1001, 1019, 1595 and 2230 cm^{-1} are relatively intense and well defined at both concentrations and the background is sufficiently quenched thanks to the activating effect of the chloride-containing solution used for the preparation of the sample (see chapter 4). However, no characteristic signal of PER is observed on substrates

synthesized without TSC, suggesting that the silver content on the paper support is too scarce or with unsuitable morphology. The SERS measurements were carried out a few days after the production, therefore the peaks of figure 7.11 may be ascribed to contamination or degradation of the silver layer due to exposure to air.
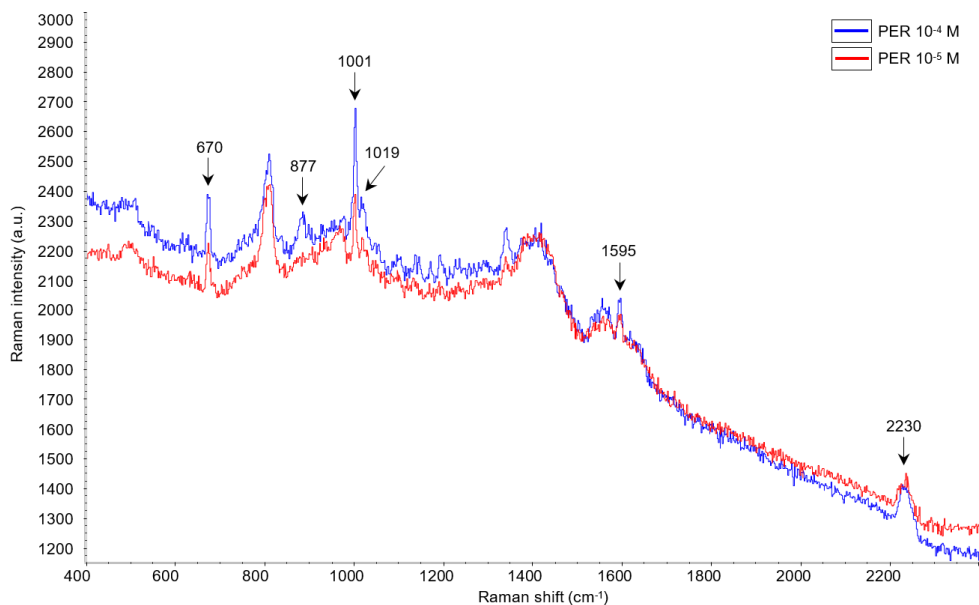
Figure 7.10: SERS spectra of acidified PER 10^{-4} and 10^{-5} M on substrates produced with TSC as reducing agent. 632.8 nm excitation, $20\times$ objective, 5 mW power, 10 s exposure time (5 averages). Intensity is in common scale.
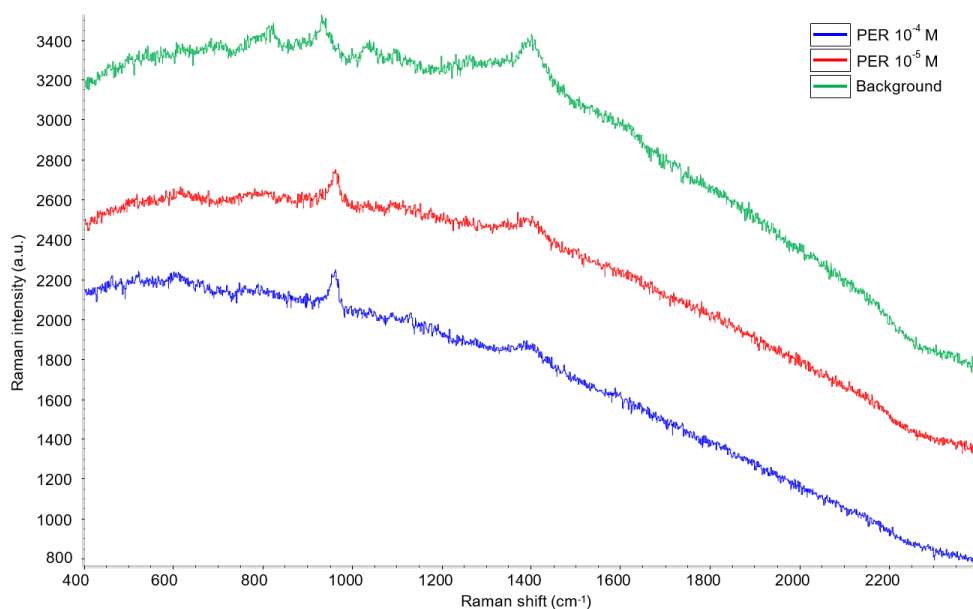
Figure 7.11: SERS spectra of acidified PER 10^{-4} and 10^{-5} M on substrates produced without TSC. 632.8 nm excitation, $20\times$ objective, 5 mW power, 10 s exposure time (5 averages). The background spectrum is also reported. Intensity is in common scale.

The previous outcomes are justified by the markedly different nanoparticle density observed with SEM on the two SERS substrates. As nanoparticles aggregation promotes the formation of the hot spots required for SERS action, it is clear that the higher NP density of the SERS substrates produced with TSC ($\approx$ 140 NP/μm^2) is beneficial compared to the lower NP density of the SERS substrates produced without TSC ($\approx$ 40 NP/μm^2).

Taking everything into account, the use of trisodium citrate as external reducing agent allows the increase of the silver content and the achievement of SERS signals comparable to those collected from substrates produced via natural sedimentation and centrifugation, even if the background is still a problem and should be attenuated with a proper chloride treatment. On the other hand, the exploitation of cellulose functional groups eliminates the drawbacks related to the presence of citrate, but the silver content is greatly reduced and the final substrate is not adequate for SERS sensing. Longer reaction times and the use of an alkaline reaction environment (e.g., NaOH) could increase the NP density and could be worth testing in future investigation. Indeed, paper-based SERS sensors produced directly during the colloidal synthesis provide a promising alternative to speed up the production process with decreasing contamination risk and significantly improved reproducibility. The optimization of the synthesis parameters such as the concentration of silver nitrate, the concentration of TSC, the availability of paper surface and the volume of the reaction batch, as well as a better matching with the plasmon resonance condition using a blue excitation radiation (e.g., 405 nm laser), may significantly improve the SERS results. Similarly, the use of reducing agents other than sodium citrate (glucose, ascorbic acid [81] or sodium borohydride [14]) and a proper pre-treatment of paper may reduce the background contribution, whereas the addition of alkaline compounds like sodium hydroxide, ammonia and sodium carbonate will promote the reduction reaction, increasing the silver content in the SERS substrate [81].

7.4 Au-based SERS substrates

7.4.1 Synthesis and characterization of the gold colloid

Gold colloids were prepared following the Turkevich method [84] and starting from a stock solution of chloroauric acid (HAuCl$_4$ $\cdot$ 3H$_2$O) with a 2.54×10^{-2} M concentration of Au.

- 1 ml of the stock solution was diluted by adding 99 mL of distilled water to obtain

100 mL of 2.5×10^{-4} M HAuCl$_4$ solution;

- 52.6 mg of TSC were dissolved in 5.26 mL of distilled water into a glass beaker (the resulting concentration of TSC is 1%). The volume ratio between HAuCl$_4$ and TSC solutions is around 19;

- Both solutions were separately heated up on a heating plate and mixed when the boiling point was reached;

- The resulting solution was kept boiling for 40 minutes to promote the reaction and it was continuously agitated through a magnetic stir bar. The solution was initially uncoloured and transparent but it rapidly became purplish and finally it turned deep red (figure 7.12). This is a strong indication of the formation of gold nanoparticles;

- At the end of the reaction, the solution was cooled down to room temperature while keeping the stirring.

As in the case of the Ag-NP synthesis, the glassware had been cleaned with distilled water and propanol before starting the synthesis process to reduce the risk of contamination and heterogeneous nucleation.
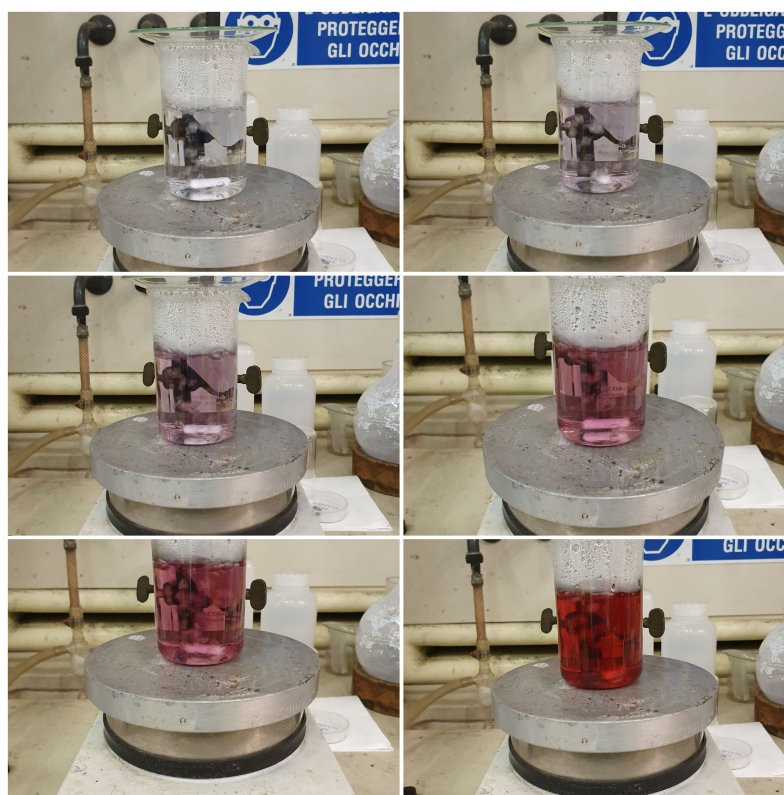
Figure 7.12: Evolution of the colouration during the preparation of colloidal gold according to the Turkevich method.

The colloid was then concentrated by multiple centrifugation cycles at 8000 RPM: 2 mL plastic tubes were filled with 1.5 mL of gold colloid and centrifuged for 5 minutes, then the clear supernatant ($\approx$ 1.3 mL) was removed. The fraction on the bottom was collected, gathered, and centrifuged again for 5 minutes, leading to some millilitres of dark red concentrated colloid.

Both the as-prepared gold colloid and the concentrate were characterized by means of UV-VIS spectroscopy, following the same experimental procedure as silver (see section 3.2). As depicted in figure 7.13, the spectrum of the as-prepared colloid features a very narrow peak at 522 nm: the narrow shape and the steep decrease of absorbance for $\lambda >$ 522 nm reveal the presence of small nanoparticles with a restricted size distribution and the absence of nanorods. The spectrum of the concentrated colloid is very similar, with a slightly broader tail towards high wavelengths.
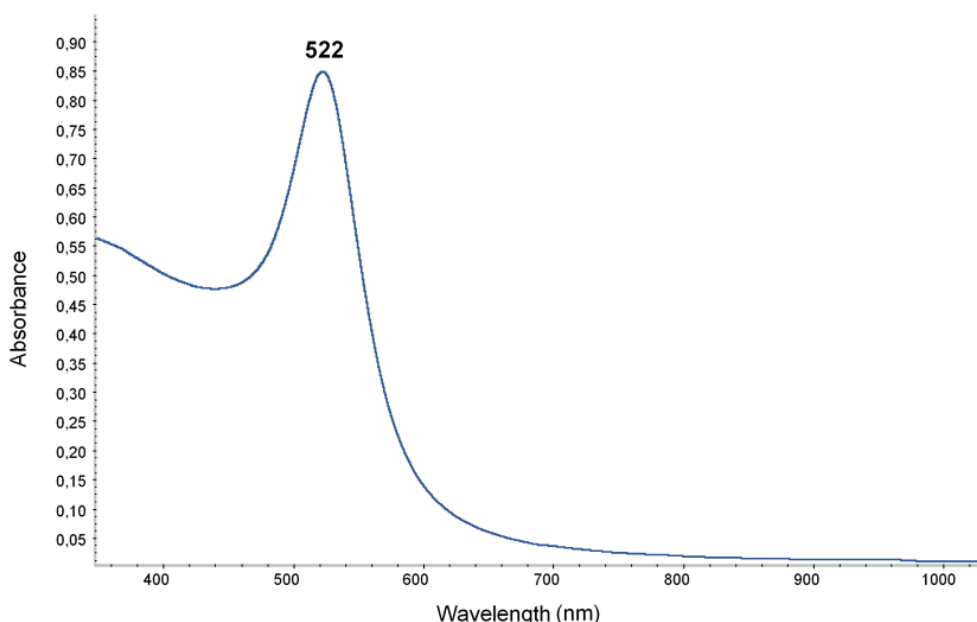
Figure 7.13: UV-VIS absorption spectrum of the as-prepared colloidal gold.

7.4.2   Preparation of Au-based SERS substrates

Gold nanoparticles were deposited on filter paper supports slightly modifying a procedure reported in [15], which employs natural sedimentation during the incubation period. Briefly, suitably prepared pieces of filter paper (4×5 mm^2) were positioned on the bottom of 3 mL glass vials, then 1 mL of concentrated gold colloid was poured in the vials and they were stocked at room temperature for 3 days. After careful extraction and drying, the substrates were stored in air until used. The dried gold substrates are characterized by a golden-brown hue (see figure 7.14).

Figure 7.14: SERS substrate obtained by natural sedimentation of concentrated Au colloid after incubation and drying.

7.4.3 SERS detection of Perampanel

Gold-based substrates were tested with the usual solutions of RH6G 10^{-6} M and acidified PER 10^{-4} and 10^{-5} M, using the 632.8 nm excitation laser focused with a 20× objective. All the SERS spectra were collected in dynamic mode, with an incident power of 5 mW and 10 s of acquisition time (5 averages). The main results are summarized in figure 7.15, in which the SERS spectra of Perampanel are shown along with the spectrum of a bare substrate.
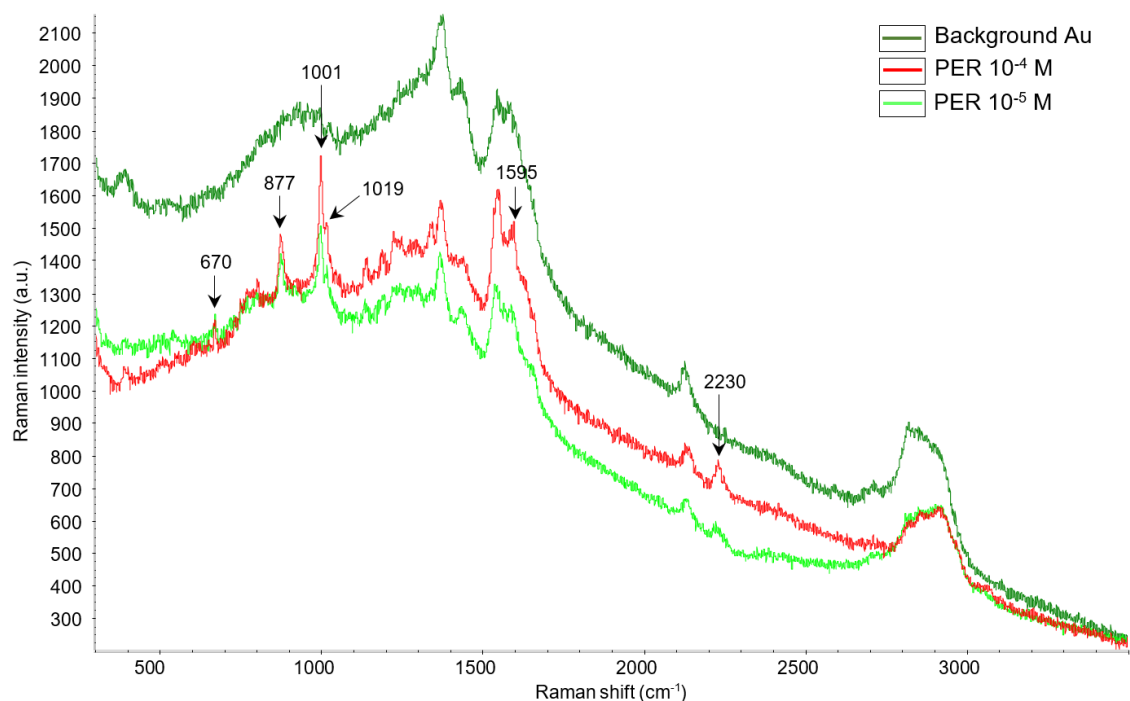
Figure 7.15: SERS spectra of acidified PER 10^{-4} M and PER 10^{-5} M; the spectrum of the background is also reported. 632.8 nm excitation, 20× objective, 5 mW power, 10 s exposure time (5 averages).

The most important markers of Perampanel at 670, 877, 1001, 1019, 1595 and 2230 cm^{-1} are visible at both concentrations, but the relative peak intensities and the signal-to-noise ratio are worse compared to the equivalent spectra recorded on silver. These findings are consistent with the results reported in a previous thesis work [8], indicating that chemically-produced gold colloids are less effective than silver in the SERS detection of Perampanel. The inferior sensing properties of gold can be ascribed to the morphology, to different chemical-physical interactions with the analyte or simply to the use of an excitation wavelength far from the resonance condition. Furthermore, although the reducing and stabilizing agent is the same as silver nanoparticles (i.e. trisodium citrate), the background signal is less intense and structured compared to silver nanoparticles. This can be explained considering that gold SERS substrates were not produced by centrifugation and that the binding structure of citrate ions on gold nanoparticles differs from that on silver [69, 85].

Conclusions and Perspectives

This thesis was born in a difficult and uncertain period, with the rapidly deteriorating public health situation and the tragic evolution of the Covid19 pandemic both at the national and international level. The consequences of the first national lockdown and the concern of a second lockdown influenced my work schedule and the choice of the most effective research activities that could be best fitted within the evolving and uncertain boundary conditions.

Nevertheless, my early investigations carried out with SERS substrates produced in still optimizable conditions were quite satisfactory and promising, therefore better results could reasonably be expected if the fabrication and detection procedures are improved based on my observations.

First of all, many substrates were produced in a relatively short time with simple chemicals (the Lee-Meisel colloid), ordinary instrumentation (a centrifuge), and inexpensive techniques. The deposition via centrifugation managed to further accelerate the production process, eliminating the long incubation period, with final results concerning sensitivity and inter-sample repeatability comparable to those achieved on substrates produced by natural sedimentation. The low spatial uniformity and intra-sample repeatability were effectively overcome by using the spinning-cell setup, which allowed not only the spatial averaging of the signal originating from a non-uniform substrate, but also the increase of the incident laser power, with a net improvement on the signal-to-noise ratio. On the other hand, the strong background contribution, probably caused by citrate anions or cellulosic materials, was partially mitigated by a chloride treatment, even if additional chemical-physical optimization would be necessary.

The anti-epileptic drug Perampanel was clearly detectable in the concentration range of 10^{-4} - 5×10^{-6} M and high quality spectra were obtained (see, for example, figure 4.15, depicting the best PER spectrum recorded during my thesis work). This indicates that large enhancement factors are possible with my setup. Moreover, in spite of quite broad error bars arising from limited substrate reproducibility, I succeeded in constructing calibration curves of the average baseline-corrected peak heights, linearly

correlated to the PER concentration in solution. It is important to underline that the concentration range of my experiments was far from the therapeutic range reported in the literature [20, 50] and, unlike rigid substrates produced by PLD [8, 9], the low concentration detection limit is 10^{-6} M instead of 3×10^{-9} M.

As for Cannabidiol, the paper-based substrates produced via centrifugation were ineffective in detecting the analyte at the concentration of 10^{-4} M, even upon the addition of magnesium chloride as enhancing agent. As a result, my paper-based substrates were not performing as the ones described in [15, 18, 19], and further analysis is required to achieve SERS detection of PER and CBD at lower concentrations and with a high-quality signal.

Finally, alternative production methods based on *in situ* reduction of silver were investigated. The synthesis of silver nanoparticles directly onto the paper support (in the presence or in the absence of an external reducing agent) resulted in an increased SERS substrates production yield, in a reduced risk of contamination and manipulation, in an improved reproducibility, and in the possibility of tuning the position of the plasmon resonance close to available laser lines in the blue-violet region (e.g., 405 nm). Further research is required, but the first results are encouraging.

All the substrates were characterized by means of UV-VIS-NIR spectroscopy and Scanning Electron Microscopy (SEM), highlighting the optical and morphological properties induced by the different production methods. Long and thin nanorods, along with large expanses of closely packed nanoparticles, were responsible for the sensing properties of substrates produced via both natural sedimentation and centrifugation. Such nanostructures were not uniformly distributed but tended to accumulate in cavities and voids among the paper fibres. On the other hand, round, small and well separated particles decorated the surface of fibres when *in situ* reduction was promoted by TSC and, as confirmed by the intense colouration, the silver content was high. Conversely, direct reduction by cellulose functional groups led to irregular and sharp particles, unevenly distributed on fibres, resulting in a fainter substrate colour, lower silver content and poor SERS properties.

Based on the outcomes of my thesis, I would like to outline possible future developments of my work and to list important points worth investigating to achieve fully optimized paper-based SERS sensors in a short time and with easy implementation.

- **Production process**: the centrifuge allows a significantly shorter production cycle but the effect of the angular velocity on the substrate performances has not been entirely clarified. Extensive SERS tests using substrates produced at various

combinations of centrifugation time and speed (above or below 5000 RPM) should be carried out. Moreover, substrates should be prepared using the colloid from one single synthesis.

- **Manipulation and handling**: the substrate extraction from the vials is one of the most critical steps during the production process and great attention must be paid in order to avoid scratching or damaging the substrates. In addition, substrate handling and positioning on the spinning-cell should be minimized by e.g. attaching the sample on a large rigid support, which could be easily touched and moved.

- **Contamination**: substrates are highly sensitive to contamination by gaseous compounds that could be naturally present in a chemistry lab at very low concentration. Therefore, the SERS substrates should be stored in a sealed environment and isolated from possible contamination sources during the drying stage and the storage.

- **Background**: the strong background contribution is not caused by contaminants either in the colloid or in the paper, but originates from the SERS signal of citrate anions and cellulose-based materials. The optimal chemical-physical condition aimed at reducing the background interference as much as possible is yet to be found. Additional treatments should be tested, including the effect of pH, chloride concentration, reducing agent, type of paper, and time and speed of centrifugation.

- **Sensitivity**: a decrease of the background intensity is expected to be accompanied by a better signal-to-noise ratio and by improved sensitivity, resulting in a lower limit of detection and a more reliable peak assignment.

- **Reproducibility**: similarly to sensitivity, also reproducibility should improve if the production process is optimized and if the background contribution is reduced. A better reproducibility, along with an increased number of data points, should result in more precise calibration curves (such as those reported in the literature [15]), with less widely scattered intensity values and narrower error bars.

- **Metal**: even if most of the measurements have been performed using silver, gold may be a valuable alternative and a complete investigation into the sensing properties of gold nanoparticles towards PER and CBD should be performed.

- **Excitation wavelength**: 632.8 nm laser has successfully excited the plasmonic response of gold and silver nanoparticles, but UV-VIS-NIR reflectance measure-

ments have highlighted the fact that the plasmon resonance of dried substrates is shifted towards the low-wavelength region of the visible spectrum. Therefore, larger enhancements could be reached using a 532 nm or a 405 nm laser, provided that the fluorescence contribution is low.

- **New substrates**: *in situ* reduction can be improved optimizing the ratio between the exposed paper surface and the silver precursor concentration, the reaction conditions (e.g., presence of alkaline activators), and the reducing agent. In particular, the exploitation of silver ions should be maximized.

- **CBD**: finally, CBD has shown a weak SERS response, therefore better results may be obtained using optimized substrates with a low background contribution. The complexing and mediating effect of magnesium ions should be investigated as well by means of more detailed computational studies.

All in all, my thesis has proved the feasibility of simple, cheap and rapid methods to produce effective paper-based SERS sensors for the detection of selected types of AEDs. In spite of several critical issues and improvable aspects, positive results have been achieved, representing an interesting starting point for future optimization.

Bibliography

[1]   E. C. Le Ru and P. G. Etchegoin. *Principles of Surface-Enhanced Raman Spectroscopy*. Amsterdam: Elsevier, 2009.

[2]   K. Kneipp, H. Kneipp, I. Itzkan et al. "Surface-enhanced Raman scattering and biophysics". In: *Journal of Physics: Condensed Matter*, vol. 14, no. 18 (2002), pp. 597–624. DOI: 10.1088/0953-8984/14/18/202.

[3]   R. Pilot, R. Signorini, C. Durante et al. "A Review on Surface-Enhanced Raman Scattering". In: *Biosensors*, vol. 9, no. 2: 57 (2019). DOI: 10.3390/bios9020057.

[4]   A. Jaworska, S. Fornasaro, V. Sergo et al. "Potential of Surface Enhanced Raman Spectroscopy (SERS) in Therapeutic Drug Monitoring (TDM). A critical review". In: *Biosensors*, vol. 6, no. 3: 47 (2016). DOI: 10.3390/bios6030047.

[5]   M. Tommasini, C. Zanchi, A. Lucotti et al. "Laser Synthesized Nanoparticles for Therapeutic Drug Monitoring". In: *Advances in the Application of Lasers in Materials Science*. Ed. by P. M. Ossi. Cham, Switzerland: Springer International Publishing, 2018, pp. 339–360.

[6]   M. Tommasini, C. Zanchi, A. Lucotti et al. "Laser-Synthesized SERS Substrates as Sensors toward Therapeutic Drug Monitoring". In: *Nanomaterials*, vol. 9, no. 5: 677 (2019). DOI: 10.3390/nano9050677.

[7]   F. Iacoe. "Production of optimized Ag colloids for sensing by SERS the anti-epileptic drug Lamotrigine". Master's thesis. Politecnico di Milano, 2018. URL: https://www.politesi.polimi.it/handle/10589/147867.

[8]   N. S. Villa. "Development of a SERS technique for Therapeutic Drug Monitoring: case study on Perampanel". Master's thesis. Politecnico di Milano, 2018. URL: https://www.politesi.polimi.it/handle/10589/142314.

[9]   L. Giuliani. "SERS of Perampanel for Therapeutic Drug Monitoring using substrates produced by PLD". Master's thesis. Politecnico di Milano, 2018. URL: https://www.politesi.polimi.it/handle/10589/145302.

[10] C. Zanchi, L. Giuliani, A. Lucotti et al. "On the performance of laser-synthesized, SERS-based sensors for drug detection". In: *Applied Surface Science*, vol. 507, 145109 (2020). DOI: 10.1016/j.apsusc.2019.145109.

[11] M. Santoro, E. Fazio, S. Trusso et al. "SERS sensing of Perampanel with nano-structured arrays of gold particles produced by pulsed laser ablation in water". In: *Medical Devices & Sensors*, vol. 1, no. 1: e10003 (2018). DOI: 10.1002/mds3.10003.

[12] C. Zanchi, A. Lucotti, M. Tommasini et al. "Pulsed laser deposition of gold thin films with long-range spatial uniform SERS activity". In: *Applied Physics A*, vol. 125, no. 5: 311 (2019). DOI: 10.1007/s00339-019-2527-7.

[13] M. J. Oliveira, P. Quaresma, A. Araújo et al. "Office paper decorated with silver nanostars - an alternative cost effective platform for trace analyte detection by SERS". In: *Scientific Reports*, vol. 7, no. 1: 2480 (2017). DOI: 10.1038/s41598-017-02484-8.

[14] S. A. Ogundare and W. E. van Zyl. "A review of cellulose-based substrates for SERS: fundamentals, design principles, applications". In: *Cellulose*, vol. 26, no. 11 (2019), pp. 6489–6528. DOI: 10.1007/s10570-019-02580-0.

[15] S. Dalla Marta, C. Novara, A. Bonifacio et al. "Optimization and Characterization of Paper-Made Surface Enhanced Raman Scattering (SERS) Substrates with Au and Ag NPs for Quantitative Analysis". In: *Materials*, vol. 10, no. 12: 1365 (2017). DOI: 10.3390/ma10121365.

[16] K. Xu, R. Zhou, K. Takei et al. "Toward Flexible Surface-Enhanced Raman Scattering (SERS) Sensors for Point-of-Care Diagnostics". In: *Advanced Science*, vol. 6, no. 16: 1900925 (2019). DOI: 10.1002/advs.201900925.

[17] Y. Lu, Y. Luo, Z. Lin et al. "A silver-nanoparticle/cellulose-nanofiber composite as a highly effective substrate for surface-enhanced Raman spectroscopy". In: *Beilstein Journal of Nanotechnology*, vol. 10 (2019), pp. 1270–1279. DOI: 10.3762/BJNANO.10.126.

[18] S. Fornasaro, S. Dalla Marta, M. Rabusin et al. "Toward SERS-based point-of-care approaches for therapeutic drug monitoring: The case of Methotrexate". In: *Faraday Discussions*, vol. 187 (2016), pp. 485–499. DOI: 10.1039/c5fd00173k.

[19] M. Yokoyama, K. Yamada, T. Nishimura et al. "Paper-based surface enhanced Raman spectroscopy of Phenobarbital sodium for point-of-care therapeutic drug monitoring". In: *Proceedings of SPIE - Optical Diagnostics and Sensing XV: Toward Point-of-Care Diagnostics*. Vol. 9332. 2015. DOI: 10.1117/12.2080619.

[20] D.-Y. Kim, J. Moon, Y.-W. Shin et al. "Usefulness of saliva for Perampanel therapeutic drug monitoring". In: *Epilepsia*, vol. 61, no. 6 (2020), pp. 1120–1128. DOI: 10.1111/epi.16513.

[21] J. P. Szaflarski, K. Hernando, E. M. Bebin et al. "Higher Cannabidiol plasma levels are associated with better seizure response following treatment with a pharmaceutical grade Cannabidiol". In: *Epilepsy and Behavior*, vol. 95 (2019), pp. 131–136. DOI: 10.1016/j.yebeh.2019.03.042.

[22] Nobel Media AB 2020. *The Nobel Prize in Physics 1930*. [Online]. URL: https://www.nobelprize.org/prizes/physics/1930/summary/ (visited on 12/07/2020).

[23] D. A. Long. *The Raman effect: a unified treatment of the theory of Raman scattering by molecules*. Chichester, England: John Wiley & Sons, Ltd, 2002.

[24] N. B. Colthup, L. D. Haly and S. E. Wiberley. *Introduction to Infrared and Raman Spectroscopy*. 3rd edition. San Diego, CA: Academic Press, Inc., 1990.

[25] E. Smith and G. Dent. *Modern Raman Spectroscopy: A Practical Approach*. 2nd edition. Hoboken, NJ: John Wiley & Sons, Ltd, 2019. Chap. 4 (pp. 101-117).

[26] S. V. Gaponenko. *Introduction to nanophotonics*. Cambridge: Cambridge University Press, 2010.

[27] S. A. Maier. *Plasmonics: fundamentals and applications*. New York, NY: Springer US, 2007.

[28] M. A. Mahmoud and M. A. El-Sayed. "Different plasmon sensing behavior of silver and gold nanorods". In: *Journal of Physical Chemistry Letters*, vol. 4, no. 9 (2013), pp. 1541–1545. DOI: 10.1021/jz4005015.

[29] D. A. Skoog, F. J. Holler and S. R. Crouch. *Principles of Instrumental Analysis*. 7th edition. Boston, MA: Cengage Learning, 2018. Chap. 13 (pp. 304-326).

[30] Z. Chen, T. G. Deutsch et al. "UV-Vis spectroscopy". In: *Photoelectrochemical Water Splitting: Standards, Experimental Methods, and Protocols*. Ed. by Z. Chen, H. N. Dinh and E. Miller. New York, NY: Springer, 2013, pp. 49–62.

[31] J. P. Blitz. "Diffuse Reflectance Spectroscopy". In: *Modern Techniques in Applied Molecular Spectroscopy*. Ed. by F. M. Mirabella. Hoboken, NJ: John Wiley & Sons, Inc, 1998, pp. 185–219.

[32] The Editors of Encyclopaedia Britannica. *Epilepsy. Encyclopædia Britannica, inc.* [Online]. URL: https://www.britannica.com/science/epilepsy (visited on 27/07/2020).

[33] S. Lattanzi and P. Striano. "The impact of Perampanel and targeting AMPA transmission on anti-seizure drug discovery". In: *Expert Opinion on Drug Discovery*, vol. 14, no. 3 (2019), pp. 195–197. DOI: 10.1080/17460441.2019.1566318.

[34] L. M. Willems, S. Bauer, F. Rosenow et al. "Recent advances in the pharmacotherapy of epilepsy: Brivaracetam and Perampanel as broad-spectrum anti-seizure drugs for the treatment of epilepsies and status epilepticus". In: *Expert Opinion on Pharmacotherapy*, vol. 20, no. 14 (2019), pp. 1755–1765. DOI: 10.1080/14656566.2019.1637420.

[35] A. Satlin, L. D. Kramer and A. Laurenza. "Development of Perampanel in epilepsy". In: *Acta Neurologica Scandinavica*, vol. 127, no. s197 (2013), pp. 3–8. DOI: 10.1111/ane.12098.

[36] T. Hanada. "The discovery and development of Perampanel for the treatment of epilepsy". In: *Expert Opinion on Drug Discovery*, vol. 9, no. 4 (2014), pp. 449–458. DOI: 10.1517/17460441.2014.891580.

[37] T. Hanada, Y. Hashizume, N. Tokuhara et al. "Perampanel: A novel, orally active, noncompetitive AMPA-receptor antagonist that reduces seizure activity in rodent models of epilepsy". In: *Epilepsia*, vol. 52, no. 7 (2011), pp. 1331–1340. DOI: 10.1111/j.1528-1167.2011.03109.x.

[38] European Medicines Agency. Committee for Medicinal Products for Human Use (CHMP). *EMA/424476/2012 - Fycompa: EPAR - Public assessment report (2012)*. [Online]. URL: https://www.ema.europa.eu/en/documents/assessment-report/fycompa-epar-public-assessment-report_en.pdf (visited on 27/07/2020).

[39] E. Marom and S. Rubnov. "Polymorphs of Perampanel". U.S. pat. US9096574B2. MAPI PHARMA Ltd. 4th Aug. 2015. URL: https://patents.google.com/patent/US9096574B2/en?oq=US+9%2c096%2c574+B2.

[40] A.-A. Guseynov, S. A. Pisarev, D. A. Shulga et al. "Computational characterization of the glutamate receptor antagonist Perampanel and its close analogs: density functional exploration of conformational space and molecular docking study". In: *Journal of Molecular Modeling*, vol. 25, no. 10: 312 (2019). DOI: 10.1007/s00894-019-4188-z.

[41] H. Li, Y. Liu, D. Tian et al. "Overview of Cannabidiol (CBD) and its analogues: Structures, biological activities, and neuroprotective mechanisms in epilepsy and Alzheimer's disease". In: *European Journal of Medicinal Chemistry*, vol. 192, 112163 (2020). DOI: 10.1016/j.ejmech.2020.112163.

[42] A. Arzimanoglou, U. Brandl, J. H. Cross et al. "Epilepsy and Cannabidiol: a guide to treatment". In: *Epileptic Disorders*, vol. 22, no. 1 (2020), pp. 1–14. DOI: `10.1684/epd.2020.1141`.

[43] S. Silvestro, S. Mammana, E. Cavalli et al. "Use of Cannabidiol in the treatment of epilepsy: Efficacy and security in clinical trials". In: *Molecules*, vol. 24, no. 8: 1459 (2019). DOI: `10.3390/molecules24081459`.

[44] D. Samanta. "Cannabidiol: A Review of Clinical Efficacy and Safety in Epilepsy". In: *Pediatric Neurology*, vol. 96 (2019), pp. 24–29. DOI: `10.1016/j.pediatrneurol.2019.03.014`.

[45] European Medicines Agency. Committee for Medicinal Products for Human Use (CHMP). *EMA/458106/2019 - Epidyolex: EPAR - Public assessment report (2019)*. [Online]. URL: `https://www.ema.europa.eu/en/documents/assessment-report/epidyolex-epar-public-assessment-report_en.pdf` (visited on 17/08/2020).

[46] T. Mayr, T. Grassl, N. Korber et al. "Cannabidiol revisited". In: *IUCrData*, vol. 2, no. 2: x170276 (2017). DOI: `10.1107/s2414314617002760`.

[47] S. K. Islam, Y. P. Cheng, R. L. Birke et al. "An analysis of tetrahydrocannabinol (THC) and its analogs using surface enhanced Raman Scattering (SERS)". In: *Chemical Physics*, vol. 536, 110812 (2020). DOI: `10.1016/j.chemphys.2020.110812`.

[48] J.-S. Kang and M.-H. Lee. "Overview of therapeutic drug monitoring". In: *Korean Journal of Internal Medicine*, vol. 24, no. 1 (2009), pp. 1–10. DOI: `10.3904/kjim.2009.24.1.1`.

[49] I. Aícua-Rapún, P. André, A. O. Rossetti et al. "Therapeutic Drug Monitoring of Newer Antiepileptic Drugs: A Randomized Trial for Dosage Adjustment". In: *Annals of Neurology*, vol. 87, no. 1 (2020), pp. 22–29. DOI: `10.1002/ana.25641`.

[50] P. N. Patsalos, E. P. Spencer and D. J. Berry. "Therapeutic Drug Monitoring of Antiepileptic Drugs in Epilepsy: A 2018 Update". In: *Therapeutic Drug Monitoring*, vol. 40, no. 5 (2018), pp. 526–548. DOI: `10.1097/FTD.0000000000000546`.

[51] S. Jacob and A. B. Nair. "An Updated Overview on Therapeutic Drug Monitoring of Recent Antiepileptic Drugs". In: *Drugs in R&D*, vol. 16, no. 4 (2016), pp. 303–316. DOI: `10.1007/s40268-016-0148-6`.

[52] P. Slepička, N. S. Kasálková, J. Siegel et al. "Methods of gold and silver nanoparticles preparation". In: *Materials*, vol. 13, no. 1: 1 (2020). DOI: `10.3390/ma13010001`.

[53] P. C. Lee and D. Meisel. "Adsorption and Surface-Enhanced Raman of Dyes on Silver and Gold Sols". In: *The Journal of Physical Chemistry*, vol. 86, no. 17 (1982), pp. 3391–3395. DOI: `10.1021/j100214a025`.

[54] V. S. Tiwari, T. Oleg, G. K. Darbha et al. "Non-resonance SERS effects of silver colloids with different shapes". In: *Chemical Physics Letters*, vol. 446, no. 1-3 (2007), pp. 77–82. DOI: `10.1016/j.cplett.2007.07.106`.

[55] K. Ohlendieck. "Centrifugation". In: *Principles and Techniques of Biochemistry and Molecular Biology*. Ed. by K. Wilson and J. Walker. 7th edition. Cambridge: Cambridge University Press, 2010, pp. 73–99.

[56] I. Yaremchuk, V. Fitio and Y. Bobitski. "Silver nanoparticles under plasmon resonance conditions". In: *28th International Conference on Microelectronics (MIEL) Proceedings*. IEEE. 2012, pp. 297–300. DOI: `10.1109/MIEL.2012.6222859`.

[57] M. T. Postek and A. E. Vladár. "Does your SEM really tell the truth? How would you know? Part 4: charging and its mitigation". In: *Proceedings of SPIE - International Society for Optics and Photonics: Scanning Microscopies 2015*. Vol. 9636. 2015. DOI: `10.1117/12.2195344`.

[58] W. Rasband et al. *ImageJ 1.53e*. National Institutes of Health, USA [Online]. URL: `https://imagej.nih.gov/ij/index.html` (visited on 29/10/2020).

[59] D. Paramelle, A. Sadovoy, S. Gorelik et al. "A rapid method to estimate the concentration of citrate capped silver nanoparticles from UV-visible light spectra". In: *Analyst*, vol. 139, no. 19 (2014), pp. 4855–4861. DOI: `10.1039/c4an00978a`.

[60] E. Lee. "Imaging modes". In: *Raman Imaging. Techniques and Applications*. Ed. by A. Zoubir. Berlin Heidelberg: Springer, 2012, pp. 1–37.

[61] P. Li, X. Zhou, H. Liu et al. "Surface-enhanced Raman evidence for Rhodamine 6G and its derivative with different adsorption geometry to colloidal silver nanoparticle". In: *Journal of Raman Spectroscopy*, vol. 44, no. 7 (2013), pp. 999–1003. DOI: `10.1002/jrs.4319`.

[62] Wikimedia Commons contributors. Wikimedia Commons, the free media repository [Online]. URL: `https://commons.wikimedia.org/wiki/File:Rhodamine_6G.svg` (visited on 10/11/2020).

[63] F. Zhong, Z. Wu, J. Guo et al. "Porous silicon photonic crystals coated with Ag nanoparticles as efficient substrates for detecting trace explosives using SERS". In: *Nanomaterials*, vol. 8, no. 11: 872 (2018). DOI: `10.3390/nano8110872`.

[64] G. Socrates. *Infrared and Raman Characteristic Group Frequencies*. 3rd edition. Chichester, England: John Wiley & Sons, Ltd, 2004.

[65] U. P. Agarwal. "Analysis of cellulose and lignocellulose materials by Raman spectroscopy: a review of the current status". In: *Molecules*, vol. 24, no. 9: 1659 (2019). DOI: 10.3390/molecules24091659.

[66] Y. Zhang, F. Wang, H. Yin et al. "Nonuniform Distribution of Capping Ligands Promoting Aggregation of Silver Nanoparticles for Use as a Substrate for SERS". In: *Advances in Nanoparticles*, vol. 2 (2013), pp. 104–111. DOI: 10.4236/anp.2013.22018.

[67] W.-L.-J. Hasi, X. Lin, X.-T. Lou et al. "Chloride ion-assisted self-assembly of silver nanoparticles on filter paper as SERS substrate". In: *Applied Physics A: Materials Science and Processing*, vol. 118, no. 3 (2015), pp. 799–807. DOI: 10.1007/s00339-014-8800-x.

[68] M. Grouchko, A. Kamyshny, C. F. Mihailescu et al. "Conductive Inks with a Built-In Mechanism That Enables Sintering at Room Temperature". In: *ACS Nano*, vol. 5, no. 4 (2011), pp. 3354–3359. DOI: 10.1021/nn2005848.

[69] P. Wulandari, T. Nagahiro, N. Fukada et al. "Characterization of citrates on gold and silver nanoparticles". In: *Journal of Colloid and Interface Science*, vol. 438 (2015), pp. 244–248. DOI: 10.1016/j.jcis.2014.09.078.

[70] N. Leopold, A. Stefancu, K. Herman et al. "The role of adatoms in chloride-activated colloidal silver nanoparticles for surface-enhanced Raman scattering enhancement". In: *Beilstein Journal of Nanotechnology*, vol. 9 (2018), pp. 2236–2247. DOI: 10.3762/bjnano.9.208.

[71] T. Mostowtt and B. McCord. "Surface enhanced Raman spectroscopy (SERS) as a method for the toxicological analysis of synthetic cannabinoids". In: *Talanta*, vol. 164 (2017), pp. 396–402. DOI: 10.1016/j.talanta.2016.11.002.

[72] S. K. Islam, Y. P. Cheng, R. L. Birke et al. "Rapid and sensitive detection of synthetic cannabinoids AMB-FUBINACA and α-PVP using surface enhanced Raman scattering (SERS)". In: *Chemical Physics*, vol. 506 (2018), pp. 31–35. DOI: 10.1016/j.chemphys.2018.03.028.

[73] E. L. Doctor and B. McCord. "Comparison of aggregating agents for the surface-enhanced Raman analysis of benzodiazepines". In: *Analyst*, vol. 138, no. 20 (2013), pp. 5926–5932. DOI: 10.1039/c3an00669g.

[74] D. R. Case, J. Zubieta and R. P. Doyle. "The Coordination Chemistry of Bio-Relevant Ligands and Their Magnesium Complexes". In: *Molecules*, vol. 25, no. 14: 3172 (2020). DOI: 10.3390/molecules25143172.

[75] T. Dudev, J. A. Cowan and C. Lim. "Competitive binding in magnesium co-ordination chemistry: Water versus ligands of biological interest". In: *Journal of the American Chemical Society*, vol. 121, no. 33 (1999), pp. 7665–7673. DOI: `10.1021/ja984470t`.

[76] J. Weston. "Biochemistry of Magnesium". In: *PATAI's Chemistry of Functional Groups, Online*. Ed. by Z. Rappoport. John Wiley & Sons, Ltd, 2009. DOI: `10.1002/9780470682531.pat0407`.

[77] Avogadro. *Avogadro: an open-source molecular builder and visualization tool*. Version 1.2.0 [Online]. URL: `http://avogadro.cc/` (visited on 11/11/2020).

[78] A. A. Nayeb-Hashemi and J. B. Clark. "The Ag-Mg (Silver-Magnesium) System". In: *Bulletin of Alloy Phase Diagrams*, vol. 5, no. 4 (1984), pp. 348–358.

[79] Y. Park, Y. N. Hong, A. Weyers et al. "Polysaccharides and phytochemicals: a natural reservoir for the green synthesis of gold and silver nanoparticles". In: *IET nanobiotechnology*, vol. 5, no. 3 (2011), pp. 69–78. DOI: `10.1049/iet-nbt.2010.0033`.

[80] S. A. Ogundare and W. E. van Zyl. "Nanocrystalline cellulose as reducing and stabilizing agent in the synthesis of silver nanoparticles: Application as a sur-face enhanced Raman scattering (SERS) substrate". In: *Surfaces and Interfaces*, vol. 13 (2018), pp. 1–10. DOI: `10.1016/j.surfin.2018.06.004`.

[81] Y.-J. Xu, L.-G. Zuo, X. Qian et al. "Preparation and Characterization of Cellulose-Silver Nanocomposites by in situ Reduction with Alkalis as Activation Reagent". In: *BioResources*, vol. 11, no. 1 (2016), pp. 2797–2808. DOI: `10.15376/biores.11.1.2797-2808`.

[82] C. M. Cobley, S. E. Skrabalak, D. J. Campbell et al. "Shape-controlled synthesis of silver nanoparticles for plasmonic and sensing applications". In: *Plasmonics*, vol. 4, no. 2 (2009), pp. 171–179. DOI: `10.1007/s11468-009-9088-0`.

[83] A. L. González, C. Noguez, J. Beránek et al. "Size, shape, stability, and color of plasmonic silver nanoparticles". In: *Journal of Physical Chemistry C*, vol. 118, no. 17 (2014), pp. 9128–9136. DOI: `10.1021/jp5018168`.

[84] J. Turkevich, P. C. Stevenson and J. Hillier. "A study of the nucleation and growth processes in the synthesis of colloidal gold". In: *Discussions of the Faraday Society*, vol. 11 (1951), pp. 55–75. DOI: `10.1039/DF9511100055`.

[85] J.-W. Park and J. S. Shumaker-Parry. "Structural Study of Citrate Layers on Gold Nanoparticles". In: *Journal of the American Chemical Society*, vol. 136, no. 5 (2014), pp. 1907–1921. DOI: `10.1021/ja4097384`.